ELECTROCHEMICAL TRANSPORT IN
ENERGY STORAGE SYSTEMS

A DISSERTATION
SUBMITTED TO THE DEPARTMENT OF ENERGY SCIENCE
AND ENGINEERING
AND THE COMMITTEE ON GRADUATE STUDIES
OF STANFORD UNIVERSITY
IN PARTIAL FULFILLMENT OF THE REQUIREMENTS
FOR THE DEGREE OF
DOCTOR OF PHILOSOPHY

Weiyu Li

May 2023

Abstract

Rechargeable lithium batteries are electrochemical devices widely used in portable electronics and electric-powered vehicles. A breakthrough in battery performance requires advancements in battery cell configurations at the microscale level. This, in turn, places a premium on the ability to accurately predict complex multiphase thermo-electrochemical phenomena, e.g., migration of ions interacting with composite porous materials that constitute a battery cell microstructure.

Optimal design of **porous cathodes** requires efficient quantitative models of microscopic (pore-scale) electrochemical processes and their impact on battery performance. We derive effective properties (electrical conductivity, ionic diffusivity, reaction parameters) of a composite electrode comprising the active material coated with a mixture of the binder and conductor (the carbon binder domain or CBD). These effective descriptors ensure the conservation of mass and charge. When used to parameterize industry-standard pseudo-two-dimensional (P2D) models, they significantly improve the predictions of lithiation curves in the presence of CBD. We identified a P2D model that provides a middle ground between model complexity and prediction accuracy.

On the **lithium anode**, dendritic growth is a leading cause of degradation and catastrophic failure of batteries with lithium anodes, e.g., lithium-metal batteries and all-solid-state lithium batteries. Deep understanding of this phenomenon would facilitate the design of strategies to reduce, or completely suppress, the instabilities characterizing electrodeposition on the lithium anode. We present linear stability analyses to quantify the interfacial instability associated with dendrite formation in

terms of the battery's operating conditions and the electrochemical and physical properties of battery materials. This would improve the safety of lithium-metal batteries with liquid electrolyte and all-solid-state lithium batteries.

When considered holistically, the quantitative nature of our work provides mechanistic insights into the optimal design of i) porous cathodes, ii) electrolytes, and iii) dendrite-suppressing buffers between the lithium-metal anode and electrolyte. The design of electrolytes involves the optimal selection of a solvent and salt, the tuning of the ionic concentration of the solution, and the deployment of anisotropic electrolytes (e.g., liquid crystals, liquid-crystalline physical gels, and the use of separators with anisotropic pore structures or columnized membranes).

Acknowledgement

First and foremost, I am deeply indebted to my Ph.D. advisors, Prof. Daniel Tartakovsky and Prof. Hamdi Tchelepi. Four years ago, you welcomed me into your research group, which has had a profound and transformative impact on my life. Being your student has been the greatest privilege and the best thing that has ever happened to me. Throughout my journey at Stanford, you have been there for me during the happiest moments, celebrating my achievements with genuine joy. Similarly, during moments of despair, you have uplifted me and provided the motivation to persevere. Your constant presence and unwavering support have meant the world to me. Through both good times and bad times, you have proven to be the best advisors I could have ever imagined or asked for. The exposure to diverse problems under your guidance has broadened my perspective and enriched my skill sets. I am thankful for the countless opportunities you have provided me, allowing me to explore and grow. Thank you for valuing my intellectual curiosity and for nurturing it throughout my Ph.D. journey. Your belief in my abilities has given me the confidence to embrace every moment and cherish every opportunity. Thank you for your emphasis on keeping the people in my life as the top priority while motivating my academic progress. Thank you for guiding me to value the connections and relationships that matter. Thank you for placing your unconditional trust in me and for the immeasurable impact you have had on my growth and development as a researcher.

I extend my sincere appreciation to Prof. Yi Cui for your invaluable help and support during my faculty job search and for your role as a member of my Ph.D. committee. It was your class that has ignited my interest in battery-related research. Your expertise in this field has been truly instrumental in shaping my academic

journey. I want to express my gratitude for the time you have generously devoted to me and the interactions we have had. Your guidance and mentorship have been invaluable, and I am honored to have had the opportunity to interact with your research group. I am truly grateful for all the doors you have opened for me and for the chance to contribute to your lab's groundbreaking work in the future.

I am also immensely grateful to Prof. Steven Chu for being a true inspiration and role model to me. Growing up, I read your stories with admiration, and your achievements have had a profound impact on my academic journey. Your words at 2009 Harvard Commencement—"If you don't have a hobby, look for it, and don't stop until you find it. Life is too short to walk empty-handed. You must pour your affection into something."—have deeply resonated with me. I am committed to following this philosophy in my own life, constantly seeking and nurturing my passions. Thank you for being part of my Ph.D. committee and thank you for your help with my dissertation. Additionally, I extend my gratitude to Prof. Lenya Ryzhik for serving as the chair of my Ph.D. defense. Your support throughout the entire process has been indispensable.

I would like to acknowledge the influence of Prof. Marcos Intaglietta at UC San Diego. Your intriguing problems in biomedical research have broadened and enriched my knowledge in a different field. Working alongside you, the founder of the field of Bioengineering, has been a truly meaningful experience. Your expertise and passion in addressing challenging bio-related problems have inspired me to continue pursuing solutions in this field. I am also grateful for the collaborative efforts of Dr. Amy Tsai from UC San Diego and Prof. Judith Martini, Vice Chair of Transplant Anesthesia from the Medical University of Innsbruck, Austria.

I extend my gratitude to Prof. Yiguang Ju from Princeton University for your continuous support and assistance during my studies at both Princeton and Stanford. During the most challenging times I encountered, you stood by my side, providing me with unwavering support that I will forever be grateful for. Thank you, Prof. Ju, for your support during my application to graduate school and faculty job search. Your guidance and expertise were crucial in navigating these important milestones. In moments of significant decisions and choices, you have always been there to offer

me unwavering support and valuable guidance.

I would also like to thank Prof. William Chueh for the insightful discussions we have had. I extend my appreciation to Dr. Yijin Liu at SLAC National Accelerator Laboratory for the fruiteful collaboration. Additionally, I would like to acknowledge all ESE faculty and staff for creating a conducive research environment and for their assistance throughout my academic journey.

I am grateful to Dr. Francesca Boso from Tartakovsky's research group and Dr. Kimoon Um from Hyundai Motor Group, South Korea, for your collaboration, patience and support. Your contributions have significantly enriched my research. I would like to express my appreciation to Dr. Jie Yang, now at Meta, for providing help and guidance during the early stages of my Ph.D.

Special thanks go to Caroline Chen and Roger Jiang, outstanding undergraduate interns whom I had the honor to supervise. Your dedication and enthusiasm convinced me to embrace the role of a teacher.

I am grateful to my funding sources, National Science Foundation, Hyundai Motor Group, TotalEnergies, and Lawrence Berkeley Lab, for their financial support, which made this research possible. I would like to thank the Siebel Scholar Foundation for appointing me as a Siebel Scholar and for graciously sponsoring the final stages of my Ph.D.

To my dear friends in ESE Department, including Livia, Xiaoyu, Alaa, Hannah, Zitong, Yuan, Manju, Su, Yunan, Yulman, Shaunak, Apoorv, Adrienne, Juliane, Henrique, Dimitrios, Dong, Jun, Joseph, Rasim, Bex and Alec, thank you for your companionship and encouragement throughout this journey.

I would like to express my deepest appreciation to my best friend, Qiaoling, for always being there for me throughout the past ten years, offering words of encouragement, and providing a source of inspiration. I am deeply thankful for the bond we share and for the countless memories we have created together. Qiaoling's friendship has been a pillar of strength, and I am truly fortunate to have you as my best friend.

To my beloved parents, I am wholeheartedly grateful for your unwavering support, unconditional love and sacrifices you have made throughout my education. Words cannot adequately express my gratitude for the love and support you have showered

upon me. I am forever proud to have you as my parents, and I am eternally grateful for everything you have done for me.　亲爱的爸爸妈妈，我衷心感谢你们在我求学过程中给予的坚定支持、无条件的爱以及所做出的牺牲。言语无法充分表达我对你们给予的爱和支持的感激之情。我永远以有你们作为我的父母而自豪，感谢你们为我付出的一切。

Contents

List of Tables

List of Figures

Chapter 1

Introduction

1.1 Background

U.S. Energy Information Administration (EIA) projects that U.S. energy-related CO2 emissions drop 25% to 38% below what they were in 2005 by 2030 [1]. This projected reductions are driven by increased electrification, higher equipment efficiency, and renewables deployment in the electric power sector. However, longer-term growth in U.S. transportation and industrial activity may limit these reductions . Biden Administration has set goals of 100% carbon pollution-free electricity by 2035 and net-zero greenhouse gas emissions by 2050. These forecasts and ambitious goals point towards research opportunities in renewable energy conversion, storage and decarbonization. Global industries are rapidly adapting to these new opportunities including the design and manufacturing of new batteries that are more efficient, more environmentally friendly, more affordable and more convenient than the present alternatives.

Batteries are electrochemical devices that act as energy storage units; their performance improvements over the last few decades have allowed the development of technological applications such as portable electronic devices and electric-powered vehicles (EV). Moreover, the increasingly preponderant use of renewable resources relies on their deployment as key elements of energy distribution systems, to transform them into smart energy grids. Both industry and end consumers require constant performance developments, pushing the research efforts towards design solutions that

would improve charge/discharge speeds by increasing energy and power density, enhance device longevity by delaying capacity fade and degradation, while guaranteeing safety and containing costs.

1.1.1   Battery basics

Each battery cell includes two electrodes (cathode and anode), a separator, two current collectors and an electrolyte (Figure 1.1). In an Li-ion battery, graphite is used as the *anode* material. The *cathode* consists of lithium intercalation materials [2], such as lithium cobalt oxide, lithium nickel manganese cobalt oxide, lithium manganese oxide, or lithium iron phosphate. The *separator* is a permeable membrane that enables the movement of Li ions in the electrolyte through the holes and prevents the direct contact between the electrodes, thus safeguards the battery against short-circuiting. The *current collectors* are electrical conductors that collect the electrons generated by the electrochemical reactions and transport them through the external circuit of the battery.
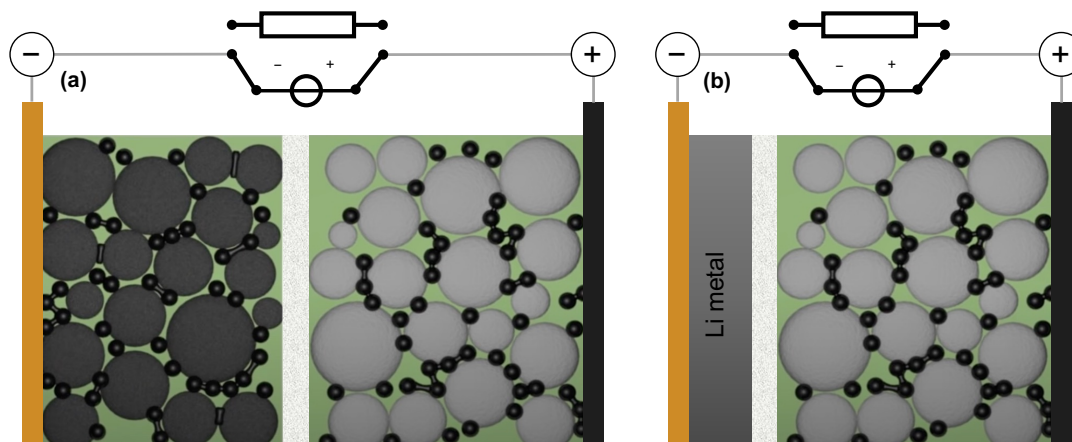
Figure 1.1: Schematic representation of (a) a Li-ion battery and (b) a Li-metal battery. In this diagram, the active materials in the cathode and anode are represented by large grey and black circles, while the carbon binder domain (CBD) is represented by small black circles. Graphite and Li-metal are used as anode materials in the case of Li-ion and Li-metal batteries.

Active cathode material particles, as well as graphite anode material particles, are

routinely mixed with conductive additive and binder, or the so-called carbon binder domain, to improve the electric conductivity and mechanical stability of electrodes. The active materials and the carbon binder domain construct the microstructure of the electrodes with the resulting pore spaces filled up with electrolyte.

During charging, an external electrical power source (the charging circuit) is applied to the Li-ion battery and an oxidation half-reaction at the cathode produces positively charged Li ions and negatively charged electrons. The Li ions move out of the active material structure in the cathode through deintercalation and transport through the liquid electrolyte in the pores of the cathode and separator and get intercalated inside the graphite particles in the anode. The electrons move through the external circuit from the cathode to the anode, and then they recombine with Li ions at the anode in a reduction half-reaction. During discharging, these reactions and transport phenomena take place in the opposite direction: the anode active material is oxidized and produces Li ions and electrons that subsequently migrate from the anode to the cathode via the electrolyte or the external circuit.

Replacing the porous graphite anode of a conventional Li-ion battery with a solid Li-metal plate significantly improves the energy density of the resulting Li-metal battery (Figure 1.1(b)). The theoretical specific capacity of a Li-metal anode (3,860 mAh/g) is about 10 times higher than that of a graphite anode (372 mAh/g). Unlike the intercalation and deintercalation of Li ions into and from the graphite host in a Li-ion battery, in an Li-metal battery, Li metal is alternatively plated and stripped from the anode during charging and discharging cycles. Li-metal batteries hold the potential of becoming the next-generation energy storage devices; however, several significant challenges associated with the Li-metal anode impede their commercialization as rechargeable batteries. These challenges, including dendrite formation, infinite volume change, and fracture of the solid electrolyte interphase layer, result in low reversibility and Columbic efficiency of Li-metal batteries, as discussed in Section 1.2 in detail.

Both the Li-ion and Li-metal batteries utilize the same composite cathode materials, i.e., (transition-metal oxide) active material particles and carbon binder domains.

Understanding the complex multi-phase thermo-electro-chemical phenomena that occur at the micro-scale level of battery cell configurations, where ions interact with the composite porous materials that constitute each battery cell microstructure, is crucial to improving battery performance. Therefore, continued research into the development of new materials, designs, and manufacturing processes at the micro-scale level is necessary for the advancement of battery technology.

1.1.2   State-of-the-art batteries

Currently, Li-ion batteries are considered to be the state-of-the-art electrochemical energy storage technology for powering portable electronic devices and electric vehicles. With the introduction of high-energy, high-capacity/high-voltage cathode hosts, such as NCA and NCM811, and better electrolytes, etc., the specific energy densities of Li-ion batteries have almost tripled in the past decade. These breakthroughs in Li-ion battery technology have enabled the range and charging speed evolution of electric vehicles. [3]

Despite the significant improvements in Li-ion battery technology over the past years, further increases in their energy density are limited by the theoretical energy density values of Li-ion batteries [4], making them not well-suited for some burgeoning applications, such as grid-scale energy storage and electric flights, where longer duration and higher power capabilities are required.

With growing demand for future energy storage, it is necessary to go beyond Li-ion batteries and explore alternative battery chemistries, such as solid-state batteries, lithium-sulfur and lithium-air batteries, etc. The theoretical energy density values of these emerging battery technologies are of one order of magnitude higher than the Li-ion batteries currently in use, making them promising candidates for meeting the energy storage needs of the future.

1.2   Challenges for future batteries

The research activities in the field of battery technology aim to answer several key
questions: What is the upper limit of energy density that batteries can achieve? How
quickly can batteries be charged while maintaining their performance and safety? Can
batteries be made completely safe, without risk of overheating, explosion, or other
hazards? Is it possible to extend battery lifespan to 10,000 cycles or 30 years? Can we
reduce the cost of batteries by a factor of three or more? These questions are closely
interdependant, and addressing one can both have positive and negative outcomes for
the others. For example, improving the battery's energy density may accelerate the
battery's charging speed but it would sacrifice battery's safety and longevity while
adding extra cost. Thus, it is essential to approach these questions with a holistic
perspective and consider the potential trade-offs or downsides of different solutions.
There are practical challenges that arise when seeking answers to these questions.

- Porous electrodes present several challenges for optimal design. Achieving the
  best pore structure for the electrode requires improved characterization and
  modeling of effective electronic and ionic transport in the composite electrode,
  which includes both active material and carbon binder domains. Unfortunately,
  little attention has been paid to the effects of the carbon binder domain on ionic
  transport in the electrode. Furthermore, side reactions and structural degrada-
  tion can further complicate matters. For example, the growth of a passivation
  layer can decrease pore size or even cause clogging of pores, which impedes
  ion transport [5, 6]. Additionally, active material loss due to transition metal
  dissolution [7, 8], particle isolation, and particle structure distortion during
  charging/discharging cycles can lead to a reduction in cell capacity [9].

- The theoretical specific capacity of a Li-metal anode (3,860 mAh/g), sodium-
  metal anode (1,165 mAh/g), or silicon anode (4,200 mAh/g) is significantly
  higher than that of a graphite anode (372 mAh/g). However, the use of high-
  capacity metal or silicon anodes in batteries is associated with several severe
  challenges. Dendrite growth is a serious issue that can occur during charging,

as dendrites grow from the anode to the cathode, causing a short circuit and potentially resulting in a fire. Dead Li, sodium or silicon can accumulate during discharging due to ununiform stripping, resulting in capacity degradation of the battery. The problem of dendrite formation is not limited to a specific type of battery and is observed in batteries with different chemistries such as Li-metal, Li-sulfur, Li-air, sodium-air, sodium-sulfur, silicon-sulfur, and silicon-air batteries. Dendrite growth is worsened during fast charging. Batteries with metal or silicon-based anodes also suffer from huge volume expansion. For example, silicon-based anodes can experience a maximum volume expansion of up to 400%, resulting in mechanical degradation of the anode and decreased battery performance.

- One of the greatest challenges associated with liquid electrolytes that use organic solvents is their limited temperature stability, high volatility and flammability. This can pose safety risks, as the electrolyte and organic solvent can decompose and emit gases that increase the pressure within the cell, which can eventually lead to thermal runaway. When this happens, the temperature within the cell rises rapidly, leading to overcharging and potentially an explosion [10].

- All-solid-state batteries are considered as promising next-generation high energy density batteries with improved safety compared to liquid electrolyte batteries. However, there are several fundamental challenges that must be overcome for the widespread adoption of solid electrolytes. These include the poor electrode/electrolyte interfacial contact for ceramic electrolytes, low ionic conductivity for polymer electrolytes, and difficulties in large-scale manufacturing, among others. One of the most significant challenges that must be addressed is the formation and growth of dendrites, which can cause degradation of all-solid-state batteries, just as they do for Li-metal batteries.

In addition to the above-mentioned challenges, the formation and stability of the solid-electrolyte interphase (SEI) layers, the cracking and fracture of the active materials due to repeated expansion and contraction during charging and discharging

cycles and thermal effects also pose significant challenges for high energy density batteries.

Researchers are actively exploring various strategies to tackle with these issues, including the development of new electrolyte formula, artificial SEI or interfacial buffer layers, three-dimensional electrode structures, and the use of additives, doping and coating to improve electrode stability and prevent dendrite growth. These approaches hold promise for developing safer and more efficient high-capacity batteries. However, a large portion of the current state-of-the-art in battery research including the above-mentioned strategies for improving battery performance relies on the trial-and-error approach. In addition to the large cost incurred, there are challenges and limitations in these experimental studies. For example, it is very hard to resolve the internal physics of dendrite growth inside the battery through experiments because dendrites are too delicate for post-mortem analysis, and designing an optically transparent battery is technically difficult [11]. It is also very challenging to isolate the effects of different mechanisms that control dendrite growth based on battery performance.

The understanding of these problems can be improved through mathematical modeling to isolate and couple the competing physics during battery operation. The aim of this dissertation is to address these above-mentioned challenges through mathematical modeling and simulations, providing a quantitative assessment of battery performance, and offering mechanistic insights into battery design and material selection.

1.3   Multi-scale, multi-physics battery modeling

Batteries are complex systems that involve multiple physical and electrochemical processes at various length and time-scales. Figure 1.2 illustrates the different computational methods available for battery modeling, ranging from electronic structure methods and molecular dynamics simulations at the atomistic level [12], to system-level simulations for battery packs and state estimation at larger scales [13].

Electronic structure methods, such as conventional and linear-scaling Density Functional Theory (DFT), are employed to model the thermodynamic properties,

electronic structures, reaction kinetics, and ion transport paths of electrodes/electrolytes for batteries [14]. These methods provide valuable insights into the atomistic and electronic processes that govern energy and power densities in batteries. Classical molecular dynamics simulations are commonly used to investigate the dynamics and structure of materials, enabling the study of defect formation and evolution in batteries. These simulations can provide insights into the thermodynamics and kinetics of atomic and molecular processes, such as diffusion and phase transitions, and can be used to explore the behavior of complex materials under different conditions. However, a more detailed understanding of the complex interactions between electrochemistry and transport phenomena occuring at fluid/solid interfaces requires modelling of larger systems, and these small scale methods, such as DFT and molecular dynamics simulations are too computationally expensive to resolve the pore-scale effects. System-level simulations, on the other hand, are used to model battery packs and to predict their behavior under different operating conditions, and estimate the state of the battery such as state of health and state of charge while ignoring the internal pore-scale physics and electrochemistry.

Therefore, our focus is on the microscopic to macroscopic scales, ranging from microns to millimeters, and sometimes even including the nano-scale, to simulate spatiotemporally varying fields such as ion concentration and electric potential distribution. The challenge lies in the gap between these two scales: how do the interfaces, fluid-solid interactions, mass, charge, and heat transport in the microstructures affect battery performance at the device scale? This is an area that is least studied in the field, but it is crucial for the next breakthrough in battery technologies.

1.4   Theory-guided design of battery materials

By improving our understanding of the complex interactions between electrochemical processes and transport phenomena across different scales, this dissertation aims to approach the technical challenges mentioned in Section 1.2 with a holistic perspective and provide mechanistic insights into the optimal design of battery materials. A key objective is to bridge the gap between micro-scale and macro-scale phenomena,
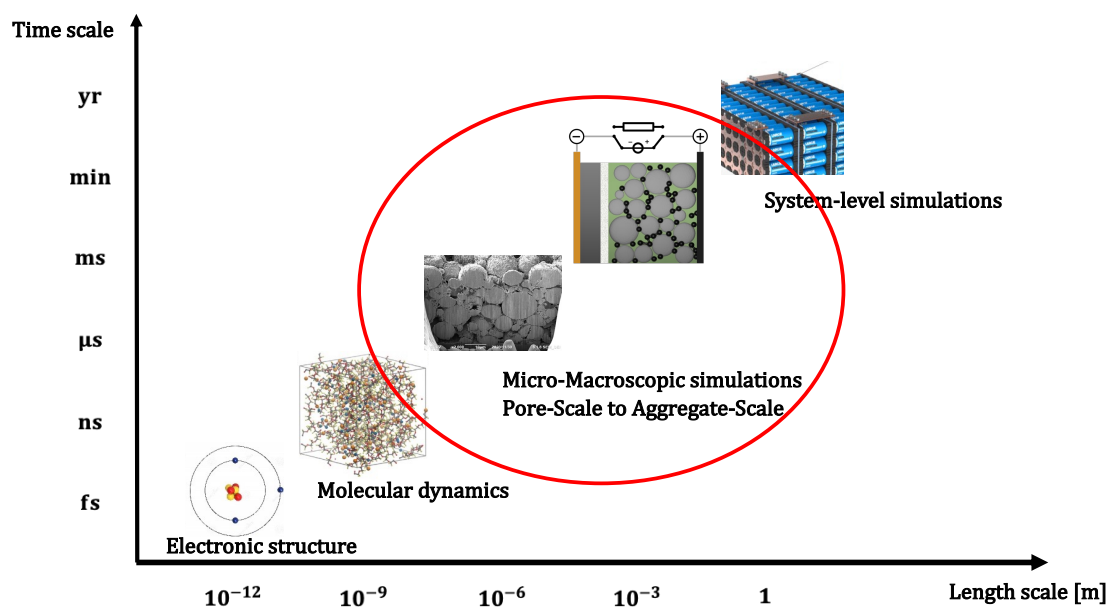
Figure 1.2: Different computational methods available for battery modeling, ranging from electronic structure methods and molecular dynamics simulations at the atomistic level, to system-level simulations for battery packs and state estimation at larger scales. We focus on bridging the microscopic transport phenomena to the cell-level battery performance, which is circled in red.

establishing a connection between pore-scale physics and overall cell performance.

Figure 1.3 serves as an overview of the modeling framework utilized in this dissertation, illustrating the various scales at which the associated problems are investigated. These problems encompass the modeling of the porous cathode in Li-ion/Li-metal batteries at the single particle scale and at the aggregate scale (Chapter 2 and Chapter 3), as well as the study of dendrite formation at the Li metal anode in Li-metal batteries and all-solid-state batteries (Chapter 4 and Chapter 5). These modeling efforts are conducted in close collaboration with experimentalists and industrial partners who contribute material characterization and observation of battery performance. These interactions ensure that these models account for correct physics and chemistry. Ultimately, this modeling framework provides theoretical guidelines for the optimal design of porous cathodes, Li-metal anodes, electrolytes, separator

pore structures and dendrite-suppressing buffer layers between the lithium-metal an-
ode and electrolyte.
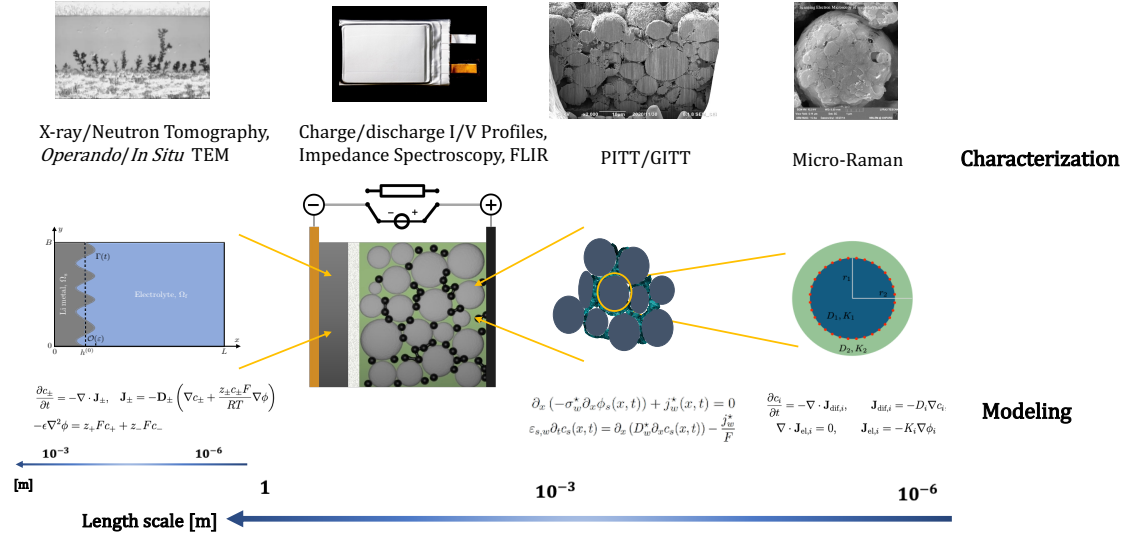
Figure 1.3: Observation-inspired battery modeling and simulation at various length
scales.

1.5 Dissertation outline

The dissertation is organized as follows.

Chapter 1 provides an introduction to the research topic, focusing on the chal-
lenges involved in the design of high energy density batteries. It emphasizes the
importance of achieving a comprehensive understanding of electrochemical processes
and transport phenomena across different scales, ranging from the micro to macro
levels. The chapter discusses the significance of bridging the gap between these scales
and the potential impact on improving the performance of high energy density bat-
teries. By highlighting the key challenges and research gaps, it sets the foundation
for the subsequent chapters, which aim to address these issues through modeling and
simulation approaches.

In Chapter 2, we focus on the development of an effective model for mass and charge transport in the composite electrode, specifically considering the composite spherical particle consisting of active material and carbon binder domain. The presence of the carbon binder domain in the electrode impacts ionic transport and reduces the active surface area, affecting battery performance. We derive equivalent electrical conductivity, ionic diffusivity, and reaction parameters in the Butler-Volmer equation for the homogeneous counterpart of the composite particle. These equivalent characteristics are defined to ensure that the same mass and charge enter the composite and homogenized spheres. We analyze the time-dependent behavior of the effective diffusion coefficient and reaction parameters, which exhibit a two-stage behavior characterized by the reaction delay time. At later times, these characteristics become time-independent and can be expressed using closed-form formulas. These expressions provide simplicity and facilitate their application in the modeling of Li-ion and Li-metal batteries. The work in Chapter 2 has been published in *Journal of The Electrochemical Society* in 2022 [15].

In Chapter 3, we delve into the analysis of parameterization strategies for pseudo-2-dimensional models used to predict the lithiation curves in lithium batteries, considering the challenges posed by the carbon binder domain. We propose two alternative strategies for parameterization that explicitly account for the volume of the carbon binder domain. The first strategy involves aggregating the carbon binder domain with the electrolyte-filled pore space and expressing the Bruggeman exponent through a solution of a microstructure-specific closure problem. The second strategy treats the carbon binder domain and active particles as a composite solid phase, leveraging the effective properties derived in Chapter 2 to compute their properties (semi-)analytically. We demonstrate that parameterizing the Doyle-Fuller-Newman model with the homogeneous properties derived in Chapter 2 strikes a balance between model complexity and prediction accuracy. Through our modeling efforts, we investigate the dependency of battery discharge time on the volume fraction, ionic conductivity, and diffusion coefficient of the carbon binder domain. Our findings provide valuable insights that can be utilized in the optimal design of porous cathodes. The work presented in this chapter builds upon the foundation laid in Chapter 2

and contributes to the overall objective of the dissertation, which is to bridge the gap between micro-scale and macro-scale phenomena and provide mechanistic insights for the optimal design of battery materials. The work in Chapter 3 has been published in *Journal of The Electrochemical Society* in 2022 [16].

Chapter 4 of this dissertation addresses the challenge of dendritic growth in Li-metal batteries. We present a linear-stability analysis that utilizes the Poisson-Nernst-Planck equations to describe Li-ion transport, accounting for the lack of electroneutrality. This approach enables us to investigate the impact of electric-field gradients near the electrode surface on both ion diffusion and its anisotropy. Our analysis suggests that the use of anisotropic electrolytes, with anisotropic diffusion coefficients of the Li ions, and control of the local electric field can suppress dendritic growth of Li metal. This analysis provides a useful guide for designing new electrolytes and separators to mitigate dendritic growth, improving the safety and performance of Li-metal batteries. The work in Chapter 4 has been published in *Journal of The Electrochemical Society* in 2022 [17].

In Chapter 5, our investigation continues by examining dendrite growth in all-solid-state batteries with Li anode. One approach to mitigate dendrite growth is the insertion of a buffer layer between the Li-metal and the solid electrolyte. However, most experimental investigations of potential buffer materials are empirical and largely unassisted by quantitative predictions of Li-ion transport and electrochemical transformations in the solid electrolyte and the buffer. We propose a mathematical model of electrodeposition on the Li anode in all-solid-state lithium metal batteries with an interfacial buffer layer between the Li anode and the solid electrolyte. The model describes Li-ion transport in the electrolyte and the buffer, which is accompanied by an interfacial charge-transfer reaction. Our findings suggest new strategies for the design of interfacial buffers, i.e., for the optimal selection of buffer material and the solid electrolyte pair based on their electrochemical and physical properties. Our model's predictions regarding the dendrite suppression abilities of different buffer materials align with published experimental findings. This model can serve as a guide for experimental and computational efforts in discovering new buffer materials that are

compatible with specific electrolytes. By leveraging this analysis, researchers can accelerate the discovery and development of buffer materials for all-solid-state batteries, contributing to the advancement of safer and more reliable energy storage technologies. The work in Chapter 5 has been published in *Journal of The Electrochemical Society* in 2023 [18].

Chapter 6 serves as a comprehensive summary of the main contributions and implications presented in each chapter of this dissertation. It highlights the key findings and insights obtained throughout the research, emphasizing their significance in advancing the understanding of high-energy-density batteries. Additionally, Chapter 6 explores potential applications of the developed modeling framework and outlines promising avenues for future research in this field. In Appendix A and B, detailed descriptions of the linear stability analyses conducted for dendritic growth in both lithium-metal batteries and all-solid-state batteries are provided. These analyses offer valuable insights into the mechanisms underlying dendritic growth and its suppression, providing a deeper understanding of the challenges associated with these battery systems.

I have also made additional contributions in other research areas, including biomedical modeling and environmental applications, during my Ph.D. study at Stanford University. These works have been published in *Water Resources Research* in 2021 and 2023 [19, 20] and *Journal of Applied Physiology* in 2021 [21]. As this dissertation focuses solely on high-energy-density batteries, the specific details of these studies are not included here.

Chapter 2

Effective representation of active material and carbon binder in porous electrodes

2.1 Abstract

Active cathode material and graphite anode material are routinely mixed with conductor and binder to improve the electric conductivity and mechanical stability of electrodes. Despite its benefits, this carbon binder domain (CBD) impedes ionic transport and reduces the active surface area, thus impacting the battery performance. We consider a composite spherical particle, whose active-material core is coated with CBD, and its homogeneous counterpart, for which we derived equivalent electrical conductivity, ionic diffusivity, and reaction parameters in the Butler-Volmer equation. These equivalent characteristics are defined to ensure that the same mass and charge enter the composite and homogenized spheres. They are expressed in terms of the volume fraction of the active material and transport properties of the active material and CBD. In general, the equivalent effective diffusion coefficient and reaction parameters are time-dependent and exhibit two-stage behavior characterized by the reaction delay time. At later times, these characteristics are time-independent

and given explicitly by closed-form formulae. The simplicity of these expressions facilitates their use in single- and multi-particle representations of Li-ion and Li-metal batteries.

2.2 Introduction

Rechargeable Li-ion and Li-metal batteries are among the most effective and promising energy storage devices for portable electronics and electric vehicles. While their anode materials differ (graphite and Li metal in the case of Li-ion and Li-metal batteries, respectively), both battery types use the same lithium intercalation cathode materials [2], such as lithium cobalt oxide, lithium nickel manganese cobalt oxide, lithium manganese oxide, or lithium iron phosphate. Continued improvement of porous cathodes requires the ability to model both microscopic (pore-scale) electrochemical processes and their impact on battery performance.

Active cathode material particles, as well as graphite anode material particles, are often mixed with conducting material (e.g., carbon black) and binder to improve the electric conductivity and mechanical stability of electrodes [22, 23, 24, 25]. During the manufacturing process, conductive additive and binder form the so-called carbon binder domain (CBD), a mixed phase surrounding active particles. Despite its benefits, CBD impedes ionic transport in the electrode by increasing the tortuosity of diffusion pathways and reducing the active surface area, thus impacting the battery performance [26, 27, 28].

Advances in imaging techniques have enabled one to resolve the spatial extent of CBD in a composite electrode [29, 26, 28, 30, 31]. This, in turn, made it possible to assess the impact of CBD on effective transport properties either via direct tortuosity [27, 31] and impedance [32] measurements, or via microstructure-resolving simulations of Li-ion transport and electrochemical transformations [29]. Although such pore-scale models accurately capture the relevant processes in tiny volumes comprising a few CBD-coated active particles and electrolyte, they are too computationally expensive to be used at the device scale. This motivated the development of their macroscopic counterparts such as the single particle models (SPMs) [33, 34, 35, 36],

the Doyle-Fuller-Newman (DFN) model [37] or homogenized models [38, 39, 40]. These and similar macroscopic models seldom account for the presence of CBD. A notable exception is the study [8] that used charge transfer resistance measurements to relate changes in the reaction rate constant to changes in the volume fractions of active material and CBD in the cathode, although ionic transport in CBD was ignored.

Yet, the latter is of paramount importance to battery performance. For example, the overall electrode ionic conductivity is more strongly tied to the volume fraction and ionic conductivity of CBD than to its overall porosity [26]. This suggests the need for a mathematical model that relates measurable characteristics of active particles and CBD, such as their volume fractions and transport properties (diffusion coefficients, ionic conductivities, etc.) to the bulk properties of the composite electrode material (effective diffusion coefficients, ionic conductivities, etc.).

Complex microstructures of composite materials can be represented via an assemblage of coated spheres [41]. This strategy can be used to model the composite electrode as collection of spherical grains of active material coated by CBD, with resulting pores filled by electrolyte. For linear systems, the Hashin-Shtrikman bounds provide the effective conductivity bounds for an isotropic two-component material composed of coated spheres [42], while the Wiener arithmetic and harmonic means give the upper and lower bounds for the effective conductivity of anisotropic media with multiple components [41]. These theoretical results have impacted a wide range of linear and nonlinear problems, [43, 44, 45] but are of limited use in battery modeling, since they do not guarantee the mass and charge conservation in the presence of ion intercalation into active particles.

Our study fills this void by presenting an equivalent/homogenized model of ion transport and intercalation for a spherical active particle coated by CBD and immersed into electrolyte under galvanostatic condition. The model conserves mass and charge, and results in semi-analytical expressions for equivalent ionic conductivity, diffusion coefficient, and reaction rate of the composite (active material / CBD) particle. These equivalent characteristics are expressed in terms of the volume fractions and transport properties of the constitutive phases; they take the closed form at large

times. Our results for a CBD-coated $LiNi_{0.6}Mn_{0.2}Co_{0.2}O_2$ (NMC622) active particle with the volume fraction of 0.8, 0.85, and 0.9 exhibit the relative error in Li ion accumulation of less than 1% for C rates ranging from 0.1C to 10C.

Our effective model is important in its own right when used in the single-particle models. It also can serve as input for the DFN model and homogenized macroscopic dual-continua models. Hence, it is of direct relevance to cell-level performance simulation and optimization.

2.3 Problem formulation

Continuum or Darcy-scale treatments of porous media represent irregular grains and complex pore structures as ordered assemblages of regular shaped objects e.g., periodic arrangements of spheres or ellipses. [41, 46, 40] That is because any structural irregularity averages out over a representative elementary volume that contains thousands or millions of grains. With that in mind, we consider a spherical active particle of radius r_1 that is coated with the CBD layer, giving rise to the composite sphere of radius r_2 (Figure 2.1). The active material has diffusion coefficient D_1 (m^2/s) and ionic conductivity K_1 (S/m); the corresponding quantities for CBD are denoted by D_2 and K_2. Li-ion intercalation takes place at the active particle's surface, i.e., at $r = r_1$. The sphere is immersed into the electrolyte with Li-ion concentration c_e and electric potential ϕ_e; a uniform electric field $\mathbf{E}$ in the x direction represents the electric field in a working battery's electrode. Indeed, visualization of the electric potential distribution across working devices shows the electric potential profile in the porous electrode has an approximately linear slope, which corresponds to a uniform electric field, $\mathbf{E} = -\nabla\phi_e$. [47] The single particle model [33] predicts a similar linear electric potential distribution in the electrode.

An equivalent representation of this composite particle is a homogeneous sphere of radius r_2 that has diffusion coefficient D^*, ionic conductivity K^*, and ion intercalation at its surface. These characteristics are such that the two spheres have the same current density and ion flux through their respective surfaces. Our goal is to express these equivalent parameters in terms of the volume fractions ($V_1 = r_1^3/r_2^3$ and $V_2 =$
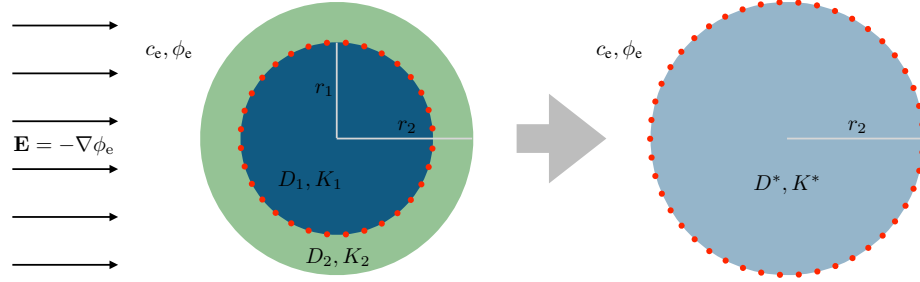
Figure 2.1: **Left:** Spherical composite particle of radius r_2 comprising an active material core of radius r_1 coated with a CBD layer. The active material has diffusion coefficient D_1 and ionic conductivity K_1; the corresponding quantities for CBD are denoted by D_2 and K_2. **Right:** Its homogeneous counterpart with equivalent diffusion coefficient D^* and ionic conductivity K^*. The red lines denote locations of the intercalation surface. The sphere is immersed in the electrolyte with Li-ion concentration c_e, electric potential ϕ_e, and uniform electric field $\mathbf{E} = -\nabla\phi_e$.

$1 - V_1$) and transport properties of each phase.

2.3.1 Transport in active core and CBD coating

Given the geometry of the composite particles, we use the spherical coordinate system $\mathbf{r} = (r, \theta, \varphi)^{\top}$. Spatiotemporal evolution of the molar concentrations of Li ions (mol/m^3) in the active material, $c_1(\mathbf{r}, t)$ with $0 \leq r \leq r_1$, and the CBD coating, $c_2(\mathbf{r}, t)$ with $r_1 \leq r \leq r_2$, is described by the diffusion equations [32]:

$$\frac{\partial c_i}{\partial t} = -\nabla \cdot \mathbf{J}_{\mathrm{dif},i}, \qquad \mathbf{J}_{\mathrm{dif},i} = -D_i \nabla c_i, \qquad i = 1, 2. \qquad (2.1)$$

The corresponding electrical potentials (V) in each phase, $\phi_1(\mathbf{r}, t)$ with $0 \leq r \leq r_1$ and $\phi_2(\mathbf{r}, t)$ with $r_1 \leq r \leq r_2$, are governed by the Laplace equations

$$\nabla \cdot \mathbf{J}_{\mathrm{el},i} = 0, \qquad \mathbf{J}_{\mathrm{el},i} = -K_i \nabla \phi_i, \qquad i = 1, 2. \qquad (2.2)$$

These two sets of equations are defined on $0 < r < r_1$ for $i = 1$, and on $r_1 < r < r_2$ for $i = 2$; both for time $t > 0$. They are coupled by enforcing the continuity of the radial components of the mass fluxes, $\mathbf{J}_{\mathrm{dif},i}$, and current densities, $\mathbf{J}_{\mathrm{el},i}$, at the interface

$r = r_1$: [48]

$$D_1 \frac{\partial c_1}{\partial r} = D_2 \frac{\partial c_2}{\partial r} = R_{\text{int}} \tag{2.3}$$

and

$$K_1 \frac{\partial \phi_1}{\partial r} = K_2 \frac{\partial \phi_2}{\partial r} = F R_{\text{int}}. \tag{2.4}$$

Assuming that the Butler-Volmer equation with the charge transfer coefficient of 0.5 describes the ion intercalation on the active particle surface,

$$R_{\text{int}} = 2k_1 \sqrt{c_1 c_2 \left(1 - \frac{c_1}{c_{1,\text{max}}}\right)} \sinh \left[\frac{F}{2RT}(\phi_1 - \phi_2 - U(c_1/c_{1,\text{max}}))\right], \tag{2.5}$$

where k_1 is the reaction rate constant of the active material (m/s), $c_{1,\text{max}}$ is the maximum Li concentration that could be stored in the active particle (mol/m^3), U is the open circuit potential (V) that depends on the Li filling fraction $c_1/c_{1,\text{max}}$, F is the Faraday constant (s·A/mol), R is the gas constant (J/mol/K), and T is the temperature (K).

At the interface between the composite particle and liquid electrolyte, $r = r_2$, we assume charge neutrality and the electrolyte to be dilute [48]. This gives rise to the boundary conditions at $r = r_2$,

$$D_e \frac{\partial c_e}{\partial r} + \frac{t_+^2 K_e}{F^2} \frac{\partial \mu_e}{\partial r} + \frac{K_e t_+}{F} \frac{\partial \phi_e}{\partial r} = D_2 \frac{\partial c_2}{\partial r}, \tag{2.6}$$

$$\frac{t_+ K_e}{F} \frac{\partial \mu_e}{\partial r} + K_e \frac{\partial \phi_e}{\partial r} = K_2 \frac{\partial \phi_2}{\partial r}, \tag{2.7}$$

and

$$c_e = c_2, \qquad \phi_e = \phi_2, \tag{2.8}$$

where $c_e(\mathbf{r})$ and $\phi_e(\mathbf{r})$ are respectively the Li ion concentration (mol/m^3) and electrical potential (V) in the electrolyte, $r \geq r_2$; and D_e, K_e, and t_+ denote the interdiffusion coefficient (m^2/s), the ionic conductivity (S/m), and the transfer coefficient $(-)$ of Li ions in the electrolyte, respectively. μ_e is the chemical potential of Li ions in the electrolyte and may be defined by $\mu_e = RT\log(fc_e)$, where f is the activity coefficient. The interfacial electric potential in the electrolyte (at $r = r_2$) varies with the angle

θ, in response to the uniform electrical current imposed in the x_1 direction far away from the sphere (Fig. 2.1).

The problem formulation is completed by specifying the boundary and initial conditions

$$c_1(r = 0, t) < \infty; \qquad \phi_1(r = 0, t) < \infty; \qquad c_i(\mathbf{r}, 0) = c_{\text{in}}, \quad i = 1, 2. \tag{2.9}$$

2.3.2   Transport in equivalent particle

The equivalent model treats the composite particle as a homogeneous material with equivalent diffusion coefficient D^* and equivalent ionic conductivity K^* (Figure 2.1). Equations (2.1) and (2.2) are replaced with

$$\frac{\partial c}{\partial t} = D^* \nabla^2 c, \qquad K^* \nabla^2 \phi = 0, \tag{2.10}$$

and describe the spatiotemporal evolution of Li concentration, $c(r, t)$, and electric potential, $\phi(r, t)$, in the whole particle, i.e., for $0 < r < r_2$. To ensure that the same Li ion flux and the same current density enter the composite particle and its equivalent counterpart, we replace the interfacial and boundary conditions (2.3)–(2.7) with the boundary conditions at $r = r_2$,

$$D_{\text{e}} \frac{\partial c_{\text{e}}}{\partial r} + \frac{t_+^2 K_{\text{e}}}{F^2} \frac{\partial \mu_{\text{e}}}{\partial r} + \frac{K_{\text{e}} t_+}{F} \frac{\partial \phi_{\text{e}}}{\partial r} = D^* \frac{\partial c}{\partial r} = R_{\text{int}}^*, \tag{2.11}$$

$$\frac{t_+ K_{\text{e}}}{F} \frac{\partial \mu_{\text{e}}}{\partial r} + K_{\text{e}} \frac{\partial \phi_{\text{e}}}{\partial r} = K^* \frac{\partial \phi}{\partial r} = F R_{\text{int}}^*, \tag{2.12}$$

where

$$R_{\text{int}}^* = 2k^* \sqrt{c c_{\text{e}} \left(1 - \frac{c}{c_{\text{max}}} \right)} \sinh \left[\frac{F}{2RT} (\phi - \phi_{\text{e}} - U(c/c_{\text{max})}) \right], \tag{2.13}$$

k^* is the equivalent reaction rate constant, and $c_{\max}$ is the maximum Li concentration that can be stored in the homogenized particle. In analogy with (2.9), we also require

$$c(r = 0, t) < \infty; \qquad \phi(r = 0, t) < \infty; \qquad c(\mathbf{r}, 0) = c_{\text{in}}. \tag{2.14}$$

The interfacial conditions (2.6)–(2.8) and (2.11)–(2.13) should hold for all interfacial values of (gradients of) ion concentration, $c_{\text{e}}(r_2, \cdot)$, and electric potential, $\phi_{\text{e}}(r_2, \cdot)$, in the liquid electrolyte. Consequently, for the purpose of homogenization, we treat them as given rather than computed as solutions of the Nernst-Planck equations. That is in contrast to fully-resolved pore-scale simulations that comprise a couple system of equations for the active particle, CBD, and the electrolyte-filled pore space.

2.4 Equivalent models of solid phase

The equivalent representation of the composite particle in Figure 2.1 shifts the intercalation surface from $r = r_1$ to $r = r_2$. To ensure that this procedure results in global conservation of mass and charge, we introduce the following relations on the respective intercalation surfaces:

$$r_1^2 D_1 \frac{\partial c_1}{\partial r}(r_1, t) = r_2^2 D^* \mathcal{H}(t - \tau) \frac{\partial c}{\partial r}(r_2, t - \tau) \tag{2.15}$$

$$r_1^2 K_1 \frac{\partial \phi_1}{\partial r}(r_1, t) = r_2^2 K^* \mathcal{H}(t - \tau) \frac{\partial \phi}{\partial r}(r_2, t - \tau), \tag{2.16}$$

where $\mathcal{H}(\cdot)$ is the Heaviside function. The reaction delay time $\tau = (r_2 - r_1)^2/D_2$ accounts for the shift of the reaction interface from the inner radius $r = r_1$ to the outer radius $r = r_2$. Due to the boundary conditions (2.3), (2.4), (2.11), (2.12) and the Butler-Volmer relations (2.5) and (2.13), the two interfacial conditions (2.15) and (2.16) collapse into one:

$$r_1^2 R_{\text{int}}(r_1, t) = r_2^2 \mathcal{H}(t - \tau) R_{\text{int}}^*(r_2, t - \tau). \tag{2.17}$$

This definition of the equivalent Butler-Volmer rate is automatically satisfied by imposing the following relations on the respective intercalation surfaces:

$$\phi_1(r_1, t) - \phi_2(r_1, t) = \phi(r_2, t) - \phi_e(r_2, t), \tag{2.18a}$$

$$\frac{c_1(r_1, t)}{c_{1,\text{max}}} = \mathcal{H}(t - \tau)\frac{c(r_2, t - \tau)}{c_{\text{max}}^*}, \tag{2.18b}$$

$$r_1^2 k_1 \sqrt{c_{1,\text{max}} c_2(r_1, t)} = r_2^2 k^* \mathcal{H}(t - \tau)\sqrt{c_{\text{max}}^* c_e(r_2, t - \tau)}. \tag{2.18c}$$

These relations define the equivalent parameters c_{max} and k^*.

2.4.1   Equivalent ionic conductivity

Our derivation of the equivalent ionic conductivity K^* follows that of the coated sphere model [41]. The key difference between our problem and the model [41] is that the interface between the two materials is now reactive. Consequently, we replace the continuity of electric potential at $r = r_1$ with the potential-drop condition (2.18a) and enforce the charge conservation condition (2.16).

Assuming the azimuthal symmetry, we rewrite the Laplace equations (2.2) and (2.10) in polar coordinates $\mathbf{r} = (r, \theta)^\top$ and look for their solutions, $\phi_i(\mathbf{r})$ with $i = 1, 2$ and $\phi^*(\mathbf{r})$, in the form $\phi_1 = a_1 r \cos\theta$ for $0 \leq r \leq r_1$; $\phi_2 = (a_2 r + b_2/r^2)\cos\theta$ for $r_1 \leq r \leq r_2$; and $\phi^* = a\, r \cos\theta$ for $0 < r < r_2$; where a_1, a_2, b_2, and a are the constants of integration. These are obtained from the conditions of continuity of the radial components of the current densities $\mathbf{J}_{\text{el},1}$ and $\mathbf{J}_{\text{el},2}$ at $r = r_1$ in Eq. (2.4),

$$K_1 a_1 = K_2(a_2 - 2b_2/r_1^3); \tag{2.19}$$

and of the radial components of the current densities $\mathbf{J}_{\text{el},2}$ and $\mathbf{J}_{\text{el}}^*$ at $r = r_2$ in Eqs. (2.7) and (2.12),

$$K^* a = K_2(a_2 - 2b_2/r_2^3). \tag{2.20}$$

The remaining two equations arise from the conservation of charge, Eq. (2.16),

$$r_2^2 K^* a = r_1^2 K_1 a_1;$$
(2.21)

and the drop of the electrical potential across the reaction interfaces, Eqs. (2.18a) and (2.8),

$$a_1 r_1 - (a_2 r_1 + b_2/r_1^2) = a\, r_2 - (a_2 r_2 + b_2/r_2^2).$$
(2.22)

The system of linear algebraic equations (2.19)–(2.22) has a nontrivial solution if and only if

$$K^* = \frac{2K_1 K_2}{K_1 \dfrac{r_2/r_1 - 1}{1 - r_1 r_2/(r_1 + r_2)^2} + 2K_2 r_2/r_1} = \frac{2K_1 K_2}{K_1 \dfrac{V_1^{-1/3} - 1}{1 - V_1^{1/3}/(V_1^{1/3} + 1)^2} + 2K_2/V_1^{1/3}}.$$
(2.23)

If the sphere consists entirely of the active material, i.e., if $V_1 = 1$, then this expression reduces to $K^* = K_1$, as it should.

2.4.2   Equivalent diffusion coefficient

The subsequent analysis is facilitated by considering galvanostatic conditions, under which a constant current I_a (corresponding to the current density $J = I_a/(4\pi r_2^2)$ is applied at the sphere's surface, $r = r_2$. Then, the boundary conditions (2.6) and (2.11) are replaced with

$$D_2 \frac{\partial c_2}{\partial r}(r_2, t) = \frac{I_a}{4\pi r_2^2 F} \quad \text{and} \quad D^* \frac{\partial c}{\partial r}(r_2, t) = \frac{I_a}{4\pi r_2^2 F},$$
(2.24)

and the solutions to the corresponding boundary value problems are independent from the azimuth and polar angles, $c_i = c_i(r, t)$ with $i = 1, 2$, and $c = c(r, t)$. Without loss of generality, we set the initial concentration to $c_{\text{in}} = 0$ (otherwise, one can repeat our analysis for $c_i - c_{\text{in}}$ and $c - c_{\text{in}}$).

Solution for composite sphere

Given the azimuth and polar symmetry, Eqs. (2.1) take the form

$$\frac{\partial c_i}{\partial t} = \frac{D_i}{r^2} \frac{\partial}{\partial r}\left(r^2 \frac{\partial c_i}{\partial r}\right), \qquad i = 1, 2. \tag{2.25}$$

The transformation $u_i(r, t) = r c_i(r, t)$ turns Eq. (2.25) into

$$\frac{\partial u_i}{\partial t} = D_i \frac{\partial^2 u_i}{\partial r^2}, \qquad i = 1, 2. \tag{2.26}$$

Accounting for the initial and boundary conditions (2.9) with $c_{\text{in}} = 0$, the Laplace-transformed solutions of Eqs. (2.26) are

$$\hat{u}_1(r, \lambda) = A_1 \left(e^{-\sqrt{\lambda/D_1}\, r} - e^{\sqrt{\lambda/D_1}\, r}\right), \qquad 0 \leq r \leq r_1, \tag{2.27}$$

and

$$\hat{u}_2(r, \lambda) = A_2\, e^{\sqrt{s}\, r} + B_2\, e^{-\sqrt{s}\, r}, \qquad r_1 \leq r \leq r_2, \tag{2.28}$$

where λ is the Laplace variable, and $s = \lambda/D_2$. The constants of integration A_1, A_2, and B_2 are obtained from the Laplace transforms of the auxiliary conditions (2.3), (2.15), and (2.24),

$$D_2 \frac{\mathrm{d}\hat{c}_2}{\mathrm{d}r}(r_2, \lambda) = \frac{J}{\lambda}, \qquad D_1 \frac{\mathrm{d}\hat{c}_1}{\mathrm{d}r}(r_1, \lambda) = D_2 \frac{\mathrm{d}\hat{c}_2}{\mathrm{d}r}(r_1, \lambda) = \frac{r_2^2}{r_1^2} D_2 e^{-\lambda\tau} \frac{\mathrm{d}\hat{c}_2}{\mathrm{d}r}(r_2, \lambda). \tag{2.29}$$

$$A_1 = -\frac{J r_2^2}{F D_1 \lambda} \frac{e^{-\lambda\tau}}{(r_1\sqrt{\lambda/D_1} + 1)e^{-\sqrt{\lambda/D_1}\, r_1} + (r_1\sqrt{\lambda/D_1} - 1)e^{\sqrt{\lambda/D_1}\, r_1}}; \tag{2.30}$$

with $\beta = r_2 - r_1$, and

$$A_2 = \frac{J r_2^2}{F D_2 \lambda} \frac{e^{\beta\sqrt{s}}(r_1 + 1/\sqrt{s}) - e^{-D_2\tau s}(r_2 + 1/\sqrt{s})}{(r_2 - 1/\sqrt{s})e^{\beta\sqrt{s}}(r_1\sqrt{s} + 1) - (r_1 - 1/\sqrt{s})e^{-\beta\sqrt{s}}(r_2\sqrt{s} + 1)} e^{-r_2\sqrt{s}} \tag{2.31}$$

$$B_2 = \frac{J r_2^2}{F D_2 \lambda} \frac{e^{-\beta\sqrt{s}}(r_1 - 1/\sqrt{s}) - e^{-D_2\tau s}(r_2 - 1/\sqrt{s})}{(r_2 - 1/\sqrt{s})e^{\beta\sqrt{s}}(r_1\sqrt{s} + 1) - (r_1 - 1/\sqrt{s})e^{-\beta\sqrt{s}}(r_2\sqrt{s} + 1)} e^{r_2\sqrt{s}}. \tag{2.32}$$

We rewrite (2.27)–(2.32) as (2.33). Then, the Laplace-transformed solutions of the diffusion equations (2.1), written in the spherical coordinates and subject to the auxiliary conditions (2.3), (2.9), (2.15) and (2.24) are

$$\hat{c}_1(r, \lambda) = \frac{Jr_2^2}{FD_1 r \lambda} \alpha_1 (e^{r\sqrt{\lambda/D_1}} - e^{-r\sqrt{\lambda/D_1}}), \qquad 0 \leq r \leq r_1, \tag{2.33a}$$

$$\hat{c}_2(r, \lambda) = \frac{Jr_2^2}{FD_2 r \lambda} \left[\alpha_2 e^{-(r_2-r)\sqrt{s}} + \beta_2 e^{-(r-r_1)\sqrt{s}} \right], \qquad r_1 \leq r \leq r_2, \tag{2.33b}$$

where λ is the Laplace-transform variable, $s = \lambda/D_2$, $\beta = r_2 - r_1$, and

$$\alpha_1 = \frac{e^{-\lambda\tau}}{(r_1\sqrt{\lambda/D_1} + 1)e^{-r_1\sqrt{\lambda/D_1}} + (r_1\sqrt{\lambda/D_1} - 1)e^{r_1\sqrt{\lambda/D_1}}}, \tag{2.33c}$$

$$\alpha_2 = \frac{r_1 + 1/\sqrt{s} - e^{-D_2\tau s - \beta\sqrt{s}}(r_2 + 1/\sqrt{s})}{(r_2 - 1/\sqrt{s})(r_1\sqrt{s} + 1) - (r_1 - 1/\sqrt{s})e^{-2\beta\sqrt{s}}(r_2\sqrt{s} + 1)}, \tag{2.33d}$$

$$\beta_2 = \frac{e^{-\beta\sqrt{s}}(r_1 - 1/\sqrt{s}) - e^{-D_2\tau s}(r_2 - 1/\sqrt{s})}{(r_2 - 1/\sqrt{s})(r_1\sqrt{s} + 1) - (r_1 - 1/\sqrt{s})e^{-2\beta\sqrt{s}}(r_2\sqrt{s} + 1)}. \tag{2.33e}$$

We compute the inverse Laplace transforms, $c_1(r_1, t)$ and $c_2(r_2, t)$, either numerically via the subroutine INVLAP [49] from the MATLAB File Exchange or analytically for large times t and steady state, as described in Section 2.4.4.

Solution for equivalent sphere

Diffusivity of an equivalent medium is known to be time-dependent, at least at early times [50]. We account for this possibility by treating $D^* = D^*(t)$. Introducing the new dependent variable $u(r, t) = rc(r, t)$ and the rescaled time

$$T = \int_0^t D^*(t')dt', \tag{2.34}$$

we transform (2.10) into

$$\frac{\partial u}{\partial T} = \frac{\partial^2 u}{\partial r^2}, \qquad 0 < r < r_2. \tag{2.35}$$

Accounting for the boundary and initial conditions (2.14) with $c_{\text{in}} = 0$, the Laplace-transformed (with respect to T) solution of this equation is

$$\hat{u}(r, \lambda_T) = A\left(e^{-r\sqrt{\lambda_T}} - e^{r\sqrt{\lambda_T}}\right). \tag{2.36}$$

where λ_T is the Laplace-transform variable. The constant of integration A is obtained from the Laplace transform of the boundary condition (2.24),

$$\frac{\mathrm{d}(\hat{u}/r)}{\mathrm{d}r}(r_2, t) = \frac{J}{F}\int_0^\infty \frac{e^{-\lambda_T T}}{D^*(h(T))}\,\mathrm{d}T. \tag{2.37}$$

where $t = h(T)$ is given implicitly by Eq. (2.34). This step leads to

$$A = \frac{J}{F}\frac{r_2^2}{e^{r_2\sqrt{\lambda_T}} - e^{-r_2\sqrt{\lambda_T}} - r_2\sqrt{\lambda_T}(e^{-r_2\sqrt{\lambda_T}} + e^{r_2\sqrt{\lambda_T}})}\int_0^\infty \frac{e^{-\lambda_T T}}{D^*(h(T))}\,\mathrm{d}T, \tag{2.38}$$

and, ultimately, the Laplace-transformed Li-ion concentration $\hat{c}(r, \lambda_T)$ is given by

$$\hat{c}(r, \lambda_T) = \frac{Jr_2^2}{Fr}\frac{\sinh(r\sqrt{\lambda_T})}{r_2\sqrt{\lambda_T}\cosh(r_2\sqrt{\lambda_T}) - \sinh(r_2\sqrt{\lambda_T})}\int_0^\infty \frac{e^{-\lambda_T T}}{D^*(h(T))}\,\mathrm{d}T, \tag{2.39}$$

where λ_T is the Laplace-transform variable, and $t = h(T)$ is given implicitly by $T = \int_0^t D^*(t')\mathrm{d}t'$. The inverse Laplace transform, $\mathcal{L}_T^{-1}$, of $\hat{c}(r, \lambda_T)$ in (2.40) is given by the convolution,

$$c(r, T) = \frac{Jr_2^2}{Fr}\int_0^T \frac{w(r, T - \nu)}{D^*(h(\nu))}\mathrm{d}\nu, \tag{2.40a}$$

where

$$w(r, T) = \mathcal{L}_T^{-1}\left\{\frac{\sinh(r\sqrt{\lambda_T})}{r_2\sqrt{\lambda_T}\cosh(r_2\sqrt{\lambda_T}) - \sinh(r_2\sqrt{\lambda_T})}\right\}. \tag{2.40b}$$

We define $D^*(t)$ as the diffusion coefficient of the homogenized sphere that, under galvanostatic conditions (2.24), results in the surface Li-ion concentration $c(r_2, T)$ that equals the weighted average of the Li-ion concentrations on the surfaces $r = r_1$

and $r = r_2$ of the composite sphere, i.e.,

$$c(r_2, t) = V_1 c_1(r_1, t) + (1 - V_1)c_2(r_2, t). \tag{2.41}$$

This yields a nonlinear integral equation for $D^*(t)$,

$$\frac{Jr_2}{F} \int_0^T \frac{w(r_2, T - \nu)}{D^*(h(\nu))} d\nu = V_1 c_1(r_1, t) + (1 - V_1)c_2(r_2, t), \qquad T = \int_0^t D^*(t')dt'. \tag{2.42}$$

Numerical algorithm for solving $D^*(t)$

Rewrite equation (2.42) in terms of t:

$$\frac{Jr_2}{F} \int_0^t w(r_2, \int_{v'}^t D^*(t')dt')d\nu' = V_1 c_1(r_1, t) + (1 - V_1)c_2(r_2, t) \tag{2.43}$$

which is solved numerically using Algorithm 1.

2.4.3 Equivalent rate and maximum concentration

Combining (2.18b) and (2.18c) with (2.41) we obtain expressions for the remaining homogenized parameters, $c_{\max}^*(t)$ and $k^*(t)$,

$$\frac{c_{\max}^*(t)}{c_{1,\max}} = \frac{V_1 c_1(r_1, t) + (1 - V_1)c_2(r_2, t)}{c_1(r_1, t + \tau)}, \qquad \frac{k^*(t)}{k_1} = \frac{r_1^2}{r_2^2}\sqrt{\frac{c_{1,\max}c_2(r_1, t + \tau)}{c_{\max}^*(t)c_2(r_2, t)}}. \tag{2.44}$$

2.4.4 Closed-form asymptotic expressions

For large t, i.e., for small λ, the interfacial Li-ion concentrations in the composite sphere, Eq. (2.33), behaves asymptotically as

$$\hat{c}_1(r_1, \lambda) = \frac{Jr_2^2}{r_1^3 F}\left[\frac{3}{\lambda^2} - \frac{(15D_1\tau - r_1^2)}{5\lambda D_1}\right] + \mathcal{O}(\lambda^{3/2}), \tag{2.45a}$$

$$\hat{c}_2(r_2, \lambda) = \frac{Jr_2}{2D_2 F\lambda}\left[\frac{\beta^3 + 3\beta^2 r_1 + 6D_2 r_2\tau}{\beta^3 + 3\beta r_1 r_2} + \mathcal{O}(\lambda^{1/2})\right] \tag{2.45b}$$

$$\hat{c}_2(r_1, \lambda) = \frac{Jr_2^2}{2FD_2 r_1\lambda}\left[\frac{\beta^3 - 3\beta^2 r_1 + 6D_2 r_1\tau}{\beta^3 + 3\beta r_1 r_2} + \mathcal{O}(\lambda^{1/2})\right]. \tag{2.45c}$$

Algorithm 1: Numerical algorithm for computing $D^*(t)$

For $k = 1$:

1. Take the inverse Laplace transform of Eqs. (2.33) to obtain $c_1(r_1, t_1)$ and $c_2(r_2, t_1)$

2. Compute $c(r_2, t_1)$ in Eq. (2.41)

3. Solve equation $c(r_2, t_1) = \frac{Jr_2}{F} w(r_2, \frac{\Delta t}{2} D^*(t_1)) \Delta t$ for $D^*(t_1)$, where w is given by Eq. (2.40b)

For $k = 2$ to N_t:

1. Take the inverse Laplace transform of Eqs. (2.33) to obtain $c_1(r_1, t_k)$ and $c_2(r_2, t_k)$

2. Compute $c(r_2, t_k)$ in Eq. (2.41)

3. Solve for $D^*(t_k)$ from equation:

$$c(r_2, t_k) = \frac{Jr_2}{F} \sum_{j=1}^{k} w(r_2, \sum_{i=1}^{j} D^*(t_{k-i+1}) \Delta t \cdot l) \Delta t, \quad l = \begin{cases} 1/2, & \text{if } i = j \\ 1, & \text{if } i \neq j \end{cases}$$

where w is given by Eq. (2.40b)

4. Stop at the kth iteration if $t_k > \tau$ and $\left| \frac{D^*(t_k) - D^*(t_{k-1})}{D^*(t_{k-1})} \right| \leq 10^{-6}$ as D^* reaches steady state

---

Its inverse Laplace transform is

$$c_1(r_1, t) \approx \frac{Jr_2^2}{r_1^3 F} \left[-\frac{(15 D_1 \tau - r_1^2)}{5 D_1} + 3t \right], \quad \text{for large } t; \tag{2.46a}$$

$$c_2(r_2, t) \approx \frac{Jr_2}{2 D_2 F} \left\{ \frac{\beta^3 + 3\beta^2 r_1 + 6 D_2 r_2 \tau}{\beta^3 + 3\beta r_1 r_2} + \mathcal{O}(1/\sqrt{t}) \right\}, \quad \text{for large } t \tag{2.46b}$$

$$c_2(r_1, t) \approx \frac{Jr_2^2}{2 F D_2 r_1} \left\{ \frac{\beta^3 - 3\beta^2 r_1 + 6 D_2 r_1 \tau}{\beta^3 + 3\beta r_1 r_2} + \mathcal{O}(1/\sqrt{t}) \right\}, \quad \text{for large } t. \tag{2.46c}$$

Similarly, for the homogenized sphere with constant diffusion coefficient D^*, the large-time approximation of (2.40) is

$$c(r_2, t) = \frac{3J}{r_2 F} t + \frac{Jr_2}{5 D^* F}, \quad \text{for large } t. \tag{2.47}$$

Substitution of Eqs. (2.46) and (2.47) into Eq. (2.41) leads to

$$
\frac{Jr_2}{5D^*F} = -\frac{(15D_1\tau - r_1^2)J}{5D_1 r_2 F} + (1 - V_1)\frac{Jr_2}{2D_2 F}\frac{\beta^3 + 3\beta^2 r_1 + 6D_2 r_2 \tau}{\beta^3 + 3r_1 r_2 \beta}, \tag{2.48}
$$

which yields

$$
D^* = \left\{\frac{r_1^2}{D_1 r_2^2} + \frac{5V_2}{D_2}\left[\frac{(r_2 - r_1)^2 + 3(r_1 + 2r_2)(r_2 - r_1)}{2(r_2 - r_1)^2 + 6r_1 r_2} - \frac{3(r_2 - r_1)^2}{V_2 r_2^2}\right]\right\}^{-1}. \tag{2.49}
$$

Expressing this relation in terms of the volume fraction V_1 gives

$$
D^* = \left\{\frac{V_1^{2/3}}{D_1} + 5\frac{1 - V_1}{D_2}\left[\frac{(1 - V_1^{1/3})^2 + 3(V_1^{1/3} + 2)(1 - V_1^{1/3})}{2(1 - V_1^{1/3})^2 + 6V_1^{1/3}} - \frac{3(1 - V_1^{1/3})^2}{1 - V_1}\right]\right\}^{-1}. \tag{2.50}
$$

Substitution of Eqs. (2.46) into Eq. (2.44) gives

$$
\frac{c_{\max}^*(t)}{c_{1,\max}} = V_1\frac{15D_1(t - \tau) + r_1^2}{15D_1 t + r_1^2} + V_2\frac{5r_1(r_2 - r_1)}{2r_2(15D_2 t/r_1^2 + D_2/D_1)}\frac{2r_1 + 7r_2}{(r_2 - r_1)^2 + 3r_1 r_2} \tag{2.51}
$$

and

$$
\frac{k^*(t)}{k_1} = \frac{r_1^2}{r_2^2}\sqrt{\frac{r_2 + 2r_1}{7r_2 + 2r_1}}\sqrt{\frac{c_{1,\max}}{c_{\max}^*(t)}} \approx \frac{r_1^2}{r_2^2}\sqrt{\frac{r_2 + 2r_1}{7r_2 + 2r_1}}V_1 = V_1^{2/3}\sqrt{\frac{1 + 2V_1^{1/3}}{7 + 2V_1^{1/3}}}V_1. \tag{2.52}
$$

Since $t \gg \tau$ and $V_1 \gg V_2$, we obtain approximations for $c_{\max}^*$ and k^* for large t:

$$
\frac{c_{\max}^*(t)}{c_{1,\max}} \approx V_1, \tag{2.53}
$$

and

$$
\frac{k^*(t)}{k_1} \approx V_1^{7/6}\sqrt{\frac{1 + 2V_1^{1/3}}{7 + 2V_1^{1/3}}}. \tag{2.54}
$$

2.5   Results and discussion

Figure 2.2 exhibits the equivalent ionic conductivity K^*, given by Eq. (2.23), for different values of K_1 and K_2 and several volume fractions V_1 of the active material. As V_1 decreases, the composite material contains more CBD and K^* becomes progressively smaller than the ionic conductivity of the active material, K_1. For example, if CBD has ionic conductivity $K_2 = 1$ S/m and its volume fraction in the mixture is $V_2 = 0.3$, then the equivalent ionic K^* is about half of the ionic conductivity of the active material, $K_1 = 10$ S/m.
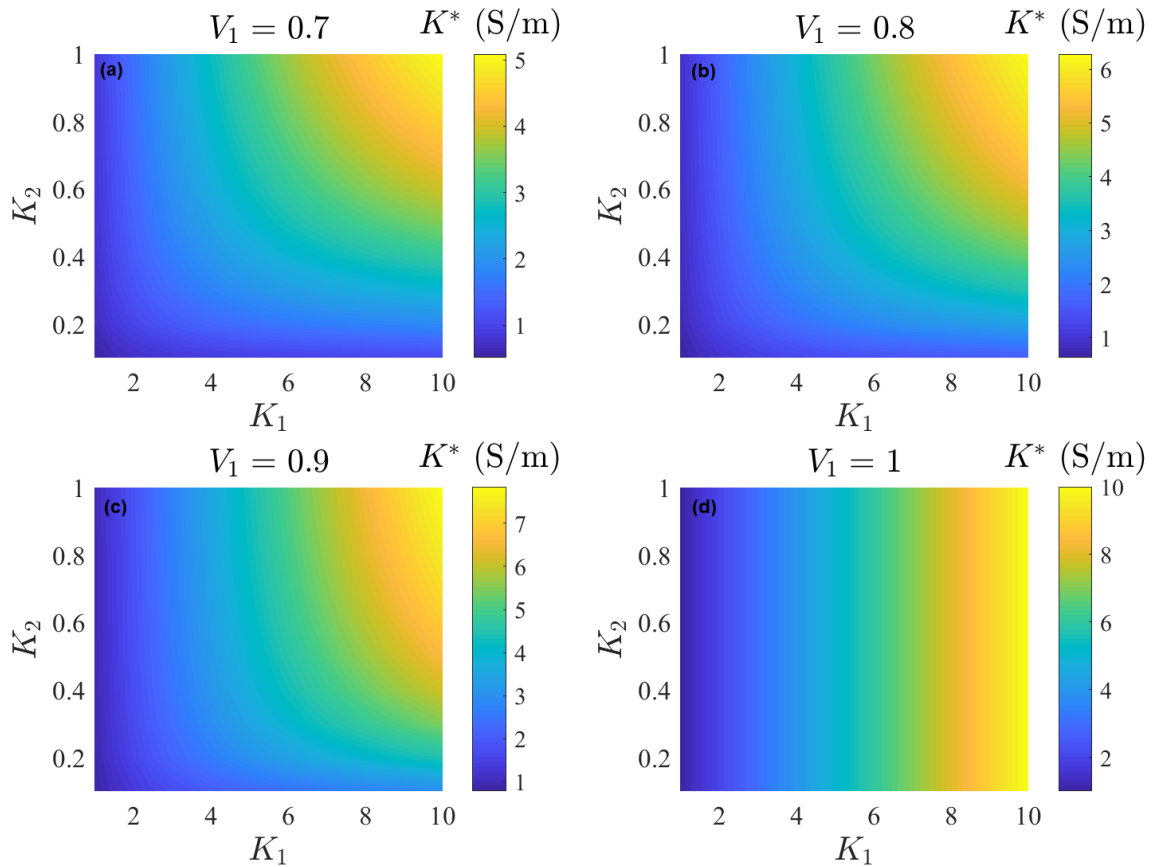
Figure 2.2: Equivalent ionic conductivity of the composite material composed of the active material and CBD with ionic conductivities K_1 and K_2, respectively. The active material's volume fraction in the mixture, V_1, is **(a)** 0.7, **(b)** 0.8, **(c)** 0.9 and **(d)** 1.

We use Algorithm 1 to solve Eq. (2.42), i.e., to compute the dimensionless equivalent diffusivity $\tilde{D}^*(\tilde{t}) = D^*/D_1$ as function of the dimensionless time $\tilde{t} = tD_1/r_2^2$. In this calculation, we use the time step $\Delta\tilde{t} = 10^{-3}$, $\tilde{t}_k = k\Delta\tilde{t}$, and MATLAB's subroutine `fsolve` with termination tolerance 10^{-6} to find the root of Eq. (2.42); the Li-ion concentrations are normalized with the maximum Li concentration in active particle $c_{1,\mathrm{max}}$ such that $\tilde{c} = c/c_{1,\mathrm{max}}$ and $\tilde{c}_i = c_i/c_{1,\mathrm{max}}$ with $i = 1, 2$; and the dimensionless current density $\tilde{J} = Jr_2/(FD_1c_{1,\mathrm{max}})$ serves as the sole input. A value of the applied current density $\tilde{J}$ does not affect the magnitude of the equivalent parameters, it only alters the values of the concentrations $\tilde{c}_i$ and $\tilde{c}$ and, thus, the time it takes the sphere to reach its maximum Li-storing capacity. To be specific, we set $\tilde{J} = 1$ in the simulation results presented below.

The results of this calculation, $\tilde{D}^* = \tilde{D}^*(\tilde{t})$, are shown in Figure 2.3 for several combinations of the active material's volume fraction V_1 and the diffusion coefficient ratios D_2/D_1. (Unless specified otherwise, we use $D_2/D_1 = 0.0178$ as a reference value [32].) The equivalent diffusivity $\tilde{D}^*(\tilde{t})$ increases at times preceding the intercalation delay time $\tilde{\tau} = (r_2 - r_1)^2 D_1/(D_2 r_2^2)$; drops appreciably at $\tilde{t} = \tilde{\tau}$; and then increases a bit to reach its steady-state value. The time to steady state decreases with V_1 (Fig. 2.3a); for $V_1 = 0.99$, CBD's volume fraction is so small that $\tilde{D}^* \approx 1$, as expected. The chemical composition of CBD, as encapsulated in the value of the diffusion coefficient D_2, affects the transitional behavior and the steady state value of D^* (Fig. 2.3b).

Figure 2.4 shows that the analytical expression (2.50) for $\tilde{D}^*$ is in close agreement with the numerical solution of Eq. (2.42) for the volume fraction V_1 ranging from 0.1 to 1.0. The close agreement between the two solutions serves to verify the accuracy of the numerical solution of Eq. (2.42). It also suggests the possibility of using the readily computable expression (2.50) as the value of the equivalent diffusivity of composite spheres in battery-scale models.

It is worthwhile to compare our analytical expression for $\tilde{D}^*$ in Eq. (2.50) with the Wiener lower bound,

$$D_{\mathrm{W}}^* = (V_1/D_1 + V_2/D_2)^{-1}. \tag{2.55}$$
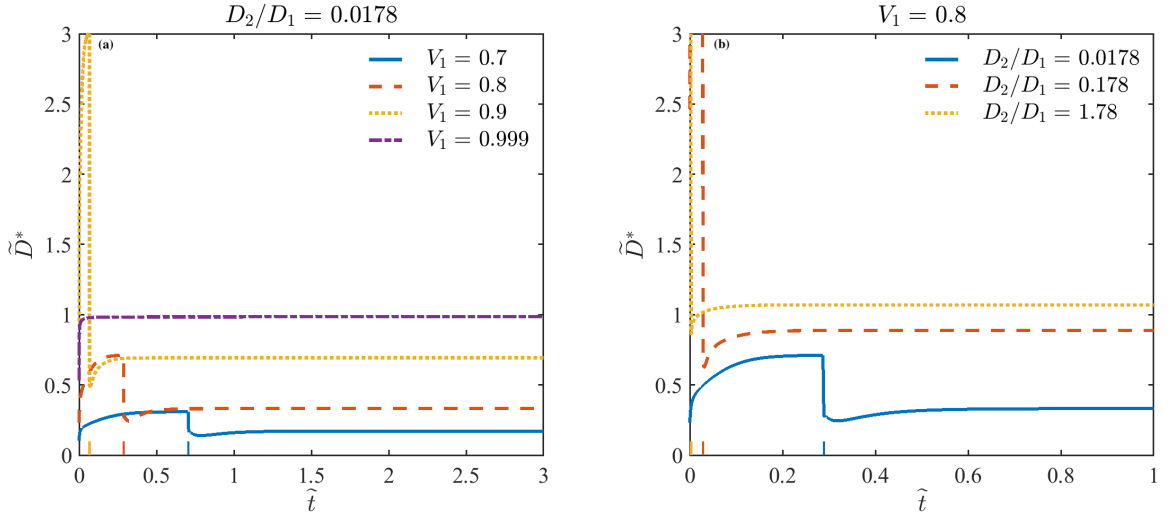
Figure 2.3: Temporal evolution of the normalized equivalent diffusivity $\tilde{D}^*(\tilde{t})$ for **(a)** several volume fractions of the active material, V_1, and $D_2/D_1 = 0.0178$; and **(b)** several diffusion coefficient ratios D_2/D_1 and $V_1 = 0.8$. The elevated tick marks indicate the dimensionless intercalation delay time $\tilde{\tau} = (r_2 - r_1)^2 D_1/(D_2 r_2^2) = 0.706$, 0.289 and 0.067 for $V_1 = 0.7$, 0.8 and 0.9, respectively.

Both are weighted harmonic means of D_1 and D_2, but with different weights. The weights in the Wiener bound are the volume fractions of the two materials, while those in our expression are more evolved because they account for Li-ion intercalation. Figure 2.4 shows that our expression for the equivalent diffusivity given by our expression (2.50) is considerably more accurate than its counterpart predicted by the Wiener bound (2.55) for the full range of the active material's volume fraction V_1 (Figure 2.4). The latter's error is highest when $0.8 < V_1 < 0.95$, which is a typical range for the volume fraction of active material in most electrodes. This result highlights the advantage of using Eq. (2.50) for battery modeling as a means to guarantee the mass and charge conservation in the presence of ion intercalation in active particles.

For the equivalent diffusion coefficient $\tilde{D}^*$ computed analytically via the closed-form expression (2.50) to be useful in battery-scale models, it must provide an accurate approximation of the Li-ion flux through the composite sphere's surface, $J_{\mathrm{dif}}(r_2, t) = -D_2 \partial_r c_2(r_2, t)$, i.e., it must conserve mass. Note that the effective model with time-dependent $D^*(t)$ in (2.42) is mass-conservative by construction, so that the
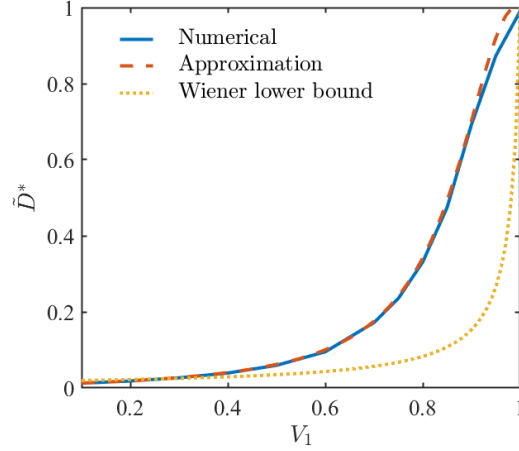
Figure 2.4: Steady-state effective diffusion coefficient $\tilde{D}^*$ alternatively computed as the numerical solution of Eq. (2.42), the analytical expression (2.50) and the Wiener lower bound (2.55). It is plotted as function of the active material's volume fraction V_1, for $D_2/D_1 = 0.0178$.

replacement of $D^*(t)$ with its steady-state counterpart D^* in (2.50) is the only source of error. Let $J^*_{\text{dif}}(r_2, t) = -D^*\partial_r c(r_2, t)$ denote the Li-ion flux through the surface of a homogeneous sphere whose diffusion coefficient D^* is given by Eq. (2.50). The ratio $J^*_{\text{dif}}/J_{\text{dif}}$ is shown in Figure 2.5a as function of dimensionless time $\tilde{t}$, for several values of V_1. The discrepancy between J^*_{dif} and J_{dif} is confined to early times $\tilde{t}$; it becomes smaller but more persistent as the active material's volume fraction decreases.

Another measure of discrepancy is the relative error in Li-ion accumulation,

$$\mathcal{E}_{\text{tot}} = \left| \frac{\int_0^{t_{\max}} J_{\text{dif}}\,\mathrm{d}t - \int_0^{t_{\max}} J^*_{\text{dif}}\,\mathrm{d}t}{\int_0^{t_{\max}} J_{\text{dif}}\,\mathrm{d}t} \right|,$$

where $t_{\max}$ is the total discharge (charge) time, i.e., the time to achieve the maximum Li-ion concentrations $c_{1,\max}$ and $c^*_{\max}$ in both the active particle and its equivalent counterpart. Figure 2.5b displays $\mathcal{E}_{\text{tot}}$ as function of C rate, for the active material LiNi$_{0.6}$Mn$_{0.2}$Co$_{0.2}$O$_2$ (NMC622) whose properties are [51] $D_1 = 4.3032 \cdot 10^{-14}$ m^2/s, $c_{1,\max} = 50451$ mol/m^3, $D_2 = 7.66 \cdot 10^{-16}$ m^2/s and $r_2 = 5$ μm. For these parameter values and for $V_1 = 0.8$, 0.85 and 0.9, 1C rate corresponds to the current density
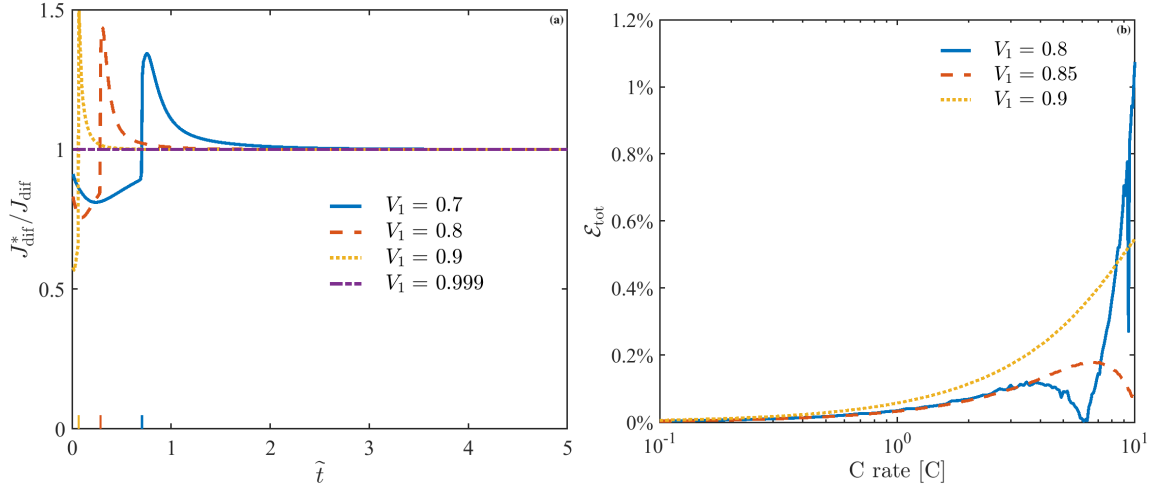
Figure 2.5: **(a)** Temporal evolution of the ratio between the Li-ion fluxes through the surface, $r = r_2$, of the composite sphere and its homogenized counterpart with D^* in Eq. (2.50), $J_{\text{dif}}^*/J_{\text{dif}}$, for several volume fractions V_1 and $D_2/D_1 = 0.0178$. The elevated tick marks indicate the dimensionless intercalation delay time $\tilde{\tau} = (r_2 - r_1)^2 D_1/(D_2 r_2^2) = 0.706$, 0.289 and 0.067 for $V_1 = 0.7$, 0.8 and 0.9, respectively. **(b)** The relative error in the prediction of Li-ion accumulation, $\mathcal{E}_{\text{tot}}$, obtained via our homogenized solution. The error is plotted as function of C rate, for the active material LiNi$_{0.6}$Mn$_{0.2}$Co$_{0.2}$O$_2$ (NMC622) with parameters [51] $D_1 = 4.3032 \cdot 10^{-14}$ m^2/s, $c_{1,\text{max}} = 50451$ mol/m^3, $D_2 = 7.66 \cdot 10^{-16}$ m^2/s and $r_2 = 5$ μm; and several values of the volume fraction V_1.

$J = 1.8728$ A/m^2, 1.9458 A/m^2 and 2.0298 A/m^2, respectively. (These values of J are obtained from Eq. (2.46) with $t = 1$ h and $c_1 = c_{1,\text{max}}$.) The corresponding delay times are $\tau = 0.0466 t_{\text{max}}$, $0.0252 t_{\text{max}}$, and $0.0108 t_{\text{max}}$; in words, the delay time τ is orders of magnitude smaller than the charging/discharging time t_{max}. This result demonstrates the adequacy of our asymptotic (for large t) expression in Eqs. (2.50)–(2.54), since the early time transient stage is negligible in the total charging/discharging process. For C rates varying from 0.1C to 10C, the relative error in Li ion accumulation is below 1%, which shows that the constant value of D^* in Eq. (2.50) is valid for a wide range of C rates.

The remaining equivalent parameters, $\tilde{k}^*(\tilde{t}) = k^*(\tilde{t})/k_1$ and $\tilde{c}_{\text{max}}^*(\tilde{t}) = c_{\text{max}}^*(\tilde{t})/c_{1,\text{max}}$, computed numerically with Eq. (2.44) are displayed in Figure 2.6 for several volume fractions V_1. At early times, $\tilde{t} < \tilde{\tau}$, Li ions diffuse from the electrolyte into the inactive
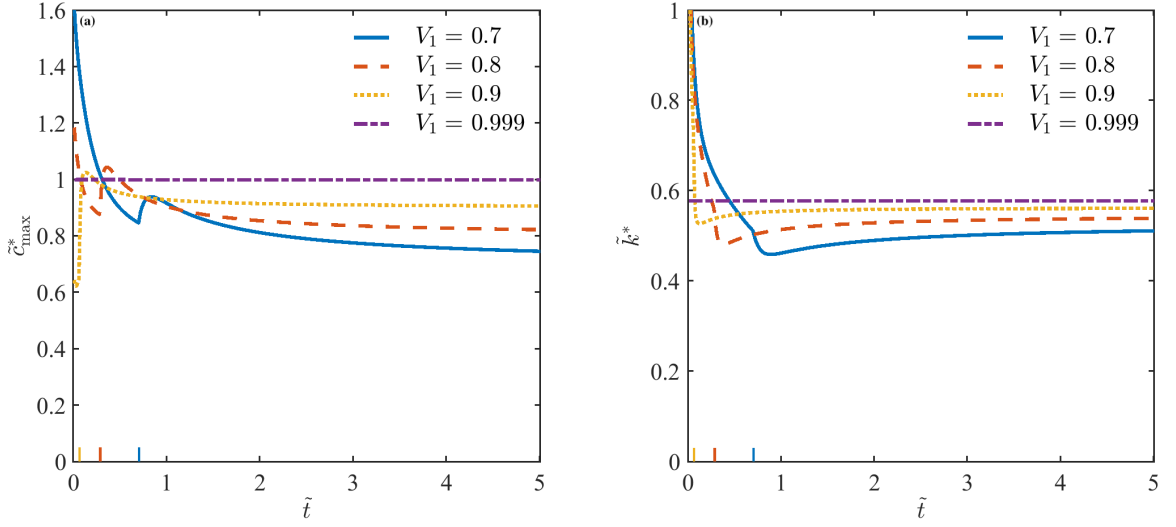
Figure 2.6: Temporal evolution of **(a)** maximum Li concentration $\tilde{c}^*_{\max}(\tilde{t}) = c^*_{\max}(\tilde{t})/c_{1,\max}$ and **(b)** reaction rate constant $\tilde{k}^*(\tilde{t}) = k^*(\tilde{t})/k_1$, for several volume fractions of the active material, V_1. The ratio between the diffusion coefficients of the inactive and inactive materials is set to [32] $D_2/D_1 = 0.0178$. The elevated tick marks indicate the dimensionless intercalation delay time $\tilde{\tau} = (r_2 - r_1)^2 D_1/(D_2 r_2^2) = 0.706$, 0.289 and 0.067 for $V_1 = 0.7$, 0.8 and 0.9, respectively.

material, causing their concentration $\tilde{c}_2(r,\tilde{t})$ to increase at both $r = r_1$ and $r = r_2$, while the Li concentration in the active particle remains unchanged, $\tilde{c}_1(r,\tilde{t}) = 0$. Starting at the delay time $\tilde{t} = \tilde{\tau}$, Li ion intercalate into the active material, increasing $\tilde{c}_1(r_1,\tilde{t})$ linearly with time, while $\tilde{c}_2(r_1,\tilde{t})$ decreases and $\tilde{c}_2(r_2,\tilde{t})$ increases slowly until reaching their steady-state values. This two-stage behavior translates into the concomitant behavior of $\tilde{k}^*(\tilde{t})$ and $\tilde{c}^*_{\max}(\tilde{t})$ (Fig. 2.6). The time it takes these two parameters to reach their asymptotes decreases with V_1. For $V_1 = 0.99$, the volume fraction of the CBD phase is so small that $c^*_{\max} \approx c_{1,\max}$, as expected; at the same time, $k^* \neq k_1$ because the intercalation surface $r = r_1$, which separates the active material and CBD in the composite sphere, is shifted to $r = r_2$ and becomes an interface between the equivalent homogeneous particle and the electrolyte.

The choice of a CBD material, as quantified by the value of its diffusion coefficient D_2, affects the intercalation delay time $\tilde{\tau}$, e.g., for $V_1 = 0.8$, $\tilde{\tau} = 0.289$, 0.029 and 0.003 if $D_2/D_1 = 0.0178$, 0.178 and 1.78, respectively. Thus, the time it takes both
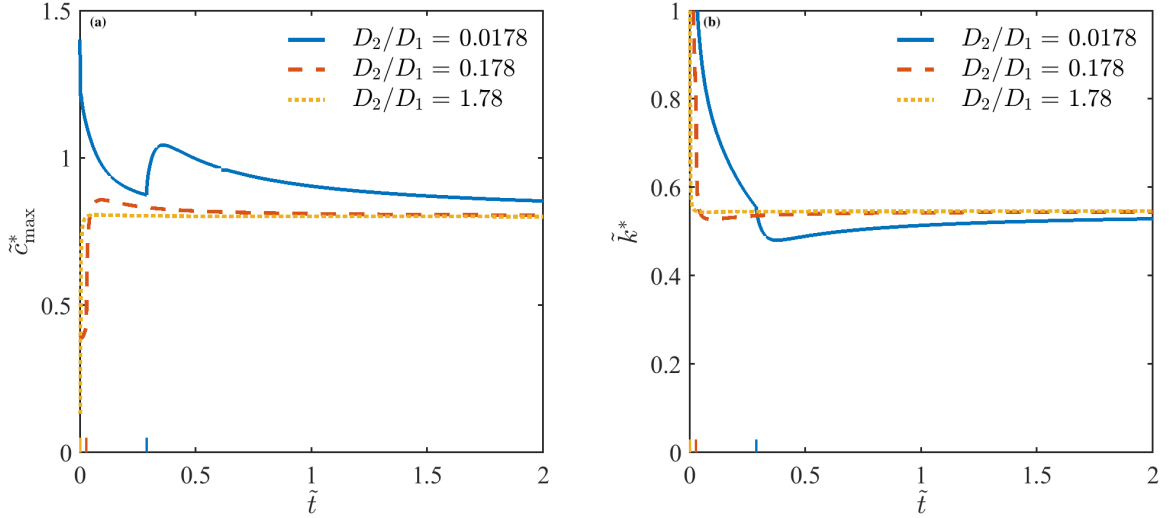
Figure 2.7: Temporal evolution of **(a)** maximum Li concentration $\tilde{c}^*_{\max}(\tilde{t}) = c^*_{\max}(\tilde{t})/c_{1,\max}$ and **(b)** reaction rate constant $\tilde{k}^*(\tilde{t}) = k^*(\tilde{t})/k_1$, for several values of D_2/D_1. Volume fraction of the active material is set to $V_1 = 0.8$. The elevated tick marks indicate the dimensionless intercalation delay time $\tilde{\tau} = (r_2 - r_1)^2 D_1/(D_2 r_2^2) = 0.289$, 0.029 and 0.003 for $D_2/D_1 = 0.0178$, 0.178 and 1.78, respectively.

$c^*_{\max}(t)$ and $k^*(t)$ to reach their steady state decreases with D_2 (Fig. 2.7). At the same time, the steady-state values of these equivalent parameters are independent of D_2. Instead, in accordance with Eqs. (2.53) and (2.54), the steady-state limit of $c^*_{\max}$ varies linearly with V_1 and that of k^* as the power of V_1.

2.6 Summary

Our study provides a quantitative assessment of the impact of CBD on the overall ionic transport in a composite electrode. The latter was represented by a spherical particle whose active-material core is coated with CBD. This composite sphere is replaced with its homogeneous counterpart, for which we derived equivalent electrical conductivity, ionic diffusivity, and reaction parameters in the Butler-Volmer equation. These equivalent characteristics are defined to ensure that the same mass and charge enter the composite and homogenized spheres. They are expressed in terms of the

volume fraction of the active material and transport properties of the active material and CBD. In general, the equivalent effective diffusion coefficient and reaction parameters are time-dependent and exhibit two-stage behavior characterized by the reaction delay time; their determination requires numerical evaluation of the inverse Laplace transforms. At later times, these characteristics are time-independent and given explicitly by closed-form formulae. Our analysis leads to the following major conclusions.

- Our model can be used to quantitatively assess the effects of CBD on ion transport. For example, for a composite electrode with CBD's volume fraction of 0.2 and the ratio between the diffusion coefficients of CBD and the active material of 0.0178, ignoring the presence of CBD would overestimate the composite's diffusion coefficient by 163%.

- Our closed-form expressions for the equivalent diffusion coefficient and reaction parameters yield accurate approximations of the key quantities of interest. For example, when used to model of an NMC622 active particle coated with CBD, they yield predictions of the Li-ion accumulation whose relative error is about 1%, for C rates ranging from 0.1C to 10C.

- The simplicity of these expressions facilitates their use in single- and multi-particle representations of Li-ion and Li-metal batteries. This enables one to use these cell-level models, while accounting for the presence of CBD and the physicochemical characteristics of composite electrodes. This, in turn, facilitates the electrode design without resolving the complicated microstructure at high computational cost.

In follow-up studies, we will conduct experimental validation of our model for various active materials, incorporate it into cell-level simulations, and assess its accuracy in predicting cell voltage during discharge. Future extensions of our model will incorporate the volume expansion of active particles and the transport properties of gradient Li-rich oxide cathodes mixed with CBD.

Chapter 3

Impact of carbon binder domain on the performance of lithium-metal batteries

3.1 Abstract

Pseudo-2-dimensional models are routinely used to predict the lithiation curves for energy storage devices, including lithium-metal batteries. The performance of such models is as good as their parameterization, which remains a challenge especially in the presence of carbon binder domain (CBD). We propose two alternative parameterization strategies, which explicitly account for the CBD volume fraction and physical properties. The first aggregates CBD with the electrolyte-filled pore space and expresses the Bruggeman exponent in terms of a solution of microstructure-specific closure problem. The second treats CBD and active particles as a composite solid phase, whose effective properties are computed (semi-)analytically via homogenization. We show that the latter strategy used to parameterize the Doyle-Fuller-Newman model provides an attractive middle ground between the model complexity and the prediction accuracy. Our modeling results suggest that the battery discharge time decreases as either the CBD volume fraction increases or the CBD ionic diffusivity decreases, and is insensitive to the CBD ionic conductivity. The quantitative nature

of these observations can be used in the optimal design of porous cathodes.

3.2 Introduction

Porous materials play a central role in energy storage devices such as lithium-based batteries. For example, the cathodes of both Li-ion and Li-metal batteries are typically composed of active porous materials (transition-metal oxide particles) [52], the anode of a Li-ion battery is made of porous graphite [53], and a porous separator is placed between the two electrodes. Pore-scale material properties, e.g., the size and spatial arrangement of (transition-metal oxide) active material particles in an electrode [54] or the columnized structure of a separator [17], can be used to optimize the performance of a device. That is because such pore-scale characteristics control device-scale transport of lithium ions, Li^+, and, ultimately, battery performance and aging.

Among other relevant pore-scale quantities, the so-called carbon binder domain (CBD) [55, 22] is ubiquitous yet least studied. CBD refers to the mixed phase comprising carbon additives (e.g., carbon black) and a binder, which surrounds active particles. It is routinely used to improve the electric conductivity and mechanical stability of porous electrodes [56, 22]. Despite its benefits, CBD hinders the intercalation of Li^+ from the electrolyte to the active particles by increasing the tortuosity of diffusion pathways and reducing the active surface area, thus leading to performance reduction, especially at high current [26, 27, 57]. Pore-scale heterogeneity of CBD distribution also impacts a device's overall performance [58].

Complexity of the fabrication process and challenges in tomographic imagining of composite materials prevent the accurate characterization of the microstructure of porous electrodes, undermining the ability to distinguish between different solid phases and between the solid phase and the pore space. In particular, it is often difficult to distinguish between the pore space and CBD, which is virtually invisible in tomographic scans [32]. Yet, this information is needed for pore-scale numerical simulations of Li-metal batteries. That is why, despite advances in imaging techniques [59],

pore-scale electrochemical simulations often rely on synthetically-enhanced realizations of the porous structure, which supplement the topology of the active material from imaging with synthetic CBD configurations [60, 61, 51, 32]. The latter process relies on morphological hypotheses about CBD distribution, e.g., assuming that active particles are covered with a uniform CBD coat or prescribing irregular CBD structures to reflect the possible tendency of CBD deposition to adhere to itself rather than to an active material surface [62, 32].

Continuum-scale simulations of physicochemical processes in porous media both obviate the need for this elusive information and significantly accelerate the computation by averaging out the pore-scale variability and replacing various phases of an electrolyte-filled porous material with a single continuum characterized by aggregate properties such as porosity and tortuosity. [40, 63] The pseudo-two-dimensional (P2D) models [37, 64] occupy the middle ground between these pore- and continuum-scale simulation frameworks in that they retain a micro-scale description of transport in the active solid-phase but represent the latter as an effective/equivalent sphere or a collection of spheres. Like all effective/continuum-scale models, the P2D models and their various simplifications [65] trade the high-fidelity of pore-scale simulations for computational efficiency.

Current implementations of the P2D models lump the CBD phase with the electrolyte-filled pore space and rely on empirical corrections of the tortuosity coefficient to account for the presence of CBD [31, 59]. In this setting, automated techniques [66] can be used to estimate tortuosity from tomographic data; and its CBD-related corrections can be constructed to account for, e.g., the overall porosity, the physics of CBD deposition during fabrication, and the active particles' geometry [31]. This procedure relies on pore-scale simulations of solute transport in a representative elementary volume of the imaged porous material and, crucially, ignores transport properties (e.g., ionic diffusion coefficient and ionic conductivity) of the CBD phase.

To explicitly account for the physicochemical characteristics of the CBD phase, we propose a parameterization of the P2D models that treats the two solid phases (active material and CBD) as a single homogenized solid phase. That is in contrast to the current approaches [31, 59] that aggregate the solid (CBD) and fluid (electrolyte)

phases into an equivalent liquid phase. Our parameterization utilizes the homogenization results [15] for a CBD/active-material spherical composite, which are based on mass and charge conservation in the presence of ion intercalation into an active particle coated by CBD. The equivalent properties of this solid composite are expressed in terms of the CBD volume fraction and transport properties of the active material and CBD. Our parameterization strategy offers three practical benefits. First, by relying on the readily available volume fraction rather than pore-scale topology, it does not confront the above-mentioned limitations of electrode imaging; the latter serve as raison d'être for the less intuitive parameterization strategies currently in use. Second, our approach is significantly more computationally efficient than its alternatives [31, 59], because it yields a (semi-)analytical parameterization without resorting to pore-scale simulations that underpin the latter. Third, the dependence of our results on the CBD volume fraction and properties of CBD and active material facilitates the optimal design of battery electrodes.

We compare the performance of the two alternative parameterizations of widely used P2D models—the Doyle-Fuller-Newman (DFN) model [37] and the multi-particle DFN (mDFN) model [64]—and of their simplified version encapsulated in the single-particle model [34] (SPM). In this comparison, the predictions of lithiation curves derived from the pore-scale simulations of a porous cathode with given CBD morphology [32] serve as "ground truth".[1] Our numerical experiments reveal the superior performance of the DFN model with our parameterization. This model's sensitivity to variations in CBD properties and ease of use make it a viable tool for prediction and design.

---

[1]The failure of P2D models to predict experimental lithiation curves at high C-rates has at least two sources: the errors in material characterization and the questionable validity of multiple approximations that underpin the upscaling (homogenization) of the underlying pore-scale models. We focus on the latter source of prediction error by treating the pore-scale simulations as exact, even when their predictions of lithiation curves differ from observations [32] due to errors in material characterization and representation.

3.3   Continuum-scale models

P2D models of a Li-metal battery describe the spatial variability of Li^+ concentration and electric potential in the through-cell (x) direction, neglecting their variability in the transverse direction. Let us place the inner surface of a Li-metal anode at $x = 0$, so that a separator of length L_{sep} occupies the interval $0 < x < L_{sep}$ and a porous cathode of length L_{cat} lies in the interval $L_{sep} \leq x \leq L$, where $L = L_{cat} + L_{sep}$. Then the device-scale spatiotemporal evolution of the Li^+ concentration, $c^e(x,t)$, and electric potential, $\varphi^e(x,t)$, in the electrolyte satisfy the one-dimensional partial-differential equations (PDEs)

$$\frac{\partial \omega c^e}{\partial t} = \frac{\partial}{\partial x}\left(D^e_{\text{eff}}\frac{\partial c^e}{\partial x}\right) + A_{rs}\frac{1-t^+}{F}j, \qquad 0 < x < L, \quad t > 0 \qquad (3.1a)$$

and

$$\frac{\partial}{\partial x}\left(K^e_{\text{eff}}\frac{\partial \varphi^e}{\partial x} + \kappa^s_{\text{eff}}\frac{\partial \ln c^e}{\partial x}\right) + A_{rs}j = 0, \qquad 0 < x < L, \quad t > 0. \qquad (3.1b)$$

Here, $\omega(x)$ is the porosity of the separator and cathode; D^e_{eff} and K^e_{eff} are, respectively, the effective ionic diffusion coefficient and effective ionic conductivity in the electrolyte in the presence of the porous material; $A_{rs}(x)$ is the specific reactive surface of the cathode, i.e., $A_{rs} = 0$ for $0 < x < L_{sep}$; $j(x,t)$ is the current density, with $j = 0$ for $0 < x < L_{sep}$; and the lumped parameter $\kappa^s_{\text{eff}} = 2RTK^e_{\text{eff}}(t^+ - 1)\lambda/F$ is expressed in terms of the effective ionic conductivity K^e_{eff}, the temperature T, the cation transference number t^+ (a given function of c^e), the activity coefficient λ, and the gas (R) and Faraday (F) constants.

The P2D models also track the spatiotemporal evolution of Li^+ concentration, c^s, and electric potential, φ^s, within the solid phase (active material) of the porous electrode. In so doing, the solid phase with complex microstructure is replaced by a collection of non-overlapping spheres of either identical radius R^s or various radii.[2]

---

[2]The former approach, the DFN model, implicitly assumes the cathode microstructure to be uniform; the latter, the mDFN model [64], aims to capture heterogeneity of the cathode's microstructure.

In the former case, i.e., in the DFN model, the specific reactive surface A_{rs} acquires a simple expression $A_{\mathrm{rs}} = 3(1-\omega)/R^{\mathrm{s}}$; and the Li^+ concentration, $c^{\mathrm{s}}(r,t;x)$, and electric potential, $\varphi^{\mathrm{s}}(r,t;x)$, vary in the radial ($r$) direction within the sphere according to

$$\frac{\partial c^{\mathrm{s}}}{\partial t} = \frac{1}{r^2}\frac{\partial}{\partial r}\left(D^{\mathrm{s}}r^2\frac{\partial c^{\mathrm{s}}}{\partial r}\right), \qquad 0 < r < R^{\mathrm{s}}, \quad t > 0, \tag{3.1c}$$

and

$$\sigma_{\mathrm{eff}}^{\mathrm{s}}\frac{\partial^2\varphi^{\mathrm{s}}}{\partial x^2} = A_{\mathrm{rs}}j, \qquad L_{\mathrm{sep}} < x < L, \quad t > 0, \tag{3.1d}$$

where D^{s} is the diffusion coefficient for Li^+ in the solid phase and $\sigma_{\mathrm{eff}}^{\mathrm{s}}$ is the effective conductivity of the solid phase in the porous cathode.

Processes in the electrolyte phase (Eqs. 3.1a and 3.1b) and the solid phase (Eqs. 3.1c and 3.1d) are coupled due to ion intercalation at the solid/liquid interface. In the DFN model, this interface is the surface of each solid sphere, $r = R^{\mathrm{s}}$. Specifically, under certain conditions, the Butler-Volmer equation,

$$j = 2Fk_0\sqrt{c^{\mathrm{e}}(x,t)c^{\mathrm{s}}(R^{\mathrm{s}},t;x)}\sqrt{c_{\mathrm{max}}^{\mathrm{s}} - c^{\mathrm{s}}(R^{\mathrm{s}},t;x)}\sinh\left(\frac{F\eta}{2RT}\right), \qquad L_{\mathrm{sep}} \leq x \leq L,$$

$$\tag{3.1e}$$

relates the current density $j(x,t)$ in Eqs. 3.1a–3.1d to the Li^+ concentrations and electric potentials both in the electrolyte, $c^{\mathrm{e}}(x,t)$ and $\varphi^{\mathrm{e}}(x,t)$, and on the active material's surface, $c^{\mathrm{s}}(R^{\mathrm{s}},t;x)$ and $\varphi^{\mathrm{s}}(R^{\mathrm{s}},t;x)$. In this relation, k_0 is the reaction rate constant; $c_{\mathrm{max}}^{\mathrm{s}}$ is the maximum concentration in the solid phase; $\eta(x,t) = \varphi^{\mathrm{s}}(R^{\mathrm{s}},t;x) - \varphi^{\mathrm{e}}(x,t) - U_{\mathrm{ocp}}$ is the cell overpotential; and the open circuit potential U_{ocp} is a given function of $c^{\mathrm{s}}(R^{\mathrm{s}},t;x)/c_{\mathrm{max}}^{\mathrm{s}}$. In the mDFN model, $j(x,t)$ is averaged over the particle size distribution.

SPM represents a reduced-complexity counterpart of the DFN model, which neglects mass transport in the electrolyte. Instead of solving Eq. 3.1a, SPM assumes the Li^+ concentration in the electrolyte, c^{e}, to be uniform.

Eqs. 3.1 are subject to initial and boundary conditions, which reflect a battery's

operating regime. To be concrete, we consider a battery with spatially uniform Li$^+$ concentrations in the electrolyte and the solid phase, $c_{\mathrm{in}}^{\mathrm{e}}$ and $c_{\mathrm{in}}^{\mathrm{s}}$, which gives rise to the initial conditions

$$c^{\mathrm{e}}(x,0) = c_{\mathrm{in}}^{\mathrm{e}}, \quad 0 < x < L; \qquad c^{\mathrm{s}}(r,0) = c_{\mathrm{in}}^{\mathrm{s}}, \quad 0 < r < R^{\mathrm{s}}. \tag{3.2a}$$

To simulate a battery discharging with the constant discharge current density i_{dis}, we impose the boundary conditions

$$-D_{\mathrm{eff}}^{\mathrm{e}}\frac{\partial c^{\mathrm{e}}}{\partial x}(0,t) = \frac{1-t_+}{F}i_{\mathrm{dis}}, \qquad \frac{\partial c^{\mathrm{e}}}{\partial x}(L,t) = 0, \qquad t > 0; \tag{3.2b}$$

$$-K_{\mathrm{eff}}^{\mathrm{e}}\frac{\partial \varphi^{\mathrm{e}}}{\partial x}(0,t) - \kappa_{\mathrm{eff}}^{\mathrm{e}}\frac{\partial \ln c^{\mathrm{e}}}{\partial x}(0,t) = i_{\mathrm{dis}}, \qquad t > 0; \tag{3.2c}$$

$$K_{\mathrm{eff}}^{\mathrm{e}}\frac{\partial \varphi^{\mathrm{e}}}{\partial x}(L,t) + \kappa_{\mathrm{eff}}^{\mathrm{e}}\frac{\partial \ln c^{\mathrm{e}}}{\partial x}(L,t) = 0, \qquad t > 0; \tag{3.2d}$$

$$\frac{\partial \varphi^{\mathrm{s}}}{\partial x}(L_{\mathrm{sep}},t) = 0, \qquad -\sigma_{\mathrm{eff}}^{\mathrm{s}}\frac{\partial \varphi^{\mathrm{s}}}{\partial x}(L,t) = i_{\mathrm{dis}}, \qquad t > 0. \tag{3.2e}$$

This formulation automatically satisfies the continuity conditions at the separator/electrode interface, $x = L_{\mathrm{sep}}$. Finally, the boundary conditions for the solid particles are

$$\frac{\partial c^{\mathrm{s}}}{\partial r}(0,t;x) = 0, \qquad -D^{\mathrm{s}}\frac{\partial c^{\mathrm{s}}}{\partial r}(R^{\mathrm{s}},t;x) = \frac{j(x,t)}{F}, \qquad t > 0, \qquad L_{\mathrm{sep}} \leq x \leq L. \tag{3.2f}$$

3.3.1 Alternative parameterizations of P2D models

The effective parameters $D_{\mathrm{eff}}^{\mathrm{e}}$, $K_{\mathrm{eff}}^{\mathrm{e}}$, and $\sigma_{\mathrm{eff}}^{\mathrm{s}}$ in the P2D models can be related to their counterparts in the corresponding free phase (the diffusion coefficients of Li$^+$ in a given electrolyte, D^{e}; and the ionic conductivities of the electrolyte and the solid phase, K^{e} and σ^{s}) and the microstructure of the porous material via homogenization [2, 40]. In lieu of such procedures, which can be computationally demanding, it is common to deploy the Bruggeman relations, [2, 31, 40]

$$D_{\mathrm{eff}}^{\mathrm{e}} = \omega^{b^{\mathrm{e}}} D^{\mathrm{e}}, \qquad K_{\mathrm{eff}}^{\mathrm{e}} = \omega^{b^{\mathrm{e}}} K^{\mathrm{e}}, \qquad \sigma_{\mathrm{eff}}^{\mathrm{s}} = (1-\omega)^{b^{\mathrm{s}}} \sigma^{\mathrm{s}}, \tag{3.3}$$

where b^{e} and b^{s} are the Bruggeman exponents, which are often set to 1.5.[3]

We consider two alternative strategies for incorporation of CBD into this parameterization of the P2D models. The currently used approach is to lump together the electrolyte and CBD phases [31, 59]; consequently, we refer to it as the augmented electrolyte (AE) parameterization. Our approach is to aggregate the two solid phases, the active material and CBD, instead; we refer to it as the augmented material (AM) parameterization. Our implementation of both strategies is detailed below.

AE parameterization. Combining the CBD phase with the electrolyte-filled pores modifies the actual porosity of the cathode, ω. If the volume fraction of the active material in the solid phase is v, then the resulting "lumped" porosity is $\varepsilon = \omega + (1 - \omega)(1 - v)$ and the volume fraction of the active material (the only remaining solid phase) is $1 - \varepsilon$. The simplest version of the AE parameterization of the P2D models modifies the Bruggeman Eqs. 3.3 by replacing ω with ε, leaving the remaining properties unchanged. This procedure ignores the physicochemical characteristics of CBD, but can be enhanced to account for some of this information. [31, 59]

We also test a more elaborate way to compute the Bruggeman exponent b^{e} in Eq. 3.3, which relies on pore-scale simulations of transport of a chemically inert solute in a representative elementary volume (REV) of the porous cathode. [66] The REV Ω_{REV} of a three-dimensional porous material is a cube of length L_{REV} that is composed of the fluid phase (the electrolyte-filled pores) Ω_{e} and the solid phase Ω_{s}, i.e., $\Omega_{\mathrm{REV}} = \Omega_{\mathrm{e}} \cup \Omega_{\mathrm{s}}$. In the AM parameterization, the "pore space" $\Omega = \Omega_{\mathrm{e}} \cup \Omega_{\mathrm{CBD}}$ comprises the electrolyte phase Ω_{e} and CBD Ω_{CBD}, while the solid phase is reduced to the active material domain Ω_{am}, such that $\Omega_{\mathrm{REV}} = \Omega \cup \Omega_{\mathrm{am}}$. The spatial distribution of the solute concentration, $c(\mathbf{y})$, within the pore space Ω is described by the three-dimensional PDE

$$\nabla \cdot (D(\mathbf{y})\nabla c) = 0, \qquad \mathbf{y} \in \Omega, \tag{3.4a}$$

---

[3]We choose the Bruggeman relations because of their widespread use in battery simulations, even though more accurate and robust representations are available [40, 63]. This choice is sufficient to demonstrate how our approach allows one to incorporate CBD into existing models, which might or might not rely on the Bruggeman relations.

that is subject to the boundary conditions along the surface $\partial\Omega$ bounding the pore space Ω,

$$c(\mathbf{y} \in \partial\Omega_\mathrm{L}) = c_\mathrm{L}; \qquad c(\mathbf{y} \in \partial\Omega_\mathrm{R}) = c_\mathrm{R}; \qquad \nabla c \cdot \mathbf{n} = 0, \quad \mathbf{y} \in \partial\Omega/(\partial\Omega_\mathrm{L} \cup \partial\Omega_\mathrm{R}).$$

$$(3.4\mathrm{b})$$

The mass flux, $-D\nabla c$, is driven by the difference between the concentrations c_L and c_R imposed at the two opposite (Left and Right) faces of the REV, $\partial\Omega_\mathrm{L}$ and $\partial\Omega_\mathrm{R}$, whereas no-flux boundary conditions are assigned to all other boundaries, identified by the outward unit vector $\mathbf{n}$. The tortuosity factor and, hence, the corresponding Bruggeman exponent b^e are computed by equating the overall flux crossing the REV and the equivalent homogeneous cube.
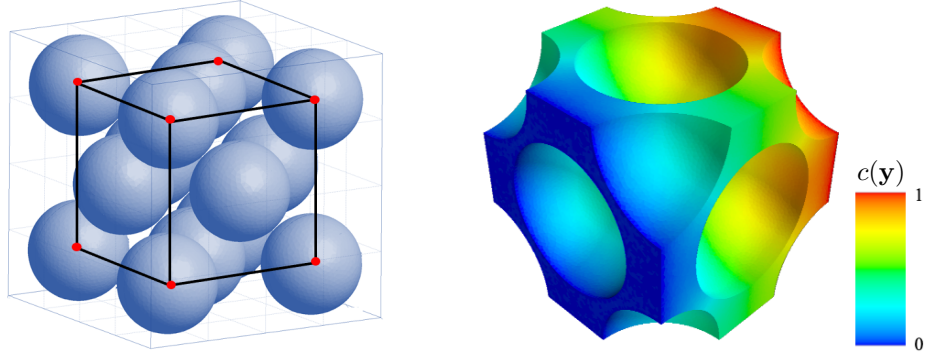
Figure 3.1: Face-Centered-Cubic arrangement of the active-material particles (Left) and a representative solution, $c(\mathbf{y})$, to the closure problem in Eq. 3.4 (Right), which is used to calculate the Bruggeman exponent b^e. This solution corresponds to $c_\mathrm{L} = 0$ and $c_\mathrm{R} = 1$.

While one could use tomographic images to estimate $\partial\Omega$ [31, 61], for our purpose it is sufficient to consider a porous cathode consisting of identical spheres arranged into a Face-Centered-Cubic lattice (Figure 3.1); the radius of these spheres is selected to achieve the prescribed porosity ε. Unlike the previous studies of this kind, we explicitly account for the diffusive coefficient of CBD, D^CBD, by letting the diffusion

coefficient $D(\mathbf{y})$ to vary in space:

$$D(\mathbf{y}) = \begin{cases} D^{\mathrm{e}} & \mathbf{y} \in \Omega_{\mathrm{e}} \\ D^{\mathrm{CBD}} & \mathbf{y} \in \Omega_{\mathrm{CBD}}. \end{cases}$$

The closure problem in Eq. 3.4 is solved once, at the beginning of the simulations, to compute the Bruggeman exponent b^{e}. A representative solution of the closure problem is shown in Figure 3.1.

AM parameterization. This new strategy leaves the electrolyte-filled pore space, Ω_{e}, untouched, while accounting for the composite nature of the solid phase, $\Omega_{\mathrm{s}} = \Omega_{\mathrm{am}} \cup \Omega_{\mathrm{CBD}}$. A porous cathode is assumed to consist of active spherical particles of radius R_{am}, which are coated with a CBD layer of thickness d_{CBD}, such that the volume fraction of active material in the solid phase is $v = R_{\mathrm{am}}^2/(R_{\mathrm{am}} + d_{\mathrm{CBD}})^2$. The effective (homogenized) physicochemical properties of the solid particle of radius $\tilde{R}^{\mathrm{s}} = R_{\mathrm{am}} + d_{\mathrm{CBD}}$ are [15]

$$\tilde{D}^{\mathrm{s}} = \left[\frac{v^{2/3}}{D^{\mathrm{s}}} + 5\frac{1-v}{D^{\mathrm{CBD}}} \left(\frac{(1-v^{1/3})^2 + 3(v^{1/3}+2)(1-v^{1/3})}{2(1-v^{1/3})^2 + 6v^{1/3}} - \frac{3(1-v^{1/3})^2}{1-v} \right) \right]^{-1}, \quad (3.5a)$$

$$\tilde{\sigma}^{\mathrm{s}} = \frac{2\sigma^{\mathrm{s}}\sigma^{\mathrm{CBD}}}{\dfrac{\sigma^{\mathrm{s}}(v^{-1/3}-1)}{1-v^{1/3}(v^{1/3}+1)^2} + 2\sigma^{\mathrm{CBD}}v^{-1/3}}, \qquad \tilde{k}_0 = k_0 v^{6/7}\sqrt{\frac{1+2v^{1/3}}{7+2v^{1/3}}}, \qquad \tilde{c}_{\mathrm{max}}^{\mathrm{s}} = c_{\mathrm{max}}^{\mathrm{s}} v,$$

$$(3.5b)$$

$$\tilde{c}_{\mathrm{in}}^{\mathrm{s}} = c_{\mathrm{in}}^{\mathrm{s}} v + c_{\mathrm{in}}^{e}(1-v). \qquad (3.5c)$$

These expressions are derived by ensuring that the mass and charge entering the composite particle are the same as those entering the homogenized particle. They are strictly valid for operating conditions under which the intercalation delay time $t_{\mathrm{del}} = d_{\mathrm{CBD}}^2/D^{\mathrm{CBD}}$ is negligible. Otherwise, the constant homogenized parameters in Eq. 3.5 should be replaced with their time-dependent counterparts; [15] we refer to the approach that replaces the constant $\tilde{D}^{\mathrm{s}}$ with $\tilde{D}^{\mathrm{s}}(t)$ as the AM+ parameterization.

The AM parameterization of the P2D models, Eqs. 3.1–3.3, consists of replacing D^{s}, $\sigma_{\mathrm{eff}}^{\mathrm{s}}$, k_0, and $c_{\mathrm{max}}^{\mathrm{s}}$ with their tilde-marked counterparts from Eq. 3.5.

3.4   Numerical experiments

We conduct a series of numerical experiments to investigate the ability of the three P2D models (DFN, mDFN, and SPM) with the two alternative (AE and AM) parameterizations to accurately predict the lithiation curves for LMBs. These curves describe the temporal evolution of cell terminal voltage $U_{\text{cell}} = \phi_{\text{s}}(L, t) - \phi_{\text{s}}(0, t)$, where the reference potential $\phi_{\text{s}}(0, t)$ is set to 0 and the solid-phase potential $\phi_{\text{s}}(x, t)$ for any $x > 0$, including $x = L$, is computed by solving Eqs.3.1–3.3.

Although our approach is general and applicable to any Li-ion or Li-metal battery, we demonstrate it on a LMB with nickel manganese cobalt oxides cathode (NMC622), carbon additives and polyvinylidene fluoride binder, and $LiPF_6$ electrolyte [32]. The electrochemical properties of this reference LMB [51, 32] are summarized in Table 3.1. For these parameters, all three P2D models, i.e., Eqs. 3.1–3.3, are solved using the open source software package Python Battery Mathematical Modelling (PyBaMM) [67]; the software routines were modified to accommodate time- and radius-dependent parameters; each subdomain (separator, porous electrode and particle) is discretized with 40 elements. In the mDFN model, the active particles are assigned a lognormal distribution with the mean and standard deviation from Ref. 32.

The three P2D models (DFN, mDFN, and SPM) with the two alternative (AE and AM) parameterizations yield six alternative methods for computing the lithiation curves; they are labeled Methods 1 through 6 in Table 3.2. The AE parameterization can either use the standard/unmodified value of the Bruggeman exponent $b^{\text{e}} = 1.5$ or to estimate this value by solving the closure problem, Eq. 3.4; the latter approach yields $b^{\text{e}} = 2.67$, as reported in Table 3.3 and referred to below as the AE+ parameterization. This closure problem is solved with the open source software package Fipy [68] on the REV in Figure 3.1. The radius of the spherical particles forming the REV is selected to match the experimentally measured porosity ω, and the pore space Ω is discretized into 349522 elements using the open source software package GMSH [69].

The AM parameterization uses the volume fraction of active material in the solid phase, v, and the transport properties of its two components (active material and CBD) as inputs to calculate the effective properties of the single homogenized solid

Table 3.1: Geometrical and electrochemical parameters used both in our analysis and to construct the reference lithiation curves [51, 32]. The functional dependencies are given in Section 4 of Ref. 51.

Porous electrode		
Initial Li concentration [mol/m^3]	c_{in}^s	18409.57
Maximum Li concentration [mol/m^3]	c_{max}^s	50451
NCM ionic conductivity [S/m]	σ^s	2.8
CBD ionic conductivity [S/m]	σ^{CBD}	0.0169
NCM ionic diffusivity [m^2/s]	D^s	$4.3032 \cdot 10^{-14}$
CBD ionic diffusivity [m^2/s]	D^{CBD}	$7.6597 \cdot 10^{-16}$
Reaction rate constant [m$^{2.5}$/s/mol$^{0.5}$]	k_0	$1.5228 \cdot 10^{-11}$
Open circuit potential [V]	U_{ocp}	function of c^s/c_{max}^s
Cathode thickness [μm]	L_{cat}	59
Active material volume fraction in the REV [$-$]	$1 - \varepsilon$	0.583
CBD volume fraction in the REV [$-$]	$(1 - \omega)(1 - v)$	0.112
Active particle representative radius [μm]	R^s	7.84
Coefficient of variation of R^s [$-$]	σ_r/R^s	0.46

Electrolyte (values at c_{in}^e)		
Initial Li$^+$ concentration [mol/m]	c_{in}^e	1000
Ionic conductivity for Li$^+$ [S/m]	K^e	0.95; function of c^e
Transference number [$-$]	t^+	0.2527; function of c^e
Diffusivity [m^2/s]	D^e	$3.7621 \cdot 10^{-10}$; function of c^e
Activity term [$-$]	λ	1.9865; function of c^e

Separator		
Thickness [μm]	L_{sep}	100
Porosity [$-$]	ω_{sep}	0.5

Cell characteristics & operating conditions		
Nominal cell capacity [mAh]	Q_{nom}	3.6192
Cell area [cm^2]	A	1.131
Applied current density [mA/cm^2]	i_{dis}	$\{1, 3, 6, 12\}$
Temperature [K]	T	298.15
Lower voltage cut-off [V]	V_{low}	3.0
Upper voltage cut-off [V]	V_{up}	4.2

Table 3.2: The three P2D models (DFN, mDFN, and SPM) with the two alternative (AE and AM) parameterizations are denoted by Method 1–Method 6. The enhanced versions of these parameterizations are denoted by the plus sign.

	DFN	mDFN	SPM
AE parameterization	Method 1	Method 3	Method 5
AE+ parameterization	Method 1+	Method 3+	Method 5+
AM parameterization	Method 2	Method 4	Method 6
AM+ parameterization	Method 2+	Method 4+	−

Table 3.3: Modified (effective) values of the physicochemical properties from Table 3.1 resulting from the AE+ and AM parameterizations of the P2D models. The only difference between the AE and AE+ parameterizations is that the former leaves the Bruggeman exponent unchanged, $b^{\mathrm{e}} = 1.5$.

	AE+	AM
Porosity, ω (ε for AE)	0.417	0.305
Solid-phase volume fraction, $1 - \omega$ ($1 - \varepsilon$ for AE)	0.583	0.695
Volume ratio of active particle in solid phase, v	1	0.839
Solid-particle radius, R^{s} ($\tilde{R}^{\mathrm{s}}$) [μm]	7.84	8.31
Solid-phase diffusivity, D^{s} ($\tilde{D}^{\mathrm{s}}$) [m^2/s]	$4.303 \cdot 10^{-14}$	$1.954 \cdot 10^{-14}$
Solid-phase conductivity, σ^{s} ($\tilde{\sigma}^{\mathrm{s}}$) [S/m]	2.8	0.364
Reaction rate, k_0 ($\tilde{k}_0$) [m$^{2.5}$/s/mol$^{0.5}$]	$1.523 \cdot 10^{-11}$	$0.772 \cdot 10^{-11}$
Maximum Li concentration, $c^{\mathrm{s}}_{\mathrm{max}}$ ($\tilde{c}^{\mathrm{s}}_{\mathrm{max}}$) [mol/m^3]	50451	42328
Cathode Bruggeman exponent b^{e}	2.67	1.5
Cathode Bruggeman exponent b^{s}	1.5	1.5

phase (Table 3.3). The value of v is computed for the FCC periodic microstructure of the porous electrode (Figure 3.1). While the representative active material radius R^{s} is kept unchanged, the CBD coating thickness d_{CBD} and, hence, the radius of the homogenized particle, $\tilde{R}^{\mathrm{s}}$, are computed to obtain the measured solid phase volume fraction. The same effective parameters are retained also when considering a distribution of particles in the mDFN model.

For reasons described in the Introduction, the lithiation curves obtained via pore-scale simulations [32] serve as the ground truth that provides a baseline for the assessment of the accuracy of the alternative parameterizations of the P2D models in

Table 3.2. These simulations consist of numerical solution of the three-dimensional mass and charge balance equations for the electrolyte-filled pore space and the ambient active material; an interfacial kinetics model couples these PDEs at the liquid-solid interfaces. The simulations [32] are carried out for a hybrid porous microstructure, in which a tomographically accurate active material geometry is enhanced by a synthetically generated CBD phase with assigned volume fraction. Our P2D simulations and their pore-scale counterparts are carried out for the same porosity, ω, and active-material volume fraction, $1 - \varepsilon$; no fitting parameters are used to improve the match between the P2D and pore-scale predictions of the lithiation curves.[4]

3.5 Results and Discussion

We use a series of numerical experiments to identify a Method, which yields the most accurate approximation of the pore-scale estimate of the lithiation curves for the LMB characterized by the parameter values in Table 3.1. In another set of numerical experiments, we use this Method as a predictive tool to quantify the impact of modifying CBD properties (the volume fraction and composition in Table 3.4) on the overall cell performance.

3.5.1 Method verification

Figure 3.2 compares predictions of the lithiation curves obtained via the DFN model with the alternative parameterizations from Table 3.2, for several values of the discharge current density i_{dis}. Also shown in this figure are the lithiation curves computed via the pore-scale simulations [32], which serve as the ground truth. Figure 3.2 reveals that the standard DFN parameterization (Method 1) fails to account for

---

[4]In lieu of performing pore-scale simulations, we use their output reported in Figure SI-1c from Supporting Information in Ref. 32. This output is in the form of lithiation curves for four discharge scenarios with increasing current density and corresponds to "Microstructure B". The latter consists of CBD-coated active particles and shares the same electrode thickness as the one utilized in our P2D simulations. In Figure SI-1c, the terminal voltage U_{cell} is exhibited as function of transferred charge $\mathcal{C} = i_{\mathrm{dis}}t$ [mAh/cm^2]; to plot U_{cell} as function of time t, we divide transferred charge by the current density i_{dis} corresponding to each C-rate scenario, i.e., $t = \mathcal{C}/i_{\mathrm{dis}}$.

the CBD presence, whose impact increases with i_{dis}, consistently over-predicting the LMB capacity. Both Method 1+ and Method 2 improve the prediction accuracy at all tested discharge currents, with Method 1+ adequately representing the lithiation curves throughout the discharge process. Method 2 accurately captures the final discharge time for all i_{dis}, but over-estimates the voltage drop at early times. That is because the AM parameterization in Eq. 3.5 ignores the pre-asymptotic time-dependence of the effective coefficients, whose persistence increases with discharge current; the time-to-asymptote is directly related to the intercalation delay time t_{del} induced by the CBD phase, which increases with i_{dis} (Figure 3.2). When choosing between Method 1+ and Method 2 it is worthwhile recognizing that Method 1+ requires the solution of a closure problem on a representative microstructure of the porous electrode, while Method 2 utilizes the effective coefficients that can be readily computed from the active material volume fraction in the solid phase v and phase-specific transport properties.

Regardless of its parameterization (Methods 5 and 6), the SPM model yields predictions of the lithiation curves that are significantly less accurate than those obtained via the corresponding DFN model (Methods 1 and 2), especially at higher C-rates (Figure 3.3). The AE parameterizations of the SPM (Methods 5 and 5+) are insensitive to the increased tortuosity caused by the CBD presence, since the assumption of the spatially uniform Li$^+$ concentration c^{e} is blind to any changes in the effective diffusion coefficient in the electrolyte phase, $D_{\mathrm{eff}}^{\mathrm{e}}$. This approximation becomes progressively less accurate as the discharge current density i_{dis} (C-rate) increases, i.e., when the availability of Li$^+$ in the electrolyte plays a limiting role in the cell performance. On the other hand, the AM parameterizations (Methods 6 and 6+) are tailor-made for the SPM, since they capture the CBD-induced changes in the active material properties. Method 6 yields accurate predictions of the total discharge time for all discharge rates and, relative to Method 1, suffers less from the constant coefficients parameterization (Eq. 3.5) at early times.

The lithiation curves predicted via the mDFN model with the alternative parameterization strategies (Methods 3 and 4 from Table 3.2) are exhibited in Figure 3.4. The computation of the Bruggeman exponent b^{e} in Method 4+ is computationally
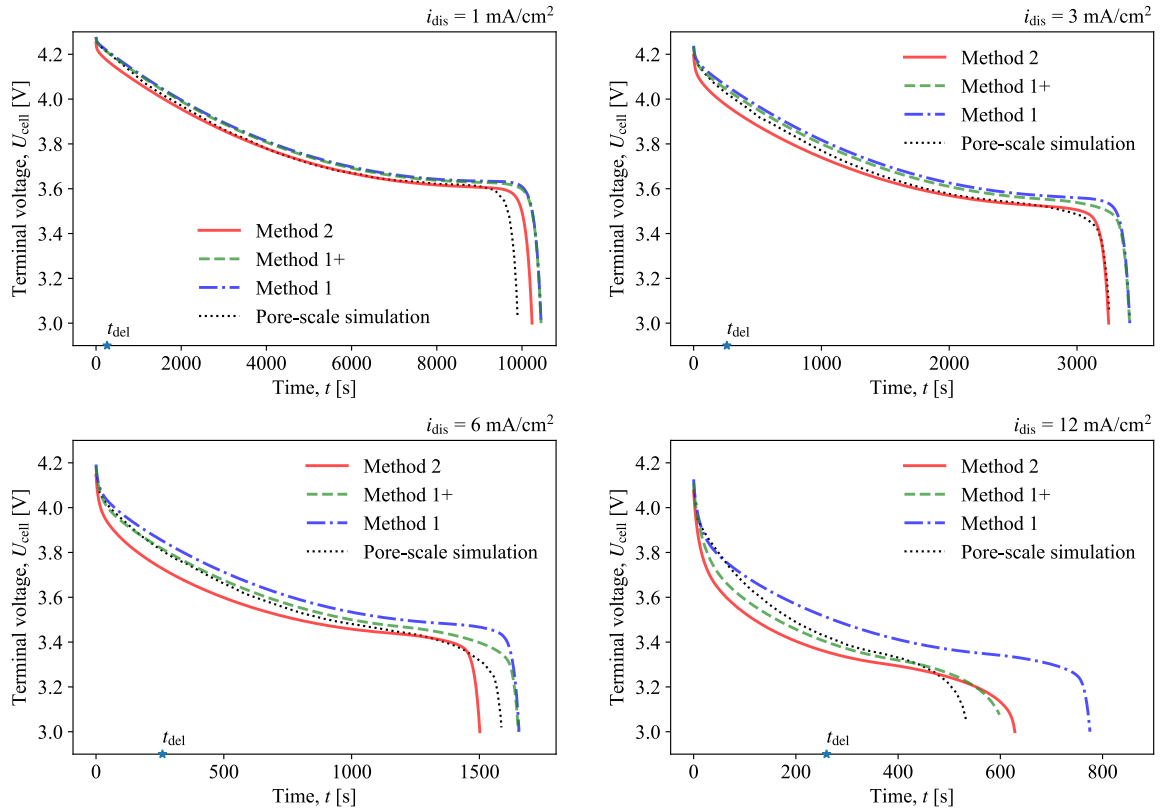
Figure 3.2: Lithiation curves predicted by the DFN model with the alternative parameterizations from Table 3.2, for different discharge current densities i_{dis}. Also shown in this figure are the lithiation curves computed via the pore-scale simulations [32], which serve as the ground truth. The star indicates the intercalation time-delay t_{del}. The parameter values used in these simulations are listed in Tables 3.1 and 3.3.
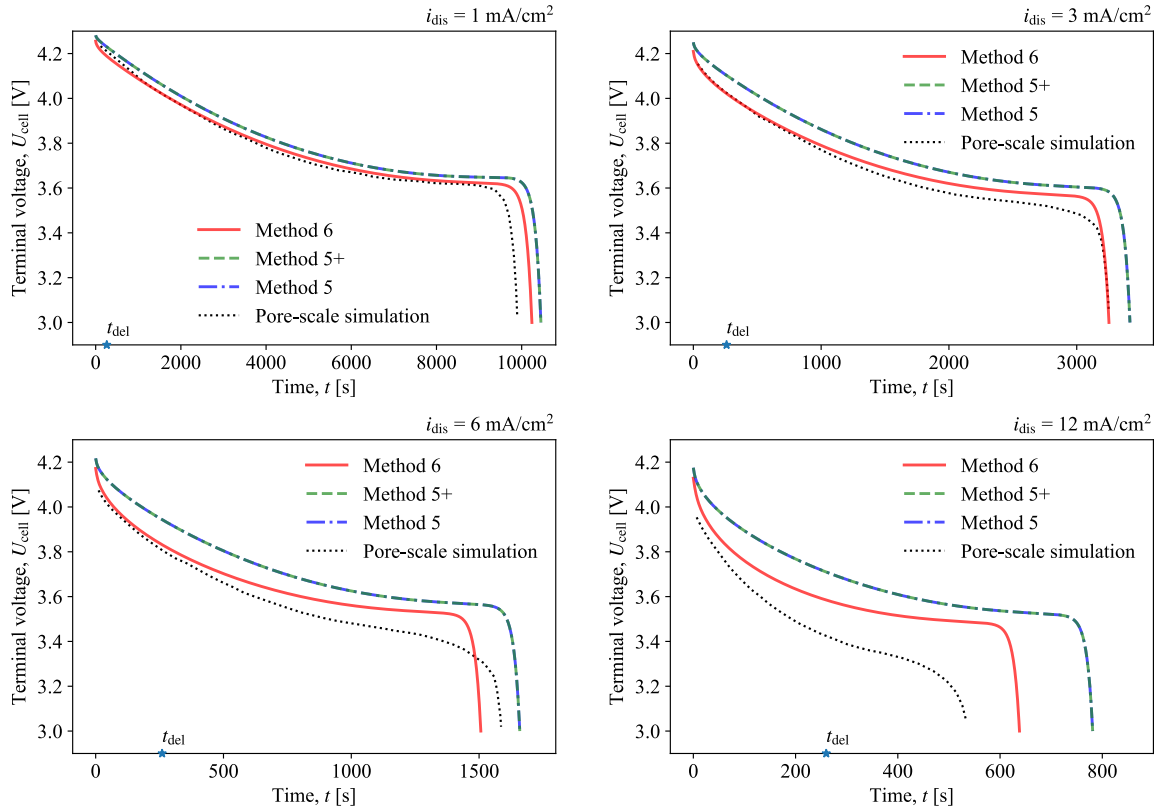
Figure 3.3: Lithiation curves predicted by the SPM model with the alternative parameterizations from Table 3.2, for different discharge current densities i_{dis}. Also shown in this figure are the lithiation curves computed via the pore-scale simulations [32], which serve as the ground truth. The star indicates the intercalation time-delay t_{del}. The parameter values used in these simulations are listed in Tables 3.1 and 3.3.

demanding, since it involves the solution of the closure problem, Eq. 3.4, for each realization of the particle radius drawn from a given distribution; consequently, we do not implement it here. The AM parameterization (Method 4) has the biggest impact on the predictions of the voltage drop at early times, especially for intermediate discharge currents. We posit that this is due to transport within large particles (tail of the distribution), whose intercalation delay time t_{del} is of the same order of magnitude as the discharge time. To confirm this hypothesis, we repeated the simulations (not shown here) for a smaller standard deviation of particle sizes and observed an improved agreement between the mDFN and pore-scale simulations. Overall, the mDFN model does not significantly improve the prediction accuracy of the lithiation curves in the presence of CBD, while increasing the computational time by more than one order of magnitude relative to the DFN model.

The AM parameterization, Eq. 3.5, employs the asymptotic value of the semi-analytical function $\tilde{D}^{\text{s}}(t)$; this asymptote is strictly valid for $t > t_{\text{del}}$ and is used for convenience. [15] To explore the impact of this procedure, we plot the lithiation curves computed via the DFN (Figure 3.5) and mDFN (Figure 3.6) models with the AM+ parameterization (Method 2+ and Method 4+ from Table 3.2, respectively). Method 2+ provides more accurate predictions of the LBM discharge at early times than Method 2 does, while displaying enhanced sharpness of the voltage profile at the intercalation delay time t_{del}. The improvement is even more noticeable when Method 4+ is used instead of Method 4. The increased accuracy of Methods 2+ and 4+ comes at the cost of the increased complexity in computing the time-varying effective diffusivity $\tilde{D}^{\text{s}}(t)$ and the necessity to modify a P2D simulator to allow for time-dependent parameterizations. We argue that Method 2 provides an attractive balance between the computational complexity and the prediction accuracy.

3.5.2 Impact of CBD properties on cell performance

Having established the ability of the properly parameterized DFN and mDFN models to accurately capture the impact of CBD on the lithiation curves for the previously studied LMB [32], we proceed to use these models to forecast the performance of a
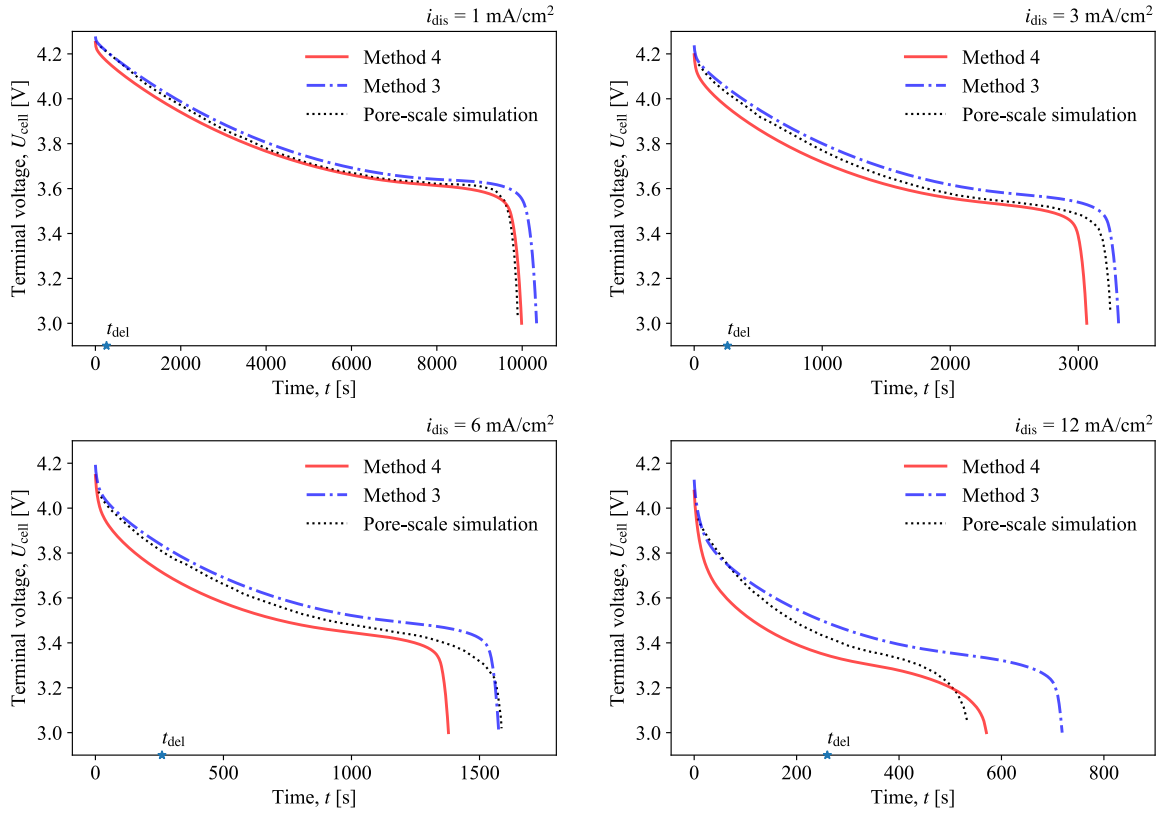
Figure 3.4: Lithiation curves predicted by the mDFN model with the alternative parameterizations from Table 3.2, for different discharge current densities i_{dis}. Also shown in this figure are the lithiation curves computed via the pore-scale simulations [32], which serve as the ground truth. The star indicates the intercalation time-delay t_{del}. The parameter values used in these simulations are listed in Tables 3.1 and 3.3.
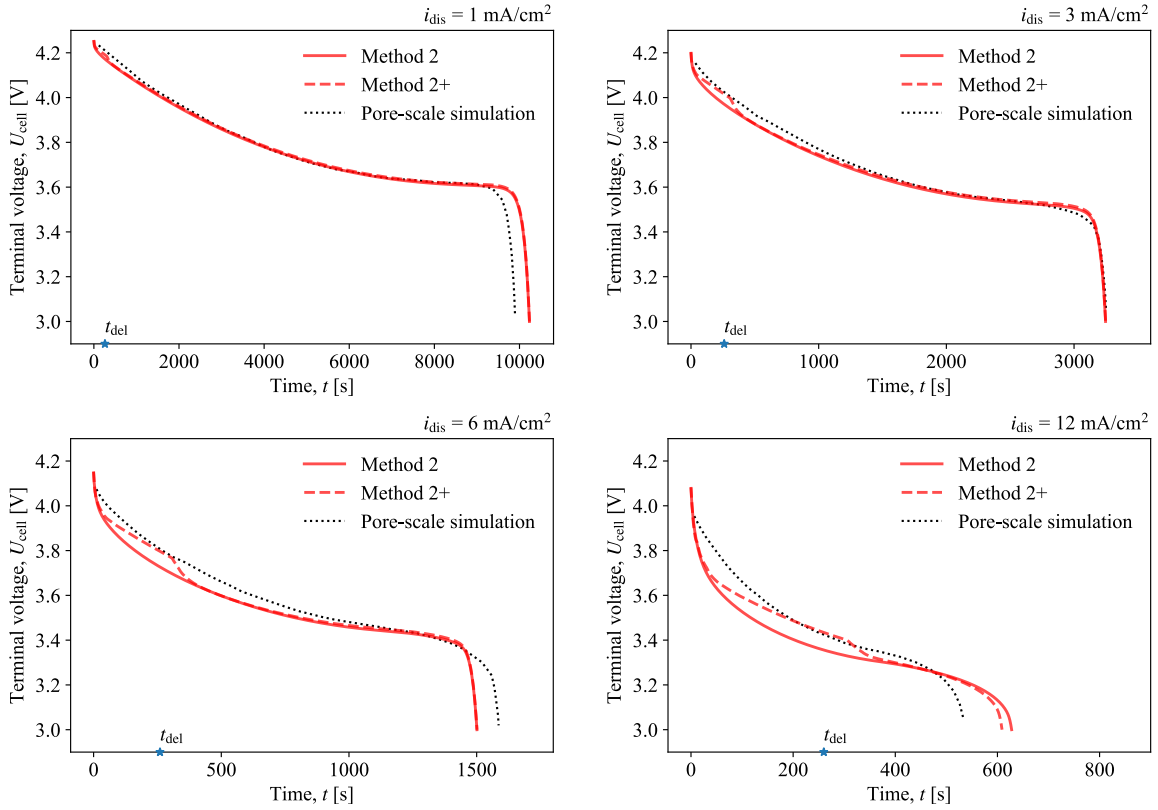
Figure 3.5: Lithiation curves predicted by the DFN model with the AM and AM+ parameterizations (Method 2 and Method 2+ from Table 3.2, corresponding to the constant and time-varying $\tilde{D}^{\mathrm{s}}$, respectively) for different discharge current densities i_{dis}. Also shown in this figure are the lithiation curves computed via the pore-scale simulations [32], which serve as the ground truth. The star indicates the intercalation time-delay τ_{del}. The parameter values used in these simulations are listed in Tables 3.1 and 3.3.
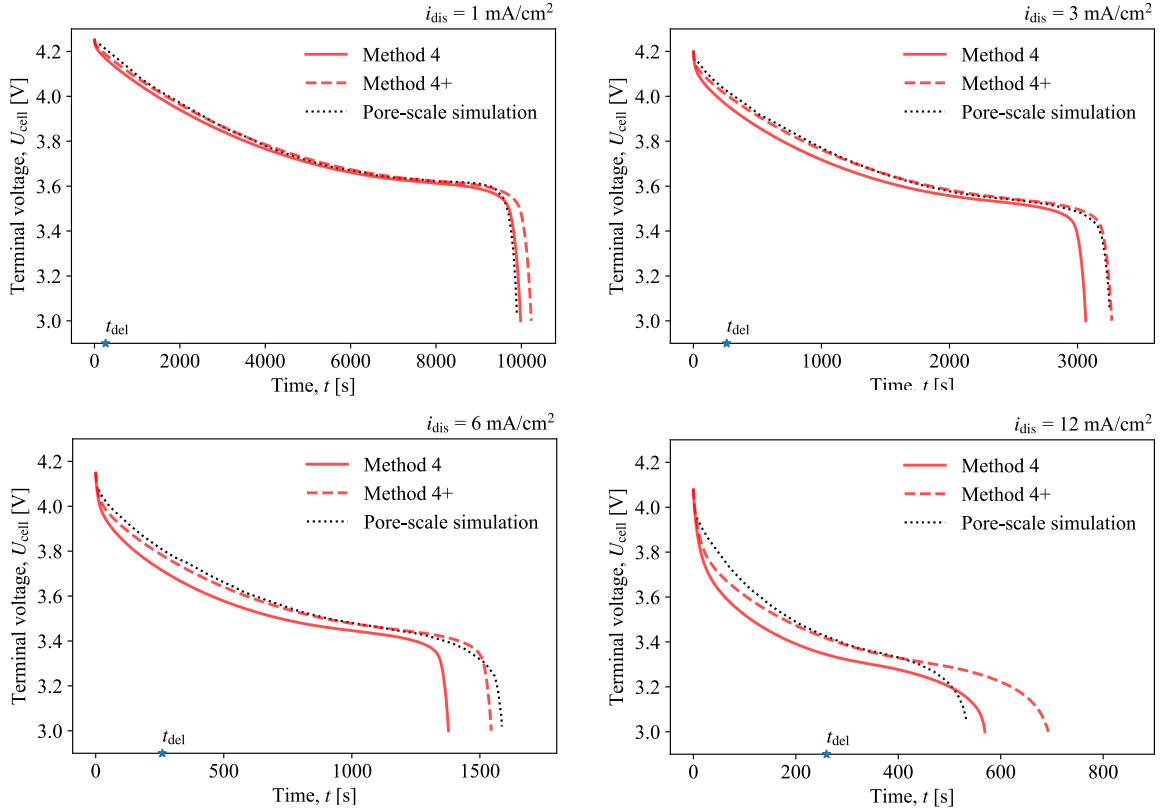
Figure 3.6: Lithiation curves predicted by the mDFN model with the AM and AM+ parameterizations (Method 4 and Method 4+ from Table 3.2, corresponding to the constant and time-varying $\tilde{D}^{\mathrm{s}}$, respectively) for different discharge current densities i_{dis}. Also shown in this figure are the lithiation curves computed via the pore-scale simulations [32], which serve as the ground truth. The star indicates the intercalation time-delay τ_{del}. The parameter values used in these simulations are listed in Tables 3.1 and 3.3.

Table 3.4: Values of the effective parameters in Method 2.

	CBD volume fraction, $1 - v$			
	0	0.06	0.10	0.14
Porosity, ω [-]	0.417	0.357	0.317	0.277
Solid phase volume fraction, $1 - \omega$ [-]	0.583	0.643	0.683	0.723
Solid particle reference radius, $\tilde{R}^s$ [μm]	7.84	8.1	8.27	8.42
Coefficient of variation, $\sigma_R / \tilde{R}^s$ [-]	0.46	0.46	0.46	0.46
Solid-phase diffusivity, $\tilde{D}^s$ [10^{-14} m^2/s]	4.303	3.158	2.177	1.549
Solid-phase conductivity, $\tilde{\sigma}^s$ [S/m]	2.8	0.596	0.398	0.302
Reaction rate, $\tilde{k}_0$ [10^{-11} m$^{2.5}$/s/mol$^{0.5}$]	1.523	0.818	0.781	0.751
Maximum Li concentration, $\tilde{c}^s_{max}$ [mol/m^3]	50451	45759	43085	40663

cell utilizing different volume fractions and material properties of CBD. The effective parameters for Method 2, computed via Eq. 3.5, are summarized in Table 3.4.

Figure 3.7 exhibits the lithiation curves for several CBD configurations predicted via Method 2. Each of these configurations differs from the reference LBM properties in Table 3.3 by a single CBD characteristic: the CBD volume fraction in the solid phase $1 - v$ (Figure 3.7a), the CBD ionic conductivity σ^{CBD} (Figure 3.7b), and the CBD ionic diffusivity D^{CBD} (Figure 3.7c). The battery discharge time decreases as either the CBD volume fraction increases or the CBD ionic diffusivity decreases, and is insensitive to the ionic conductivity of CBD. The quantitative nature of these observations can be used in the optimal design of porous cathodes.

3.6 Summary

P2D models are routinely used to predict the lithiation curves for energy storage devices, including LMBs. The performance of such models is as good as their parameterization, which remains a challenge especially in the presence of CBD. We proposed two alternative parameterization strategies, which explicitly account for the CBD volume fraction and physical properties. The first (electrolyte-augmented parameterization or AE+) aggregates CBD with the electrolyte-filled pore space and expresses the augmented Bruggeman exponent in terms of a solution of microstructure-specific
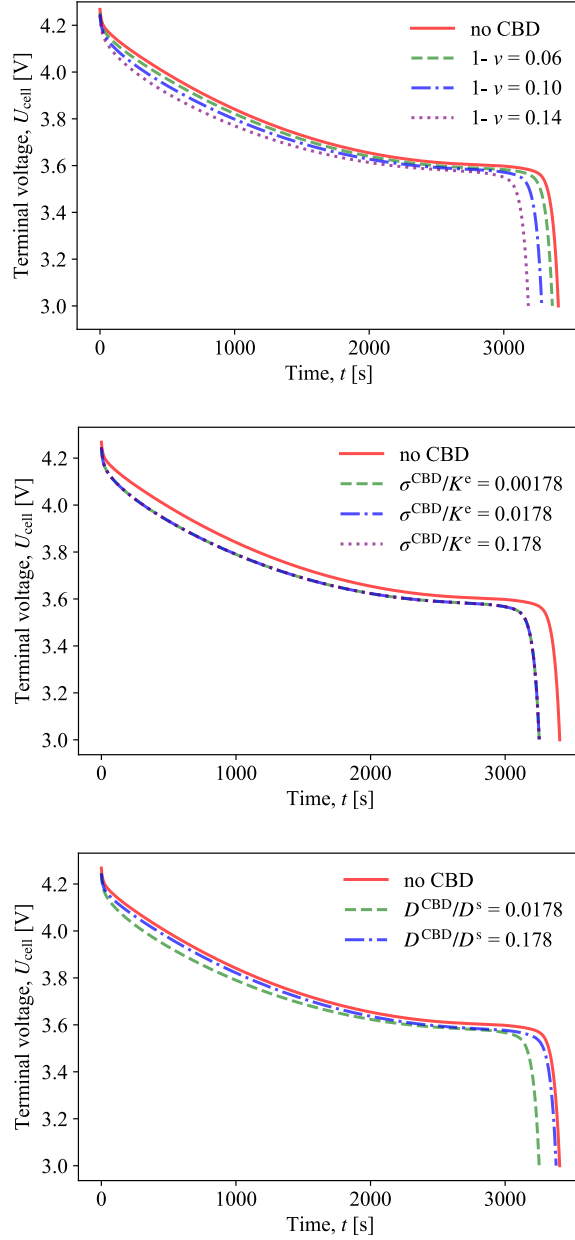
Figure 3.7: Lithiation curves for LMBs, whose porous cathode employs different CBD configurations. Each of these configurations differs from the reference LBM properties in Table 3.3 by a single CBD characteristic: the CBD volume fraction $1-v$ (top), the CBD ionic conductivity σ^{CBD} (middle), and the CBD ionic diffusivity D^{CBD} (bottom). The corresponding model parameters are collated in Table 3.4. The discharge current density is set to $i_{\mathrm{dis}} = 3$ mA/cm^2.

closure problem. The second (active material-augmented parameterization or AM) treats CBD and active particles as a composite solid phase, whose effective properties are computed (semi-)analytically via homogenization. When applied to the three P2D models (DFN, mDFN, and SPM), these parameterizations, and their enhancements, give rise to Methods 1 – 6, whose labels are assigned in Table 3.2. We conducted a series of numerical experiments that lead to the following major conclusions.

- Both AE+ and AM parameterizations of the three P2D models outperform their currently used counterparts in terms of the prediction accuracy of the lithiation curves at all C-rates considered.

- Regardless of its parameterization (Methods 5 and 6), the SPM yields predictions of the lithiation curves that are significantly less accurate than those obtained via the corresponding DFN model (Methods 1 and 2), especially at higher C-rates.

- The mDFN model provides a modest improvement in the prediction accuracy of the lithiation curves in the presence of CBD, while increasing the computational time by more than one order of magnitude relative to the DFN model.

- Increased accuracy of the transient parameterizations is balanced by the cost of computing the time-varying effective diffusivity and the need to modify a P2D simulator. Our AM parameterization of the DFN model provides an attractive middle ground between the model complexity and the prediction accuracy.

- The battery discharge time decreases as either the CBD volume fraction increases or the CBD ionic diffusivity decreases, and is insensitive to the CBD ionic conductivity. The quantitative nature of these observations can be used in the optimal design of porous cathodes.

The accuracy of the alternative P2D Methods discussed above is ascertained in terms of their ability to match the lithiation curves predicted via the pore-scale simulations [32] for a given LMB microstructure. While we treat these pore-scale results as ground truth, it is worthwhile mentioning that they depart from experimental

data [32] at high C-rates. This suggests the need to construct more representative, yet computationally tractable, alternatives to the currently used P2D models. Other venues for future research are to study CBD morphologies other than a uniform CBD coating of spherical active-material particles, and Li batteries other than NMC622 used here for demonstration purposes.

Chapter 4

Stability-guided strategies to mitigate dendritic growth in lithium-metal batteries

4.1   Abstract

Dendritic growth is a leading cause of degradation and catastrophic failure of lithium-metal batteries. Deep understanding of this phenomenon would facilitate the design of strategies to reduce, or completely suppress, the instabilities characterizing electrodeposition on the lithium anode. We present a linear-stability analysis, which utilizes the Poisson-Nernst-Planck equations to describe Li-ion transport and, crucially, accounts for the lack of electroneutrality. This allows us to investigate the impact of electric-field gradients near the electrode surface on both ion diffusion and its anisotropy. Our analysis indicates that the use of anisotropic electrolytes (i.e., electrolytes with anisotropic diffusion coefficients of the Li ions) and the control of the local electric field can suppress dendritic growth of lithium metal. Specifically, changes in the local electric field can be used to enhance the longitudinal (perpendicular to the electrode) component of the cation diffusion coefficient tensor, which decreases the maximum growth rate of the dendrites. Electrolytes with electric field-dependent diffusion coefficients would reduce dendritic growth in small batteries, while anisotropic

electrolytes (or separators with anisotropic pore structures or columnized membranes) are appropriate for batteries of any size.

4.2 Introduction

Dendritic growth of lithium metal is a leading cause of degradation and catastrophic failure of Li-metal batteries. Understanding the unstable dendrite growth during electrodeposition, which has been observed in many experimental studies [70, 71, 72, 73], is crucial to the design and safe operation of Li-metal batteries. Linear stability analyses [74, 75, 76, 77, 78] can reveal important aspects of the dynamics associated with these instabilities. Of direct relevance to our study are investigations of the possible stabilizing effects of a negative background charge in porous media and of dependence of the crystal grain size on duty cycle in pulse electroplating [79]. Linear stability analyses of electrodeposition were also used to study the mechanical stabilization effects of external pressure [80], elastic deformation [81] and electroconvection [82], as well as other stabilization mechanisms such as thin-film piezoelectricity [83] and superimposition of AC forcing on a base DC field [84].

These and other similar stability analyses rest on the assumption of local electroneutrality. Although this simplification is adequate under normal operating conditions, the deviation from electroneutrality can be significant when the applied current is high [85]. Investigations of this regime [86, 73, 87], in which the cell overpotential ranged between 1.9 V and 3.7 V, aim to understand Li-metal battery cycling performance and dendrite growth on the fast-charging lithium-metal anode [86]. In such an overlimiting regime, the electrode surface becomes highly unstable [88]. The lack of electroneutrality implies the existence of an extended space-charge region [89] that significantly affects ion transport in the entire system [90]. It affects transport properties of the electrolyte, such as possible anisotropy of ion diffusion and dependence of the disparate diffusion coefficients of cations and anions on a strong electric field gradient near the electrode surface.

Anisotropy of ion diffusion in the electrolyte may provide a means to control dendritic growth of the lithium metal, because large gradients in the ion concentration

parallel to the electrodes play a destabilizing role [91]. Dendrite formation and growth can be suppressed either by using an anisotropic electrolyte [92] or by inducing the anisotropy via application of an electric field, which engenders ionic drift diffusion and changes the transport properties [93, 94]. Recent molecular dynamics simulations [95, 96] also show that electric fields alter the diffusion coefficients of cations and anions in the electrolyte and render them direction-dependent.

Motivated by these findings, we perform a linear stability analysis of electrodeposition without resorting to the electroneutrality assumption. Our study extends the stability analysis [88] to include the mechanisms by which a local electric field close to the electrode surface alters ion diffusion and enhances its anisotropic behavior. The base- and perturbed-state equations are solved numerically to compute the spatial distributions of the electric potential, charge density, and Li-ion concentration. These numerical solutions allow us to construct dispersion relations for the parameter space of interest. The comparison of the stability conditions with and without the electric field effects identifies potential mechanisms for reducing, and even suppressing, dendritic growth. In the vicinity of the electrode surface, larger values of the applied electric potential magnify the impact of (potential-dependent) ionic diffusivity on both the maximum growth rate and charge density. For example, the maximum growth rate is about 24% smaller than its counterpart for the constant isotropic diffusion coefficient.

4.3   Mathematical Formulation

We study electrodeposition on the lithium anode in a two-dimensional half-cell domain, $\Omega = \Omega_s \cup \Omega_f$ (Figure 4.1). The Li-metal electrode surface $\Gamma(t)$, which separates the Li-metal anode $\Omega_s(t)$ from the liquid electrolyte $\Omega_f(t)$, is initially located at $x = 0$. A negative electrostatic potential, ϕ_e, is maintained on $\Gamma(t)$; the electric potential at the outer edge of the electrolyte ($x = L$) is fixed at 0. The initial concentration of lithium cations, Li^+, in the binary dilute electrolyte electrolyte is c_0. At the electrode surface, Γ, the cations, Li^+, undergo a Faradaic reaction with electrons, e^-, and reduce to Li atoms, $Li^+ + e^- \rightarrow Li$, which are subsequently deposited on the electrode

surface.

This deposition causes the Li-metal surface $\Gamma(t)$ to change with time t. We study this evolution in the two-dimensional Cartesian coordinate system spanned by the orthogonal unit-vectors $\mathbf{e}_x$ and $\mathbf{e}_y$, and represent the moving interface, $\Gamma(t)$, by a single-valued function $h(y, t)$ such that $h(y, 0) = 0$ (Figure 4.1). Our focus is on the stability of the electrodeposition, i.e., of the temporal evolution of $h(y, t)$.
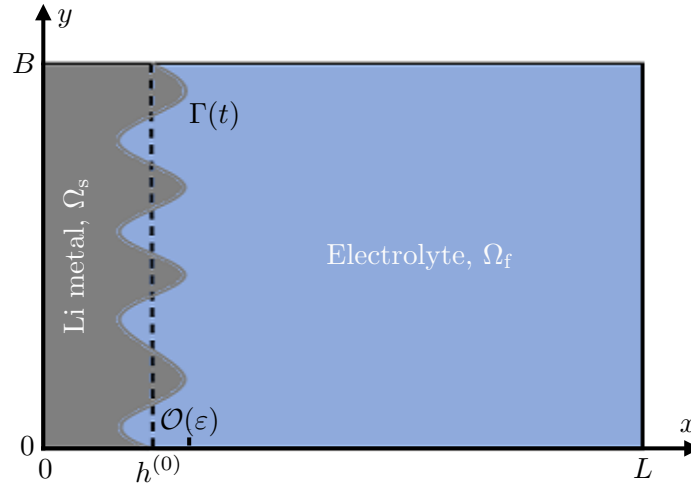
Figure 4.1: Schematic representation of a two-dimensional half-cell domain $\Omega = \Omega_{\mathrm{s}} \cup \Omega_{\mathrm{f}}$. The interface between the Li metal, Ω_{s}, and liquid electrolyte, Ω_{f}, is denoted by Γ. The coordinate system moves in the positive x direction with velocity U, which is the average deposition rate on the electrode.

4.3.1 Governing equations

Under isothermal conditions and in the absence of a magnetic field, the state of an immobile dilute electrolyte at any point $\mathbf{x} = (x, y)^\top \in \Omega_{\mathrm{f}} = \{\mathbf{x} : h(y, t) \leq x \leq L, 0 \leq y \leq B\}$ and time t is defined by the concentrations (mol/m^3) of cations, $c_+(\mathbf{x}, t)$, and anions, $c_-(\mathbf{x}, t)$, and by the electric potential $\phi(\mathbf{x}, t)$ (V). Spatial variability of these three state variables induces mass fluxes of cations, $\mathbf{J}_+(\mathbf{x}, t)$, and anions, $\mathbf{J}_-(\mathbf{x}, t)$,

$$\mathbf{J}_\pm = -\mathbf{D}_\pm \left(\nabla c_\pm + \frac{z_\pm c_\pm F}{RT} \nabla \phi \right), \tag{4.1a}$$

where $\mathbf{D}_{\pm}$ are the diffusion coefficients (m^2/s), whose tensorial nature accounts for possible anisotropy; $z_{\pm}$ are the charge numbers (valences) of the cations and anions; F is the Faraday constant (s·A/mol); R is the gas constant (J/mol/K); and T is the temperature (K). Mass conservation in the electrolyte is described by the Nernst-Planck equations,

$$\frac{\partial c_{\pm}}{\partial t} = -\nabla \cdot \mathbf{J}_{\pm}, \qquad \mathbf{x} \in \Omega_{\mathrm{f}}, \quad t > 0. \tag{4.1b}$$

The electric potential, ϕ, is governed by the Poisson equation,

$$-\epsilon \nabla^2 \phi = z_+ F c_+ + z_- F c_-, \qquad \mathbf{x} \in \Omega_{\mathrm{f}}, \quad t > 0, \tag{4.2}$$

where ϵ is the absolute permittivity of the solvent (F/m).

The electrode's surface $\Gamma(t)$ is impervious to inert (non-reactive) anions, i.e.,

$$\mathbf{n} \cdot \mathbf{J}_- = 0, \qquad \mathbf{x} \in \Gamma, \quad t > 0, \tag{4.3}$$

where $\mathbf{n}$ is the normal vector pointing outward from the electrolyte. The normal component of the cation flux, $\mathbf{J}_+$, through this surface is balanced by the Faradaic reaction Li$^+ + e^- \to$ Li such that

$$\mathbf{n} \cdot \mathbf{J}_+ = R_{\mathrm{Li}}, \qquad \mathbf{x} \in \Gamma, \quad t > 0, \tag{4.4a}$$

where R_{Li} is the rate of production of lithium atoms [79]. This condition is supplemented with the minimum Li$^+$ concentration condition at the electrode surface [88]:

$$\mathbf{n} \cdot \nabla c_+ = 0, \qquad \mathbf{x} \in \Gamma, \quad t > 0. \tag{4.4b}$$

The production rate R_{Li} is given by the Butler-Volmer equation,

$$R_{\mathrm{Li}} = -\frac{k_0}{\gamma_{\mathrm{ts}}} \left[\exp\left(\alpha_{\mathrm{an}} \frac{zF\eta_\alpha + 2\omega\gamma\kappa}{RT} \right) - \frac{c_+(\mathbf{x} \in \Gamma, t)}{c_+^{\ominus}} \exp\left(-\alpha_{\mathrm{cat}} \frac{zF\eta_\alpha + 2\omega\gamma\kappa}{RT} \right) \right], \tag{4.5}$$

where k_0 is the reaction rate constant (mol/m^2/s); γ_{ts} is the activity coefficient of the transition state for the Faradaic reaction (−); z is the number of electrons involved

in the electrode reaction; α_{an} and α_{cat} are the anodic and cathodic charge-transfer coefficients, respectively $(-)$; $c_+^\ominus$ is the standard concentration; ω is the molar volume of Li metal (m^3/mol); γ is the isotropic surface energy of the Li metal (J/m^2), and $\kappa(y, t)$ is the mean curvature of $\Gamma(t)$ (m^{-1}). The activation overpotential $\eta_\alpha(\mathbf{x} \in \Gamma, t)$ is defined as

$$\eta_\alpha = \phi_{\text{e}} - \phi(\mathbf{x} \in \Gamma, t) - E^\ominus, \tag{4.6}$$

where $E^\ominus$ is the standard electrode potential. We set $\gamma_{\text{ts}} = 1$, $\alpha_{\text{an}} = 1 - \alpha_{\text{cat}}$, and $E^\ominus = 0$. The interfacial current density I is related to the reaction rate R_{Li} by

$$I = zFR_{\text{Li}}. \tag{4.7}$$

The boundary conditions on the moving interface $\Gamma(t)$, Eqs. (4.3) and (4.4), are supplemented with a kinematic condition that describes the spatiotemporal evolution of Γ. The normal-vector $\mathbf{n}(y, t)$ and mean curvature $\kappa(y, t)$ of Γ are expressed in terms of the derivatives of $h(y, t)$ as [88]

$$\mathbf{n} = \frac{1}{\sqrt{1 + (\partial_y h)^2}} \begin{pmatrix} -1 \\ \partial_y h \end{pmatrix}, \qquad \kappa = -\frac{1}{2} \frac{\partial_y^2 h}{[1 + (\partial_y h)^2]^{3/2}}. \tag{4.8}$$

The rate of change of $\Gamma(t)$, or equivalently of $h(y, t)$, is given by the current into the anode [88, 79],

$$\mathbf{e}_x \cdot \mathbf{n} \frac{\partial h(y, t)}{\partial t} = -\frac{\omega I}{zF}. \tag{4.9}$$

The boundary conditions on the remaining segments of the computational domain Ω_{f} are

$$\phi = 0, \qquad c_+ = c_0, \qquad c_- = c_0, \qquad \text{for } x = L; \tag{4.10a}$$

$$\frac{\partial \phi}{\partial y} = 0, \qquad \frac{\partial c_+}{\partial y} = 0, \qquad \frac{\partial c_-}{\partial y} = 0, \qquad \text{for } y = 0 \text{ and } B. \tag{4.10b}$$

The boundary conditions at $x = L$ reflect an assumption that small (magnitude ε) perturbations of the anode surface do not affect the ion concentrations the half-cell distance away; this assumption is effectively enforced in the full-cell linear stability

analyses[88, 79] that impose identical perturbations on both cathode and anode (Figure 4.8 provides a comparison of our results with those reported in Ref. 79). The last three boundary conditions in Eq. (4.10) imply that the horizontal surfaces, $y = 0$ and B, are electrically insulated and impermeable.

4.3.2 Diffusivity alteration by electric field

The presence of an electric field, $\mathbf{E} = (E_x = -\partial_x \phi, E_y = -\partial_y \phi)^\top$, alters the diffusion coefficients of cations and anions, $D_\pm$, rendering them direction-dependent, $\mathbf{D}_\pm$ [95, 96]. Both the magnitude of the diffusion coefficients and the degree of their anisotropy increase with the magnitude of E_x or E_y. We adopt the exponential model derived from the molecular dynamics simulations of 1M solution of LiPF$_6$ in ethylene carbonate [95],

$$\mathbf{D}_\pm = D_\pm^{\mathrm{ref}} \begin{pmatrix} e^{b_\pm |E_x|} & 0 \\ 0 & e^{b_\pm |E_y|} \end{pmatrix} = D_\pm^{\mathrm{ref}} \begin{pmatrix} e^{b_\pm \partial_x \phi} & 0 \\ 0 & e^{b_\pm \partial_y \phi} \end{pmatrix}. \tag{4.11}$$

where $D_\pm^{\mathrm{ref}}$ are the isotropic diffusion coefficients of cations and anions when $|\mathbf{E}| = 0$, and the fitting parameters $b_\pm$ (m/V) account for the strength of the electric field.

Like many others, our model of dendritic growth, Eqs. (4.1)–(4.10), rests on the dilute-solution formulation. Measurements of the activity coefficient for LiPF$_6$ in PC/EC/DMC for a wide range of concentration (up to 4M) found it to be close to 1 for concentrations up to 1M [97], indicating that the dilute formulation holds. This finding is seemingly contradicted by the study [98] that found the solutions of LiPF$_6$ in PC/EC/EMC for the concentration range 0.0625–1M not to be "dilute"; yet, it showed that the dilute-solution model of these solutions overestimates the specific energy of a lithium-ion cell by only 0.6%. Be that as it may, our analysis can accommodate other dependencies of $\mathbf{D}_\pm$ on $\mathbf{E}$, and the one in Eq. (4.11) is used for the sake of concreteness.

4.4 Linear Stability Analysis

Linear stability analysis is performed by applying a small perturbation, $\varepsilon \exp(wt + iky)$, to a one-dimensional steady-state base state, $h^{(0)}(t) \equiv Ut$, $\phi^{(0)}(x)$ and $c_\pm^{(0)}(x)$. Here, ε is the small dimensionless parameter, w is the growth rate (1/s), k is the wave number (1/m), and $i^2 = -1$. The electrodeposition process is unstable if the perturbations grow with time, i.e., if $w > 0$. The goal of a stability analysis is to express w in terms of the physical properties of the electrolyte and the anode.

To facilitate this analysis, we rewrite (4.1)–(4.11) in terms of dimensionless variables

$$\tilde{x} = \frac{x}{L}, \quad \tilde{y} = \frac{y}{L}, \quad \tilde{t} = \frac{tD_+^{\text{ref}}}{L^2}, \quad \tilde{c}_\pm = \frac{c_\pm}{c_0}, \quad \tilde{\phi} = \frac{F\phi}{RT}, \quad \tilde{h} = \frac{h}{L}, \quad \tilde{U} = \frac{UL}{D_+^{\text{ref}}},$$
$$\tilde{D}_\pm = \frac{D_\pm}{D_+^{\text{ref}}}, \quad \tilde{b}_\pm = \frac{RTb_\pm}{FL}, \quad \tilde{\lambda}_D^2 = \frac{RT\epsilon}{2L^2F^2c_0}, \quad \text{Ca} = \frac{\omega\gamma}{RTL}, \quad \tilde{R}_{\text{Li}} = \frac{LR_{\text{Li}}}{D_+^{\text{ref}}c_0}. \tag{4.12a}$$

The corresponding dimensionless parameters describing the perturbation of the anode surface, Γ, are

$$\tilde{k} = kL, \qquad \tilde{w} = \frac{L^2w}{D_+^{\text{ref}}}. \tag{4.12b}$$

The dimensionless Li production rate $\tilde{R}_{\text{Li}}$ and interfacial current density $\tilde{I}$ are

$$\tilde{R}_{\text{Li}} = -\tilde{k}_0 e^{-\alpha_{\text{cat}}(z\tilde{\eta}_\alpha + 2\tilde{\omega}\tilde{\kappa})}\left[e^{z\tilde{\eta}_\alpha + 2\text{Ca}\tilde{k}} - \frac{\tilde{c}_+}{\tilde{c}_+^\Theta}\right], \qquad \tilde{I} = \frac{I}{I_{\text{lim}}} = \frac{z\tilde{R}_{\text{Li}}}{2}, \tag{4.12c}$$

where

$$\tilde{k}_0 = \frac{Lk_0}{D_+^{\text{ref}}c_0\gamma_{\text{ts}}}, \quad \tilde{\eta}_\alpha = \frac{F\eta_\alpha}{RT}, \quad \tilde{\kappa} = L\kappa, \quad \tilde{c}_+^\Theta = \frac{\tilde{c}_+^\Theta}{c_0}, \quad I_{\text{lim}} = \frac{2FD_+^{\text{ref}}c_0}{L}. \tag{4.12d}$$

Unless specified otherwise, all the quantities discussed from here on are dimensionless, even though we drop the tildes to simplify the notation. In a linear analysis, the electrode surface height, $h(y,t)$, and the state variables $\phi(x,y,t)$ and $c_\pm(\mathbf{x},t)$ are

written as

$$h(y,t) = h^{(0)}(t) + \varepsilon h^{(1)} \mathrm{e}^{wt+iky} \tag{4.13}$$

$$\phi(\mathbf{x},t) = \phi^{(0)}(x) + \varepsilon \phi^{(1)}(x)\mathrm{e}^{wt+iky} \tag{4.14}$$

$$c_\pm(\mathbf{x},t) = c_\pm^{(0)}(x) + \varepsilon c_\pm^{(1)}(x)\mathrm{e}^{wt+iky}, \tag{4.15}$$

where the constant $h^{(1)}$ and the functions $\phi^{(1)}$ and $c_\pm^{(1)}$ are the first-order (in ε) corrections. Then, the interfacial conditions (4.3)–(4.11) are expanded in Taylor series around the leading-order interface $h^{(0)}$, which is moving with the constant velocity $U = \mathrm{d}h^{(0)}/\mathrm{d}t = -\omega R_{\mathrm{Li}}^{(0)}$; e.g., $\phi(\mathbf{x} \in \Gamma, t) \approx \phi(h^{(0)}, y, t) + \dots$. Finally, the terms of equal power of ε are collected to specify boundary-value problems (BVPs) for the base state (of order ε^0) and the first-order correction (of order ε). These calculations are reported in the Appendix; the BVP for the base-state variables $c_\pm^{(0)}(\xi)$ and $\phi^{(0)}(\xi)$ consists of Eqs. (A.7) and (A.8), and the BVP for the perturbed-state variables $c_\pm^{(1)}(\xi)$ and $\phi^{(1)}(\xi)$ comprises Eqs. (A.9) and (A.10). Both BVPs are written in the moving coordinate system $(\xi \equiv x + \omega R_{\mathrm{Li}}^{(0)} t, y)^\top$.

The base-state Eqs. (A.7) and (A.8) are solved numerically with the Matlab function `bvp4c` to obtain $c_\pm^{(0)}(\xi)$, $\phi^{(0)}(\xi)$, and their first- and second-order derivatives. These are then used as coefficients in the perturbed-state Eqs. (A.9) and (A.10); the numerical solution is obtained [79] by employing a second-order finite-difference scheme and solving the resulting generalized eigenvalue problem with the Matlab function `eigs`.

4.5   Results and discussion

The parameters used in our simulations are presented in Table 4.1. We start by computing the base-state solution for constant isotropic diffusion coefficients, $D_\pm$, (i.e., for Eq. (4.11) with $b_\pm = 0$) for a wide range of the applied electric potential ϕ_e. Figure 4.2 shows the concentrations of cations, $\tilde{c}_+^{(0)}$, and anions, $\tilde{c}_-^{(0)}$; the charge density $\tilde{\rho}_\mathrm{e}^{(0)} = \tilde{c}_+^{(0)} - \tilde{c}_-^{(0)}$; and the electric potential $\tilde{\phi}^{(0)}$. These dimensionless quantities are computed for the half-cell length $L = 5~\mu$m, which corresponds to the limiting current

Table 4.1: Parameters used in the simulations.

Parameter	Symbol	Value	Units	Ref
Half-cell length	L	0.5, 5, 50	μm	88
Cation diffusivity without electric field	D_+^{ref}	$1.61 \cdot 10^{-11}$	m^2/s	99
Anion diffusivity without electric field	D_-^{ref}	$3.91 \cdot 10^{-11}$	m^2/s	99
Exponent in cation diffusion tensor	b_+	$2.31 \cdot 10^{-9}$	m/V	95
Exponent in anion diffusion tensor	b_-	$2.49 \cdot 10^{-9}$	m/V	95
Temperature	T	298.15	K	
Molecular weight of lithium metal	M	6.941	g/mol	100
Density of lithium metal	ρ	0.534	g/cm^3	100
Li^+ bulk concentration	c_0	1000	mol/m^3	
Standard concentration	$c^{\ominus}$	1000	mol/m^3	
Standard electrode potential	$E^{\ominus}$	0	V	
Dielectric constant	ϵ/ϵ_0	90	-	101
Vacuum permittivity	ϵ_0	$8.854 \cdot 10^{-12}$	F/m	102
Reaction rate constant	k_0	$2.7 \cdot 10^{-3}$	$\text{mol/(m}^2\cdot\text{ s)}$	103
Surface energy of metal/electrolyte interface	γ	1	J/m^2	76
Activity coefficient of the transition state	γ_{ts}	1	-	

density $I_{\text{lim}} = 2FD_+^{\text{ref}}c_0/L = 62.1 \text{ mA/cm}^2$. For small values of the applied potential, $\phi_{\text{e}} = -0.1$ V, the base-state current density $I^{(0)}$ is smaller than I_{lim}, the cations at the electrode surface are not depleted, and electroneutrality holds throughout the simulation domain. On the other hand, for large ϕ_{e} when $I^{(0)}$ reaches I_{lim}, the Li-cation concentration $c_+^{(0)}(\xi)$ is approximately zero near the electrode surface and local electroneutrality is violated within the boundary layer, $0 \leq \tilde{\xi} \leq 0.02$; for $L = 5$ μm, its width is $0.02 \cdot 5 = 0.1$ μm. Figure 4.2 also shows that higher values of the applied potential ϕ_{e} induce larger values of the electric potential gradient, $\partial_\xi \phi^{(0)}$, near the electrode surface.

In accordance with Eq. (4.11), the electric field $\mathbf{E} = -\nabla\phi$ gives rise to anisotropic ionic diffusion. Since for the base state $\mathbf{E}^{(0)} = (-j_\phi^{(0)}, 0)^\top$, the leading-order approximations of the principal components of the diffusion tensor $\mathbf{D}_\pm^{(0)}$ in Eq. (A.1) become $D_{xx}^\pm = D_\pm^{\text{ref}} \exp(b_\pm j_\phi^{(0)})$ and $D_{yy}^\pm = D_\pm^{\text{ref}}$, i.e., the diffusion anisotropy manifests itself in the boundary layer adjacent to the electrode. Figure 4.3 shows the spatial extent of this region for half-cell lengths $L = 0.5$ and 5 μm. Both the anisotropy ratio D_{xx}^+/D_{yy}^+ and the boundary-layer width increase as L decreases, or ϕ_{e} increases, with
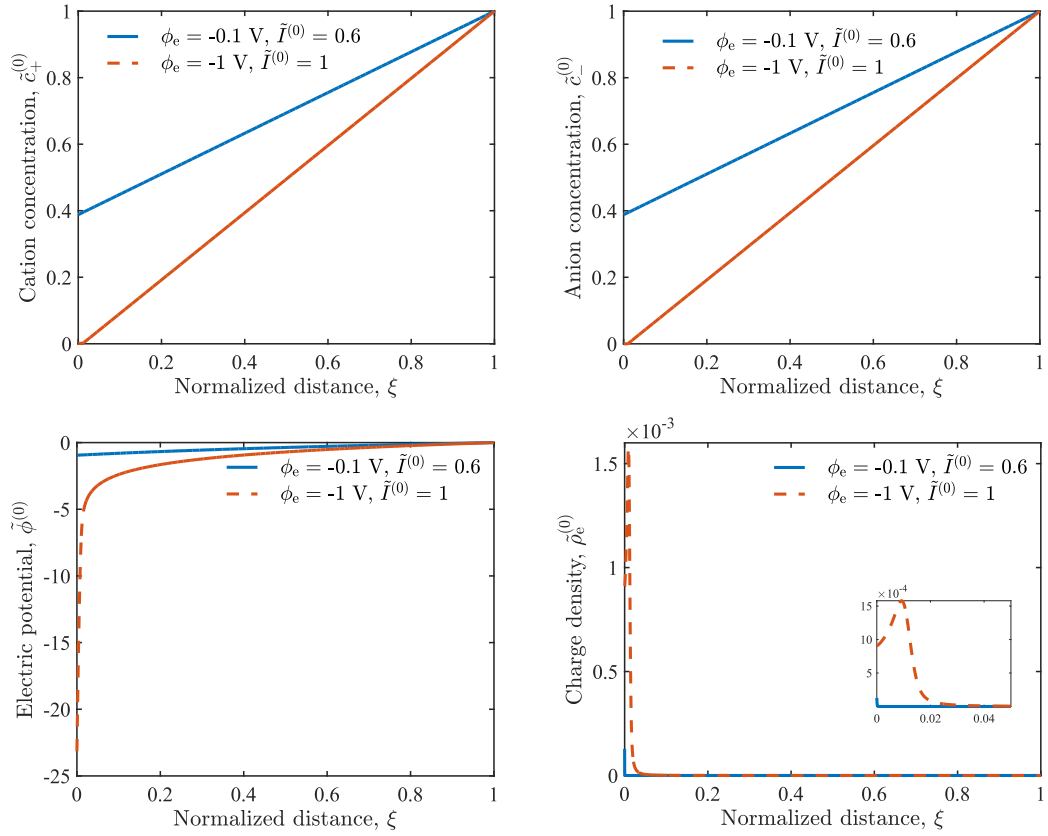
Figure 4.2: Spatial profiles of the base-state cation, $\tilde{c}_+^{(0)}$, and anion, $\tilde{c}_-^{(0)}$, concentrations; electric potential $\tilde{\phi}^{(0)}$; and charge density $\tilde{\rho}_e^{(0)}$ for $L = 5$ μm, $\phi_e = -0.1$ V or -1 V, and constant diffusion coefficients $D_\pm = D_\pm^{\text{ref}}$.

the longitudinal diffusion coefficient D_{xx}^+ being up to 12% larger than its reference value D_+^{ref} for $L = 0.5$ μm and $\phi_e = -3.5$ V.
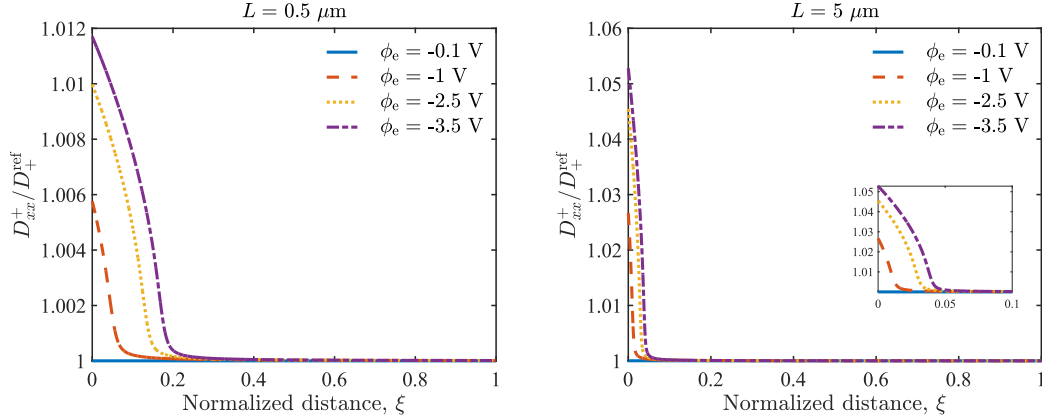
Figure 4.3: Spatial profiles of the normalized longitudinal diffusion coefficient, $D_{xx}^+/D_+^{\text{ref}}$ in Eq. (A.1), for $L = 0.5$ and 5 μm and several values of ϕ_e.

Next, we investigate the impact of the electric field-dependence of ion diffusion on electrodeposition. Specifically, we compare the base-state charge density $\tilde{\rho}_e^{(0)}$ and the perturbed-state growth rates $\tilde{w}$ alternatively computed with either constant diffusion coefficients $D_{\pm}^{\text{ref}}$ or field-dependent diffusion coefficients $\mathbf{D}_{\pm}$ in Eq. (A.1). When the applied electric potential is small ($\phi_e = -0.1$ V) the dependence of the diffusion coefficients on the electric field has negligible effect on the charge density $\tilde{\rho}_e$ (Figure 4.4). This is because in this regime the electric field E is approximately zero (Figure 4.2). Higher values of the applied electric potential ($\phi_e = -2.5$ and -3.5 V) produce the boundary layer within which the electrolyte is not eletroneutral, $E > 0$, the diffusion anisotropy increases in accordance with Eq. (A.1), and the base-state charge density $\tilde{\rho}_e^{(0)}$ near the electrode surface decreases relative to that predicted for the constant diffusion coefficient.

These relatively small and localized changes in electroneutrality (Figure 4.2) and charge density (Figure 4.4) have significant impacts on the dendrite growth rate $\tilde{w}$ when the applied electric potential ϕ_e becomes large (Figure 4.5). For small ϕ_e, i.e., for underlimiting current ($I^{(0)} < I_{\text{lim}}$), the growth rate $\tilde{w}$ is negative for all wavenumbers $\tilde{k} > 0$. This means that the electrode surface growth is unconditionally
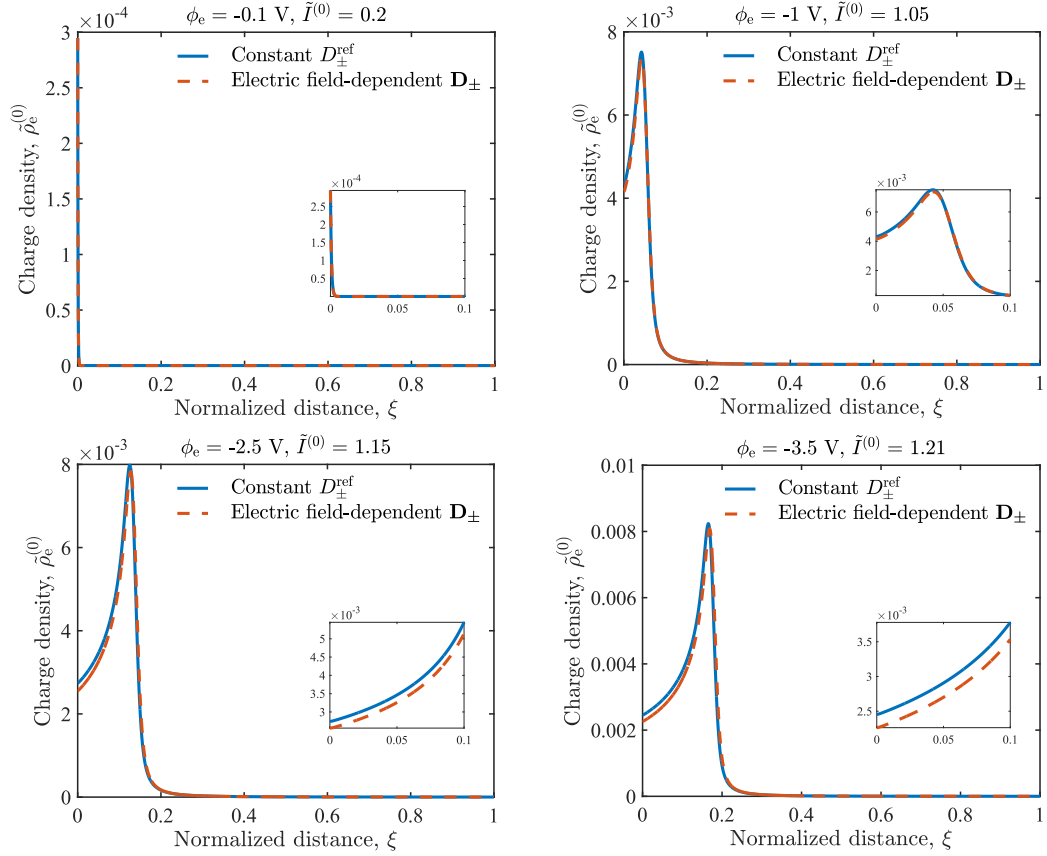
Figure 4.4: Spatial profiles of base-state charge density $\tilde{\rho}_e^{(0)}$ computed with either constant diffusion coefficients $D_\pm^{\text{ref}}$ or electric field-dependent diffusion coefficients $\mathbf{D}_\pm$ in Eq. (A.1), for $L = 0.5$ μm and several values of ϕ_e.

stable, i.e., a small initial perturbation of the surface geometry decays with time, regardless of whether or not the diffusion tensor $\mathbf{D}_\pm$ depends on the electric field $\mathbf{E}$. For larger ϕ_e (overlimiting current, $I^{(0)} > I_{\text{lim}}$), the growth rate $\tilde{w}$ is positive within a certain range of $\tilde{k}$, where the surface growth is unstable and dendrites develop. The dispersion relation $\tilde{w} = \tilde{w}(\tilde{k})$ exhibits non-monotonic behavior: $\tilde{w}$ increases from zero at $\tilde{k} = 0$ to its maximum value of $\tilde{w}_{\text{max}}$ at $\tilde{k}_{\text{max}}$ wherein the electrode surface growth is maximally unstable; further increase of $\tilde{k}$ causes the positive growth rate $\tilde{w}$ to decrease until it reaches 0 at a critical wavenumber $\tilde{k}_{\text{cr}}$ at which point the electrode surface is marginally stable. For $\tilde{k} > \tilde{k}_{\text{cr}}$, the growth rate $\tilde{w}$ becomes negative, and surface energy stabilizes the electrode surface growth. The surface energy term $\text{Ca}\,\tilde{k}^2$

in Eqs. (A.9)–(A.10) comprises the surface curvature $\kappa^{(1)} \propto k^2$ and the surface energy γ. This term has a stabilizing effect on the surface growth at large $\tilde{k}$ by imposing an energy penalty on the creation of additional surface area. The difference between the dispersion relations $\tilde{w} = \tilde{w}(\tilde{k})$ corresponding to constant diffusion coefficients $D_\pm^{\text{ref}}$ and their electric field-dependent anisotropic counterparts $\mathbf{D}_\pm$ increases with ϕ_{e}. For $\phi_{\text{e}} = -3.5$ V, the use of $D_\pm^{\text{ref}}$ instead of $\mathbf{D}_\pm$ would overestimate $\tilde{w}_{\text{max}}$ by 24%, while k_{cr} remains virtually unchanged.
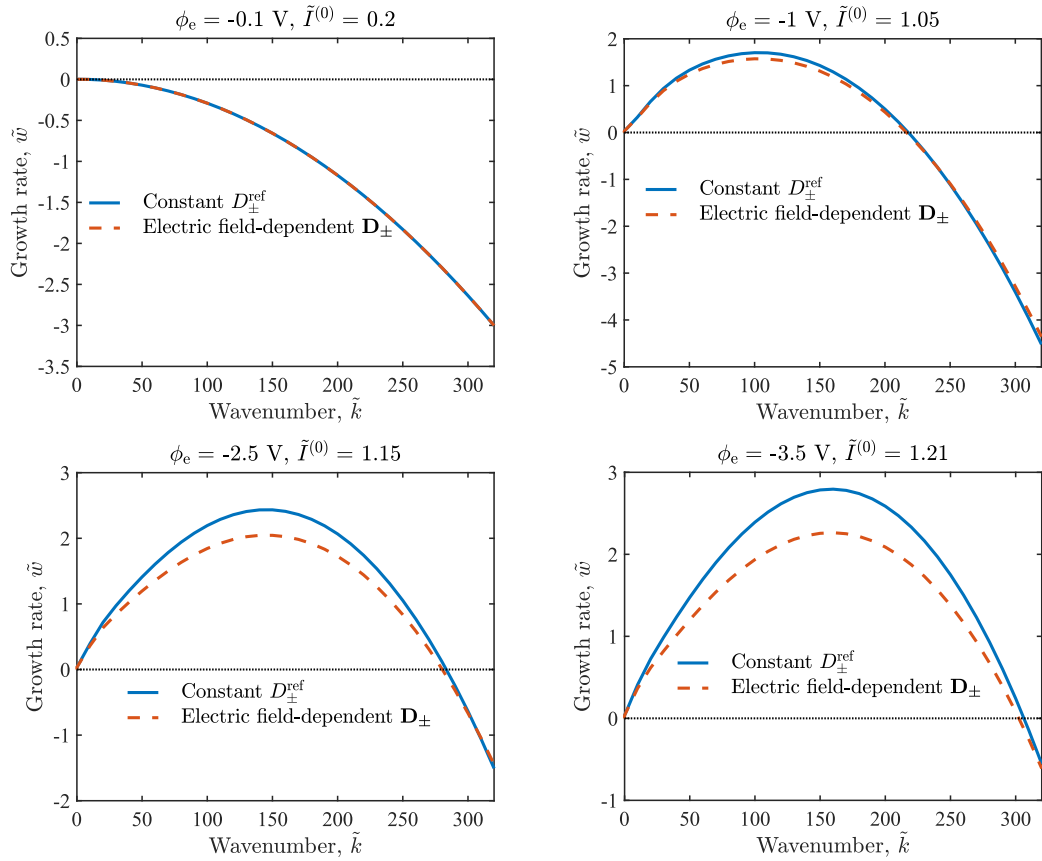
Figure 4.5: Dispersion relations $\tilde{w} = \tilde{w}(\tilde{k})$ computed with either constant diffusion coefficients $D_\pm^{\text{ref}}$ or electric field-dependent diffusion coefficients $\mathbf{D}_\pm$ in Eq. (A.1), for $L = 0.5\ \mu$m and several values of ϕ_{e}.

In another set of numerical experiments, we study how the half-cell length L affects the stability of the electrode interface growth. Figure 4.6 shows the dispersion relations $\tilde{w} = \tilde{w}(\tilde{k})$ corresponding to constant isotropic diffusion coefficients $D_\pm^{\text{ref}}$ and

the electric field-dependent diffusion tensors $\mathbf{D}_\pm$, for $L = 5 \ \mu$m (although not shown here, we have observed the same trend for $L = 50 \ \mu$m). The maximum growth rate $\tilde{w}_{\max}$ increases with L, which is in agreement with the previous study [88]. The impact of the electric field-dependency of the diffusion coefficient on the dispersion relation $\tilde{w} = \tilde{w}(\tilde{k})$ decreases with L. That is because the change in $\tilde{D}_{xx}^\pm$ is confined to the boundary layer adjacent to the electrode, and the width of this layer as a small fraction of the total cell decreases with L (Figure 4.3).
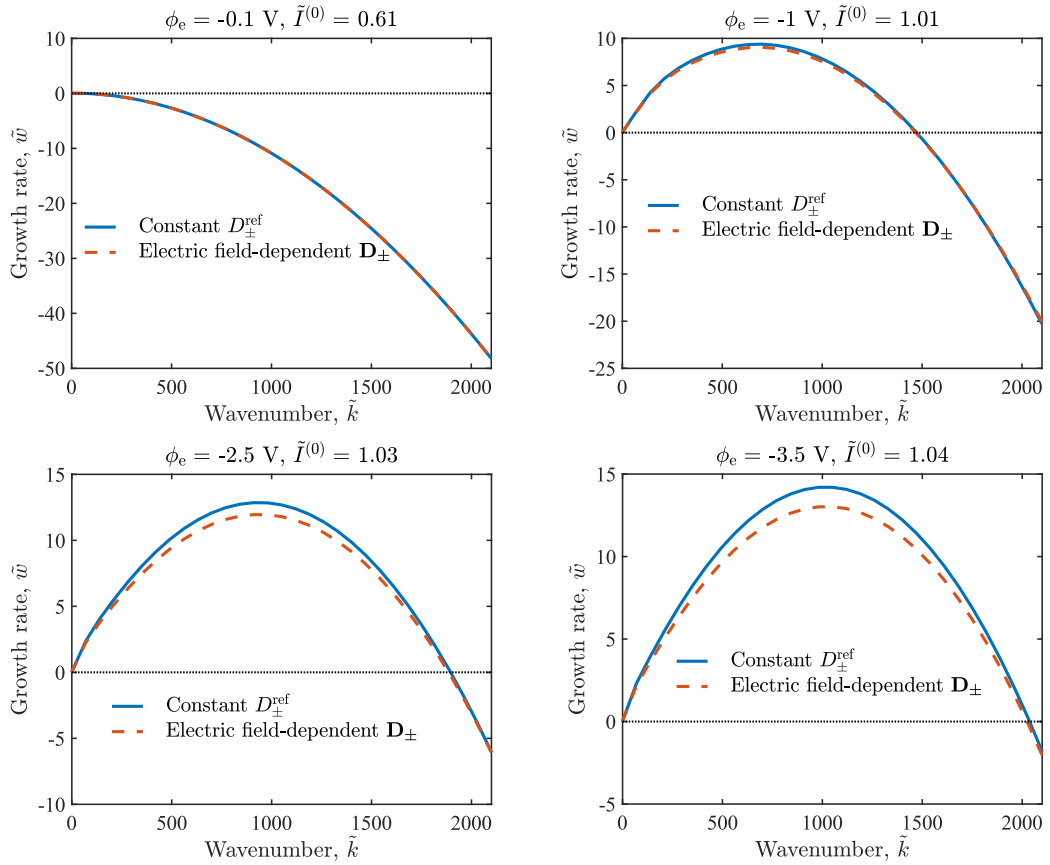
Figure 4.6: Dispersion relations $\tilde{w} = \tilde{w}(\tilde{k})$ computed with either constant diffusion coefficients $D_\pm^{\mathrm{ref}}$ or electric field-dependent diffusion coefficients $\mathbf{D}_\pm$ in Eq. (A.1), for $L = 5 \ \mu$m and several values of ϕ_e.

The local electric field impacts ion diffusion in two ways: it alters the magnitude of the ionic diffusion coefficients and enhances their anisotropic nature. To isolate the contribution of each factor, we conduct two sets of numerical experiments. In

the first, we simulate electrolytes with isotropic diffusion coefficients $D_\pm = D_\pm^{\text{ref}}$; with $D_\pm = 1000D_\pm^{\text{ref}}$; and with the anion diffusivity $D_- = D_-^{\text{ref}}$ and the cation diffusivity $D_+ = 1000D_+^{\text{ref}}$. Although not shown here, we found that modifying D_- has no effect and modifying D_+ has a negligible effect on the dispersion relations in Figures 4.5 and 4.6.

The second set of experiments deals with the stability analysis for electrolytes with constant anisotropic diffusion coefficients,

$$\mathbf{D}_\pm = \begin{pmatrix} D_{xx}^\pm & 0 \\ 0 & D_{yy}^\pm \end{pmatrix}. \tag{4.16}$$

where $D_{xx}^\pm$ and $D_{yy}^\pm$ are the constant diffusion coefficient components in the principal x and y directions. The resulting base-state and perturbed-state equations are derived in the Appendix. We found the anisotropic behavior of the anion diffusion coefficient $\mathbf{D}_-$ to have no impact on the interfacial dynamics, so we only present results for different anisotropy ratios of the cation diffusion coefficient $\mathbf{D}_+$. The use of $\mathbf{D}_\pm$ from Eq. (4.16) rather than from Eq. (4.11) does not change the base-state dynamics, which is governed by Eqs. (A.7) and (A.8). The perturbed-state equations are reported in the Appendix. Figure 4.7 exhibits the dispersion relations $\tilde{w} = \tilde{w}(\tilde{k})$ corresponding to the constant isotropic diffusion coefficients $D_\pm^{\text{ref}}$ and to the constant anisotropic diffusion coefficients $D_{xx}^+ = D_+^{\text{ref}}$, $D_{yy}^- = D_{xx}^- = D_-^{\text{ref}}$ and two values of D_{yy}^+. The maximum growth rate $\tilde{w}_{\max}$ increases by about 70% or 60% when D_{yy}^+ doubles from D_+^{ref} to $2D_+^{\text{ref}}$, for $\phi_e = -3.5$ V and $L = 0.5$ μm or $L = 5$ μm, respectively. Enhancing cation diffusion in the direction parallel to the electrode surface (y) decreases the maximum wavenumber $\tilde{k}_{\max}$, while the critical wavenumber $\tilde{k}_c$ remains unchanged. This finding is in agreement with the numerical simulations of dendrite growth [92]. It is worthwhile contrasting this behavior with that of surface growth in reactive flows [104, 105, 106, 107], in which increasing the transverse component of the diffusion coefficient tensor stabilizes the interface.

Our stability analysis follows the large body of literature [76, 108, 109, 78, 88, 82] in assuming the base state to be stationary. The transient base-state analysis [79] reveals this assumption to have no effect on the dispersion relation $w = w(k)$ when the current

density I is much smaller than the limiting current I_{lim} (Figure 4.8).The importance of the transient base state becomes more pronounced in the over-limiting regime, $I > I_{\text{lim}}$, (see Figure 5 in Ref. 79). However, in this regime the electroneutrality assumption, which underpins the stability analysis in Ref. 79, no longer holds. In a follow-up study, we will extend our analysis to account for the transient base state.
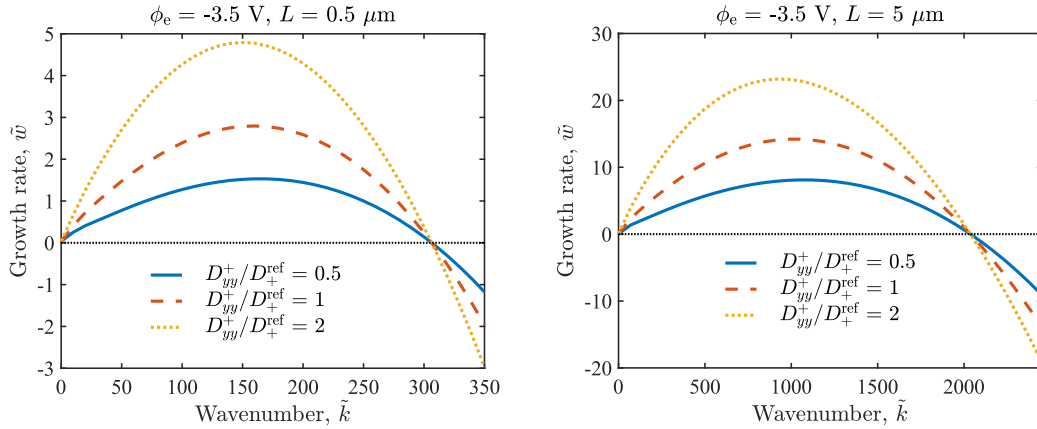
Figure 4.7: Dispersion relations $\tilde{w} = \tilde{w}(\tilde{k})$ computed with either constant isotropic diffusion coefficients $D_{\pm}^{\text{ref}}$ or constant anisotropic diffusion coefficients $D_{xx}^{+} = D_{+}^{\text{ref}}$, $D_{yy}^{-} = D_{xx}^{-} = D_{-}^{\text{ref}}$ and two values of D_{yy}^{+}. Other parameters are set to $\phi_{\text{e}} = -3.5$ V and to either $L = 0.5$ μm or $L = 5$ μm.

4.6 Summary

To identify possible mechanisms for control of dendrite growth in Li-metal batteries, we conducted a linear stability analysis of electrodeposition onto the electrode surface. The analysis employs the Poisson-Nernst-Planck equations coupled with the Butler-Volmer kinetics to describe electrodeposition. we do not invoke the assumption of electroneutrality, which is known to break down in the boundary layer adjacent to the electrode surface. Accounting for gradients in the charge distributions allowed us to investigate the stabilizing effects of electric field-dependent anisotropic diffusion of ions on dendritic growth of Li. Our analysis leads to the following major conclusions.

- Electric field-dependent anisotropic diffusion reduces both charge density close
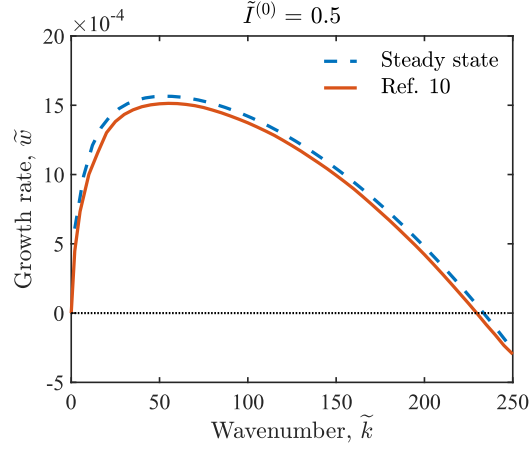
Figure 4.8: Dispersion relations $\tilde{w} = \tilde{w}(\tilde{k})$ alternatively predicted with the steady-state and transient base-state solutions. The latter is obtained by extracting the data from Figure 2 in the Supplementary Material for Ref. 79.

to the electrode surface and the maximum growth rate of dendrites relative to the values of their counterparts for constant isotropic diffusion.

- This effect is most pronounced for large values of the applied electric potential ϕ_e and small half-cell lengths L, e.g., the maximum growth rate is reduced by about 24% when $\phi_e = -3.5$ V and $L = 0.5$ μm. Hence, the impact of electric field on ionic diffusion cannot be ignored for batteries with ultra-thin separators.

- The local electric field affects ion diffusion and the stability of electrodeposition by altering the diffusion coefficient values and by enhancing the degree of anisotropy. An interplay of these two mechanisms can be used to suppress dendritic growth in Li-ion and Li-metal batteries.

Our findings suggest new strategies for the electrolyte design, i.e., for the optimal selection of solvent and salt and for the tuning of the ionic concentration of solution. Such a design would be informed by the degree to which the electric field affects the electrolyte's transport properties and anisotropic behavior and, ultimately, the dendritic growth. An optimal electrolyte (with additives) would exhibit a strong response to the local electric field in a way that increases the cation diffusion coefficient in the direction perpendicular to the electrode surface.

Another design strategy for the suppression of dendrite growth, suggested by our analysis, is to use anisotropic electrolytes, e.g., liquid crystals, liquid-crystalline physical gels etc., or separators with anisotropic pore structures or columnized membranes. As a dendrite suppression strategy, electrolytes with electric field-dependent diffusion coefficients are appropriate for small batteries, while anisotropic electrolytes reduce dendritic growth in batteries of any size.

Although our linear stability analysis reveals the role of key parameters in dendrite initiation, it does not describe subsequent dendritic growth. The latter requires a numerical solution of surface-evolution equations. In follow-up studies, we will model the dynamics of dendritic growth by solving the nonlinear phase-field equations [110, 111] and compare this solution with the predictions of our linear stability analysis. We also plan to compare the advantages and disadvantages of commonly used commercial liquid electrolytes [112] and to investigate the effects of coating on the dendritic growth of the solid electrolyte surface. The former study would require electrolyte-specific experimental data on the dependence of ionic diffusion coefficients on applied electric field, while the latter analysis will be facilitated by an effective-medium representation [15] of the composite solid electrolyte.

Finally, it is worthwhile emphasizing that our analysis ignores several interfacial phenomena on the anode, which are of potential relevance to Li-dendrite initiation and growth. These include Li-solvation/desolvation and their impact on the formation of solid electrolyte interface [113, 114]. Accounting for these processes is another fruitful venue for future research.

Chapter 5

Screening of electrolyte-anode buffers to suppress lithium dendrite growth in all-solid-state batteries

5.1 Abstract

Dendritic growth of lithium (Li) metal is a leading cause of degradation and catastrophic failure of all-solid-state batteries (ASSBs) with Li anode. Insertion of a buffer layer between the Li-metal and the solid electrolyte is known to ameliorate this phenomenon; yet the identification of an optimal buffer material, and the design of ASSBs that can be manufactured at scale, remains elusive and largely driven by trial-and-error experimentation. Our analysis seeks to accelerate the buffer-materials discovery by elucidating the conditions under which the buffer's presence stabilizes electrodeposition on the Li anode in ASSBs. The analysis quantifies the interfacial instability associated with dendrite formation in terms of the battery's operating conditions and the electrochemical and physical properties of the buffer material and solid electrolyte. The model predicts that, among several prospective buffer materials, Ag, Al,

Sn and antiperovskite super ionic conductor, $Li_3S(BF_4)_{0.5}Cl_{0.5}$, are effective in stabilizing electrodeposition and suppressing dendrite growth. Our model's predictions of the dendrite suppression abilities of different buffer materials are consistent with the published experimental findings. The model can be used to guide experimental and computational discovery of new buffer materials that match a particular electrolyte.

5.2 Introduction

All-solid-state lithium-metal batteries (ASSBs) hold the promise of becoming the next-generation safe, high-capacity power source for electric vehicles. In ASSBs, the flammable organic liquid electrolyte currently used in lithium-ion and lithium-metal batteries is replaced with either an organic solid polymer electrolyte or an inorganic solid ceramic/glass electrolyte. Solid ceramic electrolytes, such as the garnet-type $Li_7La_3Zr_2O_{12}$ (LLZO) [115], have attracted a lot of attention due to their superior ionic conductivity, high mechanical strength, and chemical stability with respect to lithium (Li) metal. However, their widespread adoption is impeded by manufacturing challenges and poor electrode/electrolyte interfacial contact. Crucially, formation and growth of Li dendrites are the leading causes of ASSB degradation [116, 117], just as they are for Li-metal batteries.

Proposed strategies for suppression of Li-dendrite growth in ASSBs include use of single-crystal solid ceramic electrolytes, fabrication of pallets with high density and few defects, development of composites combining a solid ceramic electrolyte with a self-healing polymer, and optimization of the Li-metal (Table 1 in Ref. 118). Our study focuses on arresting the Li-dendrite initiation by stabilizing the Li-metal/electrolyte interface [118]. This goal is accomplished by introducing a buffer layer between the Li-metal electrode and the solid ceramic electrolyte. For example, the placement of an aluminium (Al), silicon (Si), germanium (Ge), aluminium oxide (Al_2O_3), lithium nitride (Li_3N), or Li-rich anti-perovskite (Li_3OCl) buffer layer between Li-metal and garnet electrolyte has been shown experimentally to prevent dendrite growth [118]. In the same vein, an electronic-insulating lithium fluoride (LiF) interfacial layer has been shown to facilitate the physical contact between Li-metal and

LLZTO ($Li_{6.4}La_3Zr_{1.4}Ta_{0.6}O_{12}$) electrolyte and promote uniform Li-plating/stripping [119]. The same positive outcome is achieved by either screen-printing silver (Ag) on the garnet electrolyte of an ASSLB [120], or silver-coating the Li-metal surface of a Li-metal battery [121]. Both approaches result in stable Li-plating/stripping profiles at different current densities.

Most of the experimental exploration of potential buffer materials is chemistry-driven and uninformed by quantitative predictions of Li-ion (Li^+) transport and electrochemical transformations in the solid ceramic electrolyte and the buffer. Theoretical and computational work on this subject is scarce [15, 16]. It includes a physics-based model of the electrochemical potential in an ASSB, which accounts for mixed ionic and electronic conduction through the solid electrolyte and buffer layer, but neglects interface resistances and resulting electrode overpotentials [122]. An example of statistical models is a computational screening of over 12,000 inorganic solids, in which machine learning techniques are used to correlate the stability of electrodeposition to various mechanical properties of solid electrolytes [123]. Statistical studies of this kind provide little physical insight that can inform materials or battery design.

We fill this void by presenting a mathematical model of electrodeposition on the Li anode in ASSBs with a buffer layer between the Li anode and the solid ceramic electrolyte. The model describes Li^+ transport in the electrolyte and the buffer, in the presence of an interfacial charge-transfer reaction. We analyze two kinds of buffer material: electronic conductors (e.g., Al and Ag) and electronic insulators (e.g., Al_2O_3, Li_3N, Li_3OCl and LiF); buffers composed of semiconductors (e.g., Si and Ge) are left for future study. Conditions favorable to the onset of dendritic growth or, conversely, to its suppression are established by means of a linear stability analysis of this model.

Our analysis leads to analytical expressions that relate the dendrite growth rate to measurable characteristics such as buffer's thickness and surface morphology, current density, transport properties (Li^+ diffusivity, ionic conductivity) of the electrolyte and the buffer, and the interfacial energy between the Li-metal and the solid electrolyte or buffer layer. This analysis identifies effective buffer materials, which can have

either high electronic conductivity (Ag, Al, and tin Sn) or low electronic conductivity (anti-perovskite, $Li_{2.99}Ba_{0.005}OCl$ [124] and $Li_3S(BF_4)_{0.5}Cl_{0.5}$ [125], both of which are super ionic conductors). Such results provide a useful screening tool to narrow down the space of plausible candidates for an optimal dendrite-suppression buffer material. Ultimate selection of the ideal candidate would be determined by additional factors (e.g., elastic properties and geographic scarcity) absent from our model, such as the mode of a material's application (e.g., coating or construction of a composite) and economic cost.

5.3   Mathematical Formulation

We consider electrodeposition on the Li-metal anode, Ω_{an}, that is separated from the solid electrolyte, Ω_{el}, by the thin buffer layer Ω_b; our model of an ASSB is two-dimensional and deals with the half-cell domain in Figure 5.1. A negative electrostatic potential, φ_e, is maintained on the Li-metal electrode surface, $\Gamma(t)$, at all time t; the electric potential at the outer edge of the electrolyte ($x = L$) is fixed at 0. The Li-metal electrode surface, $\Gamma(t)$, is initially (at time $t = 0$) flat and coincides with the plane $x = 0$, i.e., $\Gamma(0) = \{\mathbf{x} = (x, y)^\top : x = 0,\ 0 \le y \le B\}$.

Temporal evolution of the Li-metal surface $\Gamma(t)$ is a result of electrodeposition that involves a Faradaic reaction between cations (Li^+) and electrons (e^-), $Li^+ + e^- \to Li$, which results in the formation of Li atoms that are subsequently deposited on Γ. Depending on the ratio between the buffer electronic conductivity, σ_{e^-}, and the ionic conductivity for Li^+, σ_{Li^+}, this reaction takes place on either the anode-buffer interface $\Gamma(t)$ or the buffer-electrolyte interface Γ_1 (Figure 5.1). For buffer materials with $\sigma_{e^-} \gg \sigma_{Li^+}$ (Scenario 1), the Faradaic reaction takes place on Γ_1 and the resultant Li atoms are transported to $\Gamma(t)$ by diffusion; for buffer materials with $\sigma_{e^-} \ll \sigma_{Li^+}$ (Scenario 2), the Faradaic reaction occurs on $\Gamma(t)$. We consider both scenarios.

We ignore mechanical effects, e.g., solid electrolyte fracture, rupture of the coated layer, etc., and explore Li diffusion in the buffer layer as a possible dendrite-stabilization mechanism.
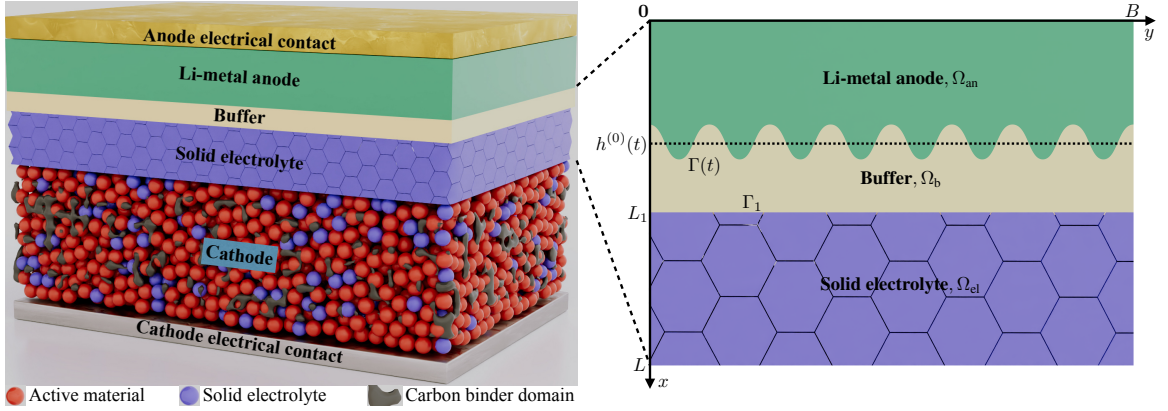
Figure 5.1: Schematic representation of an ASSB (Left) and the two-dimensional half-cell domain considered in this study (Right). The half cell consists of the Li-metal anode, Ω_{an}, that is separated from the solid electrolyte, Ω_{el}, by the buffer layer Ω_{b}. The anode's surface $\Gamma(t)$ evolves with time t due to electrodeposition, while the interface Γ_1 between Ω_{el} and Ω_{b} remains fixed.

5.3.1 Governing equations

We use a two-dimensional Cartesian coordinate system spanned by the orthogonal unit-vectors $\mathbf{e}_x$ and $\mathbf{e}_y$, and represent the anode surface with dendrites, $\Gamma(t)$, by a single-valued function $h(y,t)$ such that $h(y,0) = 0$ (Figure 5.1). The unit-normal vector, $\mathbf{n}(y,t)$, and mean curvature, $\kappa(y,t)$, of the anode surface $\Gamma(t)$ are computed as [17]

$$\mathbf{n} = \frac{1}{\sqrt{1+(\partial_y h)^2}} \begin{pmatrix} -1 \\ \partial_y h \end{pmatrix}, \qquad \kappa = -\frac{1}{2} \frac{\partial_y^2 h}{[1+(\partial_y h)^2]^{3/2}}. \tag{5.1}$$

We analyze the stability of electrodeposition in order to identify the conditions under which a small perturbation of $h(y,t)$ dissipates (rather than grows) with time t.

The rate of change of $\Gamma(t)$ or, equivalently, $h(y,t)$ is given by the normal component of the mass flux of Li atoms, $\mathbf{J}_{\text{Li}}^{\text{b}}(\mathbf{x},t)$ (mol/m²/s), across the buffer/anode interface:

$$\mathbf{e}_x \cdot \mathbf{n} \frac{\partial h}{\partial t} = -\omega \mathbf{n} \cdot \mathbf{J}_{\text{Li}}^{\text{b}}, \qquad \mathbf{x} \in \Gamma(t), \tag{5.2}$$

where ω is the molar volume of Li-metal (m³/mol). The flux $\mathbf{J}_{\text{Li}}^{\text{b}}(\mathbf{x},t)$ is computed from the mass and charge conservation laws for both the buffer and the electrolyte.

Solid electrolyte

The Li cations, Li$^+$, are the only mobile species in the solid electrolyte, $\Omega_{\mathrm{el}} = \{\mathbf{x} : L_1 < x < L, 0 \leq y \leq B\}$. Experimental evidence suggests that these cations are distributed almost uniformly throughout the electrolyte so that their concentration $c_{\mathrm{Li}^+}^{\mathrm{el}}$ is approximately constant and equal to the initial concentration in the electrolyte, $c_{\mathrm{Li}^+}^{\mathrm{el}}(\mathbf{x}, t) \approx c_0$; hence, its gradient is $\nabla c_{\mathrm{Li}^+}^{\mathrm{el}} \approx \mathbf{0}$ and their diffusion flux is negligible. [126, 127] Consequently, in our model, the movement of Li$^+$ is entirely due to electromigration. The Nernst-Planck expression for the Li$^+$ flux in the electrolyte reduces to $\mathbf{J}_{\mathrm{Li}^+}^{\mathrm{el}} = -zFu_{\mathrm{el}}c_0\nabla\varphi_{\mathrm{el}}$, where z is number of proton charges carried by Li$^+$, F is the Faraday constant (s·A/mol), $\varphi_{\mathrm{el}}(\mathbf{x})$ is the electric potential in the electrolyte (V), and u_{el} is the mobility of Li$^+$ in the electrolyte due to the potential gradient $\nabla\varphi_{\mathrm{el}}$. In the absence of an externally imposed magnetic field, the current density $\mathbf{i}_{\mathrm{el}}(\mathbf{x})$ is related to the ionic flux $\mathbf{J}_{\mathrm{Li}^+}^{\mathrm{el}}(\mathbf{x})$ by [126] $\mathbf{i}_{\mathrm{el}} = zF\mathbf{J}_{\mathrm{Li}^+}^{\mathrm{el}}$. This gives rise to Ohm's law and charge conservation in the solid electrolyte, [128, 129]

$$\mathbf{i}_{\mathrm{el}} = -\sigma_{\mathrm{el}}\nabla\varphi_{\mathrm{el}} \quad \text{and} \quad \nabla \cdot \mathbf{i}_{\mathrm{el}} = 0, \qquad \mathbf{x} \in \Omega_{\mathrm{el}}, \tag{5.3}$$

where $\sigma_{\mathrm{el}} = z^2 F^2 u_{\mathrm{el}} c_0$ is the electrolyte's ionic conductivity for Li$^+$ (S/m).

Equations (5.3) are subject to the boundary conditions

$$\varphi_{\mathrm{el}}(L, y) = 0, \qquad \frac{\partial\varphi_{\mathrm{el}}}{\partial y}(x, 0) = \frac{\partial\varphi_{\mathrm{el}}}{\partial y}(x, B) = 0, \tag{5.4}$$

the last two of which represent the electrically insulated vertical surfaces, $y = 0$ and B. The boundary conditions on the electrolyte/buffer interface $\Gamma_1 = \{\mathbf{x} : x = L_1, 0 \leq y \leq B\}$ are determined by the material properties of the buffer, as detailed below.

Buffer layer

The thin buffer, initially of uniform thickness L_1, is represented by the domain $\Omega_{\mathrm{b}}(t) = \{\mathbf{x} : h(y, t) < x < L_1, 0 < y < B\}$. The buffer is characterized by its conductivities for electrons (σ_{e^-}) and Li$^+$ (σ_{Li^+}). We consider two limiting cases defined by the magnitude of the ratio $\sigma_{e^-}/\sigma_{\mathrm{Li}^+}$.

Scenario 1: Buffer with high electronic conductivity. In buffers with $\sigma_{e^-} \gg \sigma_{\mathrm{Li}^+}$ (e.g., Al and Ag), the electron concentration is high and approximately constant throughout the buffer, so that the electric potential in the buffer, φ_{b}, is constant as well. Consequently, the Li$^+$ ions undergo the Faradaic reaction at the buffer/electrolyte interface, $x = L_1$, and reduce to the Li atoms that subsequently diffuse in Ω_{b} and are deposited on the anode surface $\Gamma(t)$. The spatiotemporal evolution of the molar concentration of Li atoms, $c_{\mathrm{Li}}^{\mathrm{b}}(\mathbf{x}, t)$ (mol/m^3), is described by the diffusion equation

$$\frac{\partial c_{\mathrm{Li}}^{\mathrm{b}}}{\partial t} = -\nabla \cdot \mathbf{J}_{\mathrm{Li}}^{\mathrm{b}}, \qquad \mathbf{J}_{\mathrm{Li}}^{\mathrm{b}} = -D_{\mathrm{Li}}^{\mathrm{b}} \nabla c_{\mathrm{Li}}^{\mathrm{b}}, \qquad \mathbf{x} \in \Omega_{\mathrm{b}}, \tag{5.5}$$

where $D_{\mathrm{Li}}^{\mathrm{b}}$ is the diffusion coefficient (m^2/s) for Li in the buffer.

Equation (5.5) is subject to the initial condition

$$c_{\mathrm{Li}}^{\mathrm{b}}(\mathbf{x}, 0) = 0, \qquad \mathbf{x} \in \Omega_{\mathrm{b}}, \tag{5.6}$$

and the boundary conditions on $\Gamma(t)$ and Γ_1. In addition to the kinematic condition in Eq. (5.2), these conditions are

$$\mathbf{n} \cdot \mathbf{J}_{\mathrm{Li}}^{\mathrm{b}} = R_{\Gamma}, \qquad \mathbf{x} \in \Gamma(t), \tag{5.7}$$

and

$$D_{\mathrm{Li}}^{\mathrm{b}} \frac{\partial c_{\mathrm{Li}}^{\mathrm{b}}}{\partial x}(L_1, y, t) = R_{\mathrm{Li}}, \qquad 0 < y < B. \tag{5.8}$$

They encode mass conservation across the interfaces bounding the buffer Ω_{b}. Specifically, Eq. (5.8) specifies that the normal component of $\mathbf{J}_{\mathrm{Li}}^{\mathrm{b}}$ across the buffer/electrolyte interface Γ_1 is proportional to the net reaction rate, R_1, of the Faradaic reaction Li$^+$ + e^- $\rightarrow$ Li; this rate is given by the Butler-Volmer equation,

$$R_{\mathrm{Li}} = -\frac{k_0}{\gamma_{\mathrm{ts}}} \left[a_{\mathrm{R}} \exp\left(\alpha_{\mathrm{an}} \frac{zF\eta_\alpha + 2\omega\gamma_1\kappa}{RT} \right) - a_{\mathrm{O}} a_{\mathrm{e}}^z \exp\left(-\alpha_{\mathrm{cat}} \frac{zF\eta_\alpha + 2\omega\gamma_1\kappa}{RT} \right) \right]. \tag{5.9a}$$

Here, k_0 is the reaction rate constant (mol/m^2/s); R is the universal gas constant (J/mol/K); γ_{ts} is the activity coefficient of the transition state for the Faradaic reaction ($-$); a_{e}, a_{O} and a_{R} are the activities of electrons and oxidant (e.g., Li$^+$) and reductant (e.g., Li atom), respectively; α_{an} and α_{cat} are the anodic and cathodic charge-transfer coefficients, respectively ($-$); γ_1 is the isotropic surface energy at the interface Γ_1 (J/m^2); and the activation overpotential η_α is defined as

$$\eta_\alpha = \varphi_{\text{e}} - \varphi_{\text{b}}(L_1, y, t) - E^{\ominus}, \tag{5.9b}$$

where $E^{\ominus}$ is the standard electrode potential.[1] Since Γ_1 is a straight line, its curvature is $\kappa = 0$. Finally, $a_{\text{R}} = c^{\text{b}}_{\text{Li}}(L_1, y, t)/c^{\ominus}$, where $c^{\ominus}$ is the standard concentration.

By the same token, Eq. (5.7) signifies that the normal mass flux of Li atoms across $\Gamma(t)$, $\mathbf{n} \cdot \mathbf{J}^{\text{b}}_{\text{Li}}$, is supplied by the Li deposition rate, R_Γ. The latter is driven by the difference in the chemical potentials of Li across the Li-metal/buffer interface, for which we adopt the Butler-Volmer form,

$$R_\Gamma = -\frac{k_\Gamma}{\gamma_{\text{ts}}} \left[\exp\left(\alpha_{\text{an}} \frac{2\omega\gamma\kappa - zFE^{\ominus}}{RT} \right) - \frac{c^{\text{b}}_{\text{Li}}(\mathbf{x} \in \Gamma, t)}{c^{\ominus}} \exp\left(-\alpha_{\text{cat}} \frac{2\omega\gamma\kappa - zFE^{\ominus}}{RT} \right) \right], \tag{5.10}$$

where γ is the isotropic surface energy (J/m^2) at the interface Γ. To be specific, we set the reaction rate constant $k_\Gamma = k_0$.

The boundary value problem comprising Eqs. (5.1)–(5.10) requires the knowledge of $c^{\text{b}}_{\text{Li}}(L_1, y, t)$ and $\varphi_{\text{b}}(L_1, y, t) \equiv \varphi(t)$. These boundary functions are computed from the continuity conditions at the interface Γ_1 separating the buffer and the electrolyte. Thus, the normal component of the current density, $\mathbf{i}_{\text{el}} = (i_{\text{el},x}, i_{\text{el},y})^\top$, entering the buffer from the electrolyte at the interface Γ_1 is proportional to the net reaction rate of the Faradaic reaction Li$^+$ + e^- → Li:

$$i_{\text{el},x}(L_1, y, t) = zFR_{\text{Li}}. \tag{5.11}$$

---

[1]In all numerical experiments reported below, we set $\gamma_{\text{ts}} = 1$, $a_{\text{e}} = 1$, $\alpha_{\text{an}} = 1 - \alpha_{\text{cat}}$, and $E^{\ominus} = 0$. We also set $a_{\text{R}} = 1$ and $a_{\text{O}} = 1$ in our simulations of ASSBs without a buffer, i.e., when the Li-metal anode and the solid electrolyte are in direct contact.

That is because, at the flat electrolyte/buffer interface, $J_{\mathrm{Li},x}^{\mathrm{b}} = J_{\mathrm{Li}^+,x}^{\mathrm{b}} = R_{\mathrm{Li}}$.

Scenario 2: Buffer with low electronic conductivity. Buffers with $\sigma_e \ll \sigma_{\mathrm{Li}^+}$ are electronic insulators with high ionic conductivity; examples include i) solid electrolyte materials whose properties differ from those of the solid electrolyte used in a given ASSLB and ii) compositions of the solid electrolyte interface (SEI) formed in an organic liquid electrolyte. Such a buffer, Ω_{b}, acts as a single-ion conductor with a constant Li^+ concentration $c_{\mathrm{Li}^+}^{\mathrm{b}}$. [126, 130, 131] The ions Li^+ undergo the Faradaic reaction, reducing to Li atoms, on the anode surface $\Gamma(t)$.

The spatial distribution of electric potential $\varphi_{\mathrm{b}}(\mathbf{x}, t)$ within the buffer Ω_{b} is governed by the Laplace equation,

$$\nabla \cdot \mathbf{i}_{\mathrm{b}} = 0, \qquad \mathbf{i}_{\mathrm{b}} = -\sigma_{\mathrm{b}} \nabla \varphi_{\mathrm{b}}, \qquad \mathbf{x} \in \Omega_{\mathrm{b}}, \tag{5.12}$$

where σ_{b} is the ionic conductivity for Li^+ in the buffer (S/m), and $\mathbf{i}_{\mathrm{b}}(\mathbf{x}, t)$ is the current density in the buffer (m^2/s). Equations (5.12) are subject to boundary conditions on $\Gamma(t)$ and Γ_1. On the moving surface $\Gamma(t)$, we supplement the kinematic boundary condition in Eq. (5.2) with the mass balance relation

$$\mathbf{n} \cdot \mathbf{i}_{\mathrm{b}} = zFR_{\mathrm{Li}}, \qquad \mathbf{x} \in \Gamma(t). \tag{5.13}$$

The production rate of Li atoms, R_{Li}, is now given by

$$R_{\mathrm{Li}} = -\frac{k_0}{\gamma_{\mathrm{ts}}} \left[\exp\left(\alpha_{\mathrm{an}} \frac{zF\eta_\alpha + 2\omega\gamma_{\mathrm{Li}}^{\mathrm{b}}\kappa}{RT} \right) - \frac{c_{\mathrm{Li}^+}^{\mathrm{b}}}{c^\Theta} \exp\left(-\alpha_{\mathrm{cat}} \frac{zF\eta_\alpha + 2\omega\gamma_{\mathrm{Li}}^{\mathrm{b}}\kappa}{RT} \right) \right]. \tag{5.14}$$

The activation overpotential η_α is now defined as $\eta_\alpha = \varphi_{\mathrm{e}} - \varphi_{\mathrm{b}}(\mathbf{x} \in \Gamma(t), t) - E^\Theta$.

At the buffer/electrolyte interface, Γ_1, we ensure the continuity of electric potential and normal components of the charge flux:

$$\varphi_{\mathrm{b}}(L_1, y) = \varphi_{\mathrm{el}}(L_1, y), \qquad \frac{\partial i_{\mathrm{b},x}}{\partial x}(L_1, y) = \frac{\partial i_{\mathrm{el},x}}{\partial x}(L_1, y). \tag{5.15}$$

In the Butler-Volmer expressions (5.9), (5.10) and (5.14), the surface energy terms

$2\omega\gamma_1\kappa/(RT)$, $2\omega\gamma\kappa/(RT)$ and $2\omega\gamma_{\mathrm{Li}}^{\mathrm{b}}\kappa/(RT)$ are included to account for the effect of the surface curvature on the reactions' energy barrier [76]. They act to flatten the electrode surface, since the creation of additional surface area results in a surface energy penalty. [17]

5.4 Stability Analysis

Linear stability analysis is performed by applying a small perturbation, $\varepsilon\exp(wt + iky)$, to a one-dimensional steady-state base state, defined by the flat electrode surface $h^{(0)}(t) \equiv Ut$ moving with the constant velocity $U = \mathrm{d}h^{(0)}/\mathrm{d}t = -\omega R_{\mathrm{Li}}^{(0)}$ and by the corresponding electric potential $\varphi^{(0)}(x)$ and Li$^+$ concentration $c^{(0)}(x)$. (The spatial profiles of $\varphi^{(0)}$ are shown in Figure B.1 in Appendix A.) Here, ε is the dimensionless small parameter ($\varepsilon \ll L_1/L \ll 1$), w is the growth rate (1/s), k is the wavenumber (1/m), and $i^2 = -1$. The electrodeposition process is unstable if the perturbations grow with time, i.e., if $w > 0$. The goal of a stability analysis is to express w in terms of the physical properties of the solid electrolyte, buffer and the anode.

The mathematical details of this analysis are provided in Appendices A and B. The results are reported below in terms of dimensionless growth rate, wavenumber, and current density,

$$\tilde{w} = \frac{wF^2c_0L^2}{\sigma_{\mathrm{el}}RT}, \quad \tilde{k} = kL, \quad \text{and} \quad \tilde{I} = \frac{LFI}{zRT\sigma_{\mathrm{el}}} = \frac{\tilde{R}_{\mathrm{Li}}}{z}. \tag{5.16}$$

5.5 Results and Discussion

The parameter values used in our stability analysis are presented in Table 5.1. For illustration purposes, we choose lithium lanthanum zirconium oxide (Li$_7$La$_3$Zr$_2$O$_{12}$, LLZO) as the solid electrolyte. To ensure that the standard electrode potential, E^Θ is 0 for Scenarios 1 and 2, we define the standard concentration c^Θ to be either the Li concentration in the lithium metal, $c^\Theta = c_{\mathrm{Li}}$, in Scenario 1 or the Li$^+$ concentration in the solid electrolyte, $c^\Theta = c_0$, in Scenario 2.

Table 5.1:   Model parameters used in the stability analysis.

Parameter	Value	Ref
Half-cell length, L (μm)	10	132
Buffer layer thickness, L_1 (nm)	20	
Ionic conductivity for Li$^+$ in solid electrolyte, σ_{el} (S/m)	0.1	133
Temperature, T (K)	298.15	
Molecular weight of lithium metal, M (g/mol)	6.941	100
Density of lithium metal, ρ (g/cm^3)	0.534	100
Li concentration in lithium metal, c_{Li} (mol/m^3)	76,934	100
Concentration of Li$^+$ in solid electrolyte, c_0 (mol/m^3)	18,012	117
Standard concentration, c^Θ (mol/m^3)	c_{Li}, c_0	
Standard electrode potential, E^Θ (V)	0	
Reaction rate constant, k_0 (mol/(m^{2}s))	$1 \cdot 10^{-2}$	134
Surface energy of Li/LLZO interface, $\gamma_{Li/el}$ (J/m^2)	0.85	135
Activity coefficient of the transition state, γ_{ts} (-)	1	

Figures 5.2 and 5.3 exhibit the dispersion relations, $\tilde{w} = \tilde{w}(\tilde{k})$, and the corresponding stability regimes for ASSBs with and without a buffer. Only the results for high-conductivity buffers (Scenario 1) are shown. That is because their counterparts for low-conductivity buffers (Scenario 2) overlap with the solutions in the absence of a buffer when $\sigma_b/\sigma_{el} = 1$, according to Eq. (B.30). These results are obtained by solving the boundary-value problems in Appendix A numerically and, under certain approximations, analytically (Appendix B). Figure 5.2 demonstrates that the numerical and analytical solutions are virtually indistinguishable; thus, the subsequent figures display only analytical results. In Figure 5.2, the range of wavenumbers $\tilde{k}$ corresponding to the positive growth rate $\tilde{w}$ identifies the conditions under which the surface growth is unstable and dendrites develop; the maximum value $\tilde{w}_{max} = \tilde{w}(\tilde{k}_{max})$ indicates the regime wherein the electrode surface growth is maximally unstable, while the regime with $\tilde{k}_{cr}$ corresponds to the marginally stable electrode surface. Both $\tilde{w}_{max}$ and $\tilde{k}_{cr}$ increase with the applied potential φ_e. When $\tilde{k} > \tilde{k}_{cr}$, the surface is stable because $\tilde{w} < 0$ due to the surface energy penalty on the creation of additional surface area. This penalty is quantified by the terms proportional to capillary numbers for the electrolyte and buffer, Ca_{Li}^{el} and Ca_{Li}^{b}, in Eqs. (B.25) and (B.28).

In the absence of a buffer, the growth rate $\tilde{w}$ is maximal at $\tilde{k} = 0$ as the electric
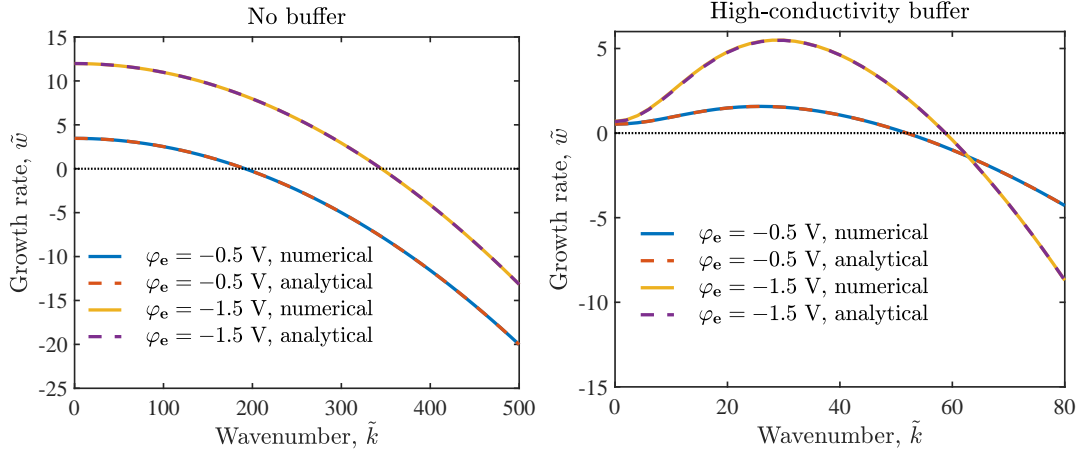
Figure 5.2: Dispersion relations $\tilde{w} = \tilde{w}(\tilde{k})$ for ASSBs without a buffer and with the high-conductivity buffer ($\tilde{D}_{\rm b} = 1$ and $Ca_{\rm Li}^{\rm el} = Ca_{\rm Li}^{\rm b}$), for $\varphi_{\rm e}$= -0.5 V and -1.5 V. The solid and dashed lines are the numerical and analytical solutions, respectively.

potential gradient always acts as a destabilization source and no stabilization mechanism is involved (Figure 5.2). That is in contrast to the high-conductivity buffer, for which the dispersion relation $\tilde{w} = \tilde{w}(\tilde{k})$ is non-monotonic: $\tilde{w}$ increases from a small positive value at $\tilde{k} = 0$ to its maximum value $\tilde{w}_{\max}$, after which it decreases and eventually becomes negative. Diffusion of Li in the buffer has a stabilizing effect by reducing the growth rate $\tilde{w}$ at all wavenumbers $\tilde{k}$. A proper selection of the transport properties of the buffer material ($\tilde{D}_{\rm b}$ and $Ca_{\rm Li}^{\rm b}/Ca_{\rm Li}^{\rm el}$) would allow one to reduce both the maximal growth rate $\tilde{w}_{\max}$ and the critical wavenumber $\tilde{k}_{\rm cr}$, i.e., to extend the operational range over which the electrodeposition on the Li anode remains stable.

The stability of electrodeposition, encapsulated in the dispersion relation $\tilde{w} = \tilde{w}(\tilde{k})$, depends on both the materials properties and the battery operating conditions (the applied electric potential $\varphi_{\rm e}$ or the current density I). Figure 5.3 identifies the stability regimes, $\tilde{w} = \tilde{w}(\tilde{k}; \tilde{I}^{(0)})$ given by Eqs. (B.30) and (B.25), for ASSBs without a buffer and with a highly conductive buffer, respectively. Defining the critical wavenumber $\tilde{k}_{\rm cr}$ as the wavenumber at which $w = 0$, yields the curve $\tilde{I}^{(0)} = \tilde{I}^{(0)}(\tilde{k}_{\rm cr})$ that separates the stable ($w < 0$) and unstable ($w > 0$) regimes. The presence of a high-conductivity buffer (with $\tilde{D}_{\rm b} = 1$ and $Ca_{\rm Li}^{\rm b} = Ca_{\rm Li}^{\rm el}$) significantly expands the stability of electrodeposition at any current density, i.e., the size of the blue region
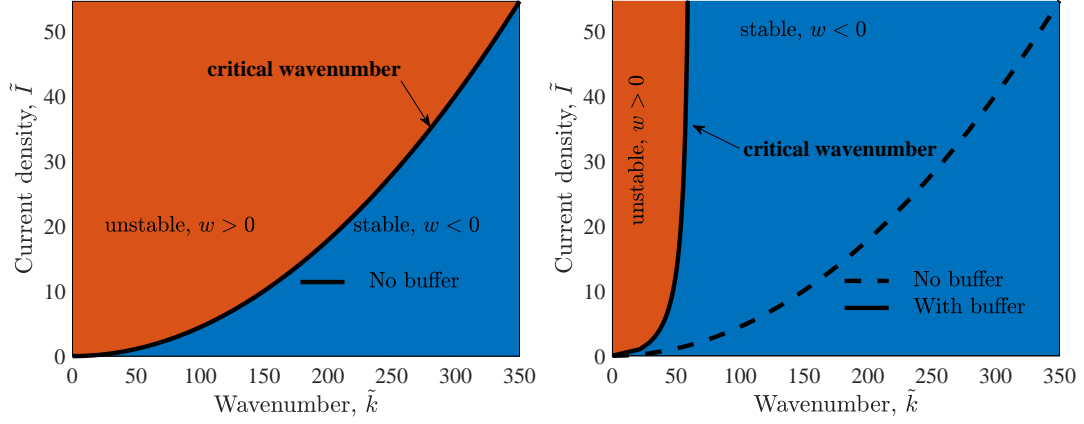
Figure 5.3: Stability regimes predicted by Eqs. (B.30) and (B.25) for ASSBs without a buffer (Left) and with a high-conductivity buffer ($\tilde{D}_b = 1$ and $Ca_{Li}^b = Ca_{Li}^{el}$) (Right). The solid/dashed lines denote the critical wavenumber $\tilde{k}_{cr}$ for each current density $\tilde{I}^{(0)}$; these lines, along which $w = 0$, separate the stable ($w < 0$, blue) and unstable ($w > 0$, red) regions.

in which $w < 0$. In the absence of a buffer, Li deposition becomes progressively unstable as I increases. The stability diagrams in Figure 5.3 provide a blueprint for the electrode-morphology design: they suggest that deploying Li-metal anodes whose surface roughness wavelength λ is smaller than the critical wavelength $\lambda_{cr} = 2\pi/\tilde{k}_{cr}$ would ameliorate dendritic growth. Such surfaces can be manufactured with, e.g., nano-structuring. [136]

Table 5.2: Transport properties and interfacial energies for buffer materials with high electronic conductivity at room temperature, $T = 298.15$ K.

Property	Ag		Al		Sn	
	Value	Ref	Value	Ref	Value	Ref
Li diffusion coefficient, D_b (m^2/s)	$1 \cdot 10^{-10}$	137	$8.43 \cdot 10^{-12}$	138	$4.15 \cdot 10^{-12}$	139
Dimensionless Li diffusivity, $\tilde{D}_b$	67.64		5.71		2.81	
Interfacial energy, γ_{Li}^b (J/m^2)	1.36	140	1.28	140	0.93	140
Ratio Ca_{Li}^b/Ca_{Li}^{el}	1.6		1.5		1.1	
Electronic conductivity, σ_e (S/m)	$6.67 \cdot 10^7$	141	$4.08 \cdot 10^7$	141	$8.7 \cdot 10^6$	141
Dimensionless e^- conductivity, $\tilde{\sigma}_e$	$6.67 \cdot 10^8$		$4.08 \cdot 10^8$		$8.7 \cdot 10^7$	

Dependence of the dispersion relations $\tilde{w} = \tilde{w}(\tilde{k})$ on the electrochemical characteristics of the electrolyte and buffer suggests the use of these relations as a screening

tool for materials selection. To this end, we investigate three metal materials as candidates for a highly conductive buffer: silver (Ag), aluminum (Al) and tin (Sn). Their transport properties (Li diffusivity, electronic conductivity) and interfacial energies at room temperature, $T = 298.15$ K are collated in Table 5.2. The Li-metal/buffer interfacial energies are computed as [142] $\gamma_{Li}^b = \gamma_{Li} + \gamma_b - 0.5\sqrt{\gamma_{Li}\gamma_b}$, where γ_{Li} and γ_b are the surface energies of Li and coating materials reported in Ref. 140. The dimensionless electronic conductivity $\tilde{\sigma}_e$ of these metals is at least seven orders of magnitude larger than the dimensionless Li diffusivity, $\tilde{D}_b$. Thus, the assumption of high and constant electron concentration in the buffer is valid, and the Faradaic reaction $Li^+ + e^- \rightarrow Li$ takes place at the buffer/electrolyte interface. The dispersion relations $\tilde{w} = \tilde{w}(\tilde{k})$ for Ag, Al and Sn buffers at φ_e = -1.5 V are shown in Figure 5.4. The use of Ag as a buffer material yields the negative growth rate $\tilde{w}$ for wavenumber $\tilde{k}$ that is slightly larger than 0. For Al and Sn buffers, $\tilde{w}$ is positive for small $\tilde{k}$ and negative for a wide range of $\tilde{k} > \tilde{k}_{cr}$. All three buffer materials dramatically expand the stable regime relative to that of an ASSB without a buffer. Our results confirm the experimental findings [120, 121] according to which the use of Ag buffers mitigates dendritic growth because the dimensionless diffusivity of Li in Ag is larger than the dimensionless Li^+ conductivity in the solid electrolyte. Another reason is that the interfacial energy between Ag and Li-metal is higher than that between the solid electrolyte and Li-metal. While somewhat less efficient in dendrite suppression, Al and Sn are plausible buffer materials, especially considering their lower cost.

Table 5.3: Transport properties and interfacial energies for coating materials with low electronic conductivity at room temperature, $T = 298.15$ K.

Property	$Li_3S(BF_4)_{0.5}Cl_{0.5}$ Value	Ref	$Li_{2.99}Ba_{0.005}OCl$ Value	Ref
Ionic conductivity for Li^+, σ_b (S/m)	10	125	1	124
Dimensionless Li^+ conductivity, $\tilde{\sigma}_b$	100		10	
Li^+ concentration, c_{Li}^b (mol/m^3)	26,629	125	93,531	124
Dimensionless Li^+ concentration, $\tilde{c}_{Li}^b$	1.45		5.19	
Interfacial energy, γ_b^{Li} (J/m^2)	0.65	143	0.65	143
Ratio Ca_{Li}^b/Ca_{Li}^{el}	0.76		0.76	
Electronic conductivity, σ_e (S/m)	negligible	125	negligible	124
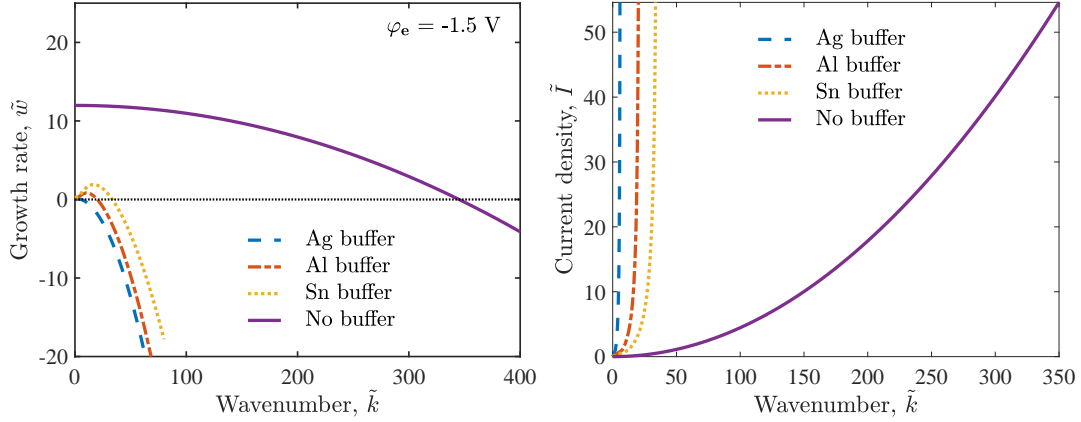
Figure 5.4: Dispersion relations $\tilde{w} = \tilde{w}(\tilde{k})$ at $\varphi_e = -1.5$ V (Left) and stability regimes $\tilde{w} = \tilde{w}(\tilde{k}; \tilde{I}^{(0)})$ (Right), for ASSBs without a buffer and with Ag, Al and Sn buffers. The lines in the right graph, along which $w = 0$ and $\tilde{k} = \tilde{k}_{cr}$, separate the stable $(w < 0)$ and unstable $(w > 0)$ regions.

Next, we apply our analysis to buffer materials with low electronic conductivity, specifically, two antiperovskite super ionic conductors, $Li_{2.99}Ba_{0.005}OCl$ [124] and $Li_3S(BF_4)_{0.5}Cl_{0.5}$ [125]. Table 5.3 reports their ionic conductivity and interfacial energy at room temperature, $T = 298.15$ K; in the absence of the interfacial energies for electrolyte/buffer systems, we use the interfacial energy of an antiperovskite super ionic conductor, Li_3OCl [143]. For both materials, the dimensionless electronic conductivity $\tilde{\sigma}_e$ is many orders of magnitude smaller than the dimensionless Li^+ conductivity and, thus, Li^+ ions undergo the Faradaic reaction with e^- and reduce to Li atoms at the anode/buffer interface, $x = L_1$. Figure 5.5 suggests that buffers made of materials with low electronic conductivity and ionic conductivity for Li^+ higher than that in the solid electrolyte (LLZO), such as the antiperovskite super ionic conductors, $Li_3S(BF_4)_{0.5}Cl_{0.5}$ and $Li_{2.99}Ba_{0.005}OCl$, suppress dendrite growth.

One might expect the buffer thickness, L_1, to affect the buffer's ability to suppress dendrite growth and, thus, to act as another design variable. According to Eqs. (B.26) and (B.29), at any given current density $I^{(0)}$, the critical wavenumber k_{cr} is independent of L_1, regardless of whether the buffer has high or low electronic conductivity. However, L_1 does impact the maximum growth rate w_{max}, with the nonlinear dependence of the growth rate on the buffer thickness, $w = w(L_1)$, given by Eq. (B.25)
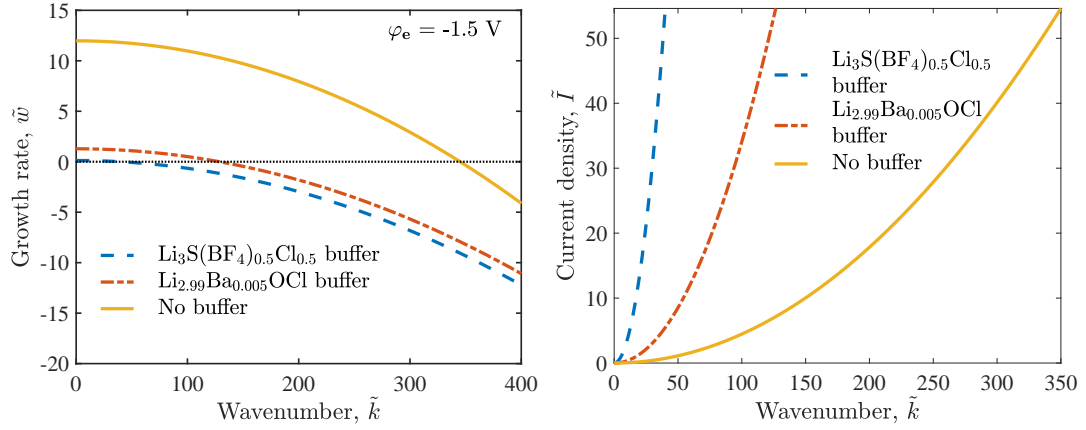
Figure 5.5: Dispersion relations $\tilde{w} = \tilde{w}(\tilde{k})$ at $\varphi_e = -1.5$ V (Left) and stability regimes $\tilde{w} = \tilde{w}(\tilde{k}; \tilde{I}^{(0)})$ (Right), for ASSBs without a buffer and with the $Li_3S(BF_4)_{0.5}Cl_{0.5}$ and $Li_{2.99}Ba_{0.005}OCl$ buffers. The lines in the right graph, along which $w = 0$ and $\tilde{k} = \tilde{k}_{cr}$, separate the stable ($w < 0$) and unstable ($w > 0$) regions.

for buffers with high electronic conductivity and by Eq. (B.28) for low-conductivity buffers. These equations point to the complex interplay between the buffer's size and transport properties. For example, according to Eq. (B.28), w decreases or increases with L_1 depending on whether $\sigma_b > \sigma_{el}$ or $\sigma_b < \sigma_{el}$.

Finally, we validate our analysis by comparing its predictions with the previously published experiments. This task proved to be challenging because many experimental studies do not report all the relevant material properties and even fewer studies report negative results. With these caveats, all the experimental results we are aware of conform to our stability diagrams (Figure 5.6). For buffer materials with high electronic conductivity and positive interfacial energies, $\gamma_{Li}^{el} > 0$ and $\gamma_{Li}^{b} > 0$, the stability diagram is presented in the $(Ca_{Li}^b \tilde{D}_b / Ca_{Li}^{el}, \tilde{I})$ phase space. For low-conductivity buffers with $\gamma_{Li}^{el} > 0$ and $\gamma_{Li}^{b} > 0$, the phase space is spanned by the material properties $\tilde{\sigma}_b$ and Ca_{Li}^b / Ca_{Li}^{el}. In both cases, the solid line represents critical wavenumbers $\tilde{k}_{cr}$ for ASSBs without a buffer, such that the insertion of a buffer with given material properties is predicted to have either destabilizing (red region to the left of the solid line) or stabilizing (blue region to the right of the solid line) effect on the Li dendrites. Using the same material properties and operating conditions as in the experiments [120, 144, 145, 146], our model confirms that high-conductivity buffers
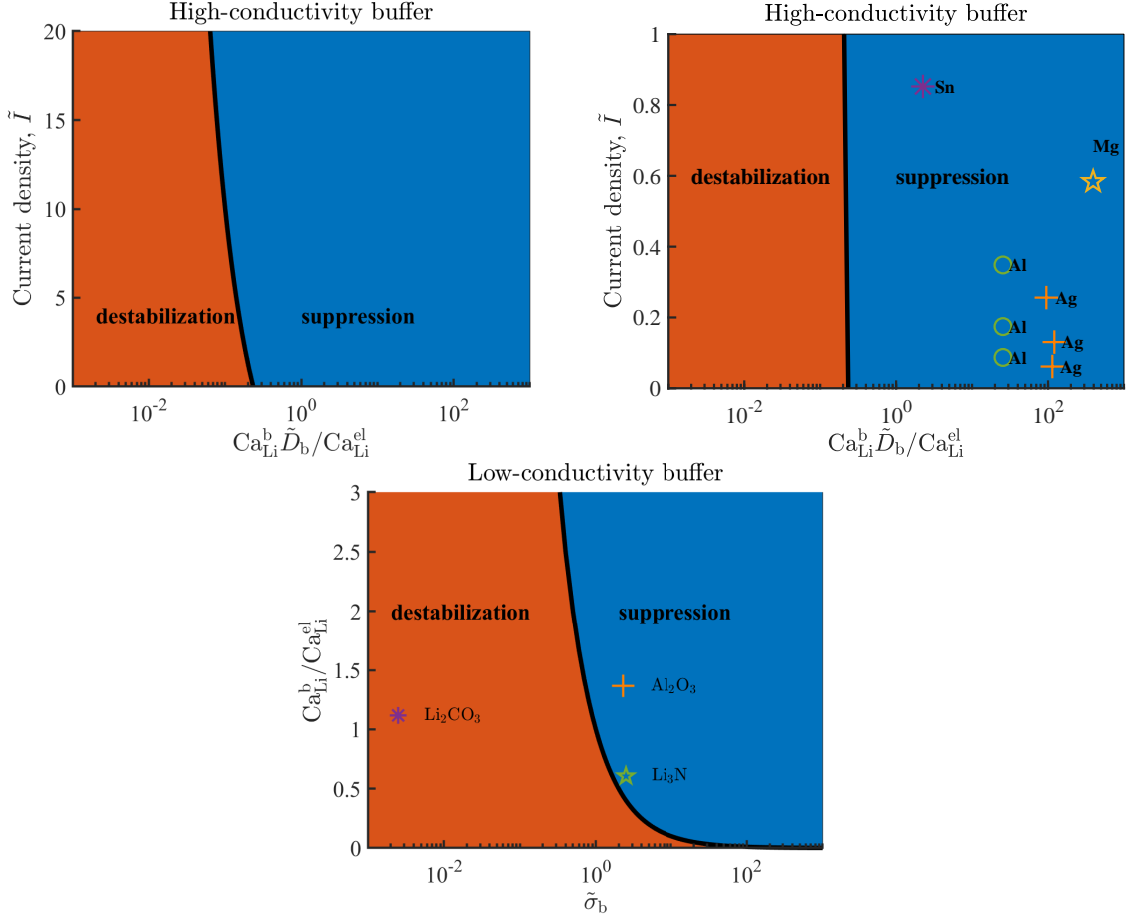
Figure 5.6: Stability diagrams in the phase space spanned by dimensionless parameters $(\mathrm{Ca}_{\mathrm{Li}}^{\mathrm{b}} \tilde{D}_{\mathrm{b}}/\mathrm{Ca}_{\mathrm{Li}}^{\mathrm{el}}, \tilde{I})$ and $(\tilde{\sigma}_{\mathrm{b}}, \mathrm{Ca}_{\mathrm{Li}}^{\mathrm{b}}/\mathrm{Ca}_{\mathrm{Li}}^{\mathrm{el}})$ for buffer materials with high and low electronic conductivity, respectively. In both cases, the interfacial energies are positive, $\gamma_{\mathrm{Li}}^{\mathrm{el}} > 0$ and $\gamma_{\mathrm{Li}}^{\mathrm{b}} > 0$. The solid line represents critical wavenumbers $\tilde{k}_{\mathrm{cr}}$ for ASSBs without a buffer, such that the insertion of a buffer with given material properties is predicted to have either destabilizing (red region to the left of the solid line) or stabilizing (blue region to the right of the solid line) effect on the Li dendrites. The experimental data for Ag, Al, Sn, Mg, Al$_2$O$_3$, Li$_3$N, and Li$_2$CO$_3$ are from Refs. 120, 144, 145, 146, 147, 148.

made of Ag, Al, Sn or magnesium (Mg) suppress dendrite growth. For buffers with low electronic conductivity, our model predictions are consistent with the experimental results [147, 148] that Al_2O_3 and Li_3N stabilize the electrodeposition on the Li anode, while lithium carbonate (Li_2CO_3) fails to suppress dendrite growth due to its relatively low ionic conductivity and interfacial energy with Li-metal.

The stability diagrams in Figure 5.6 do not include buffers and solid electrolytes that have negative interfacial energies with Li-metal, $\gamma_{Li}^{el} < 0$ and/or $\gamma_{Li}^{b} < 0$. That is because, according to our predictions based on Eqs. B.25 and B.28, negative values of the capillary numbers Ca_{Li}^{el} or Ca_{Li}^{b} always yield positive growth rate w, which signifies that the electrode surface growth is unconditionally unstable. This conclusion is in line with the experimental study [149], which found $\gamma_{Li}^{el} < 0$ to indicate an intrinsically unstable interface between the solid electrolyte (e.g., LPS) and the Li-metal, and suggested the potential dendrite suppression abilities of buffer materials with $\gamma_{Li}^{el} > 0$.

5.6 Summary

The insertion of a buffer layer between the Li-metal anode and the solid (ceramic) electrolyte has been proposed as a possible strategy to suppress Li dendrite formation in ASSBs. We investigated this possibility by presenting a mathematical model of electrodeposition on the Li anode of ASSBs with and without such a buffer layer, with focus on the stability of the evolving anode surface in response to a small perturbation. Our key result is analytical expressions that relate the instability growth-rate to both material properties (transport properties of the electrolyte and buffer and interfacial energy) and battery operating conditions (current density or applied electric potential). Our analysis leads to the following major conclusions.

- Our stability diagrams correctly identify buffer materials that are experimentally shown to suppress/mitigate dendrite growth in ASSBs. These materials can have either high (e.g., Ag, Al, Sn, Mg) or low (e.g., Al_2O_3 and Li_3N) electronic conductivity, provided they have positive interfacial energy.

- Our analysis correctly identifies buffer materials that, in experiments, failed to

impact dendrite growth. These materials have either low ionic conductivity and interfacial energy with Li-metal (e.g., Li_2CO_3) or have negative interfacial energy with Li-metal (e.g., LPS).

- Our stability diagrams suggest that prospective buffer materials should have either high electronic conductivity and high Li diffusion coefficient or low electronic conductivity and high ionic conductivity for Li^+; materials with high interfacial energy with Li-metal are preferred.

- Candidates for buffer materials with low electronic conductivity include antiperovskite super ionic conductors, $Li_{2.99}Ba_{0.005}OCl$ and $Li_3S(BF_4)_{0.5}Cl_{0.5}$, because of their Li diffusivity is higher than that of most currently proposed solid electrolytes.

- Our analysis demonstrates that the buffer thickness has no impact on the critical surface roughness wavelength, below which the interface is stable and no dendrites initiate.

Our findings suggest new strategies for the design of interfacial buffers, i.e., for the optimal selection of buffer material and the solid electrolyte pair based on their electrochemical and physical properties. Our model enables a quantitative evaluation of the buffer materials and, when combined with experimental and computational approaches that provide improved characterization of the material properties, would accelerate the discovery of new buffer materials.

In future work, we will extend our model to handle buffer materials with intermediate electronic and ionic conductivities and couple ion transport and mechanical behaviors in ASSBs. We will also investigate the effects of operating conditions and aging on dendrite suppression by changing the ionic conductivity and Li concentration in the solid electrolyte or buffer materials.

Finally, our analysis points to the possibility of using Li-metal anodes with randomly rough surfaces as a means to suppress or mitigate dendrite initiation. Such a strategy has proved to be beneficial in other applications, e.g., Ref. 150; its mathematical treatment would necessitate the adoption of a probabilistic framework. [151, 152]

Chapter 6

Concluding Remarks

This dissertation has centered on tackling various challenges related to high-energy-density batteries through the utilization of mathematical modeling and numerical techniques, including homogenization, multi-scale simulations, and linear stability analysis, etc. These approaches have significantly enhanced our comprehension of the complex electrochemical processes and transport phenomena occurring in energy storage systems.

The modeling framework developed in this dissertation will enhance the accuracy of performance predictions for batteries and provides valuable guidance for battery design and material selection. The modeling of porous cathodes has yielded important insights, summarized as follows:

- Effective Transport Model of Composite Electrode: Our effective transport model has provided a quantitative assessment of the impact of carbon binder domain on the overall ionic transport in a composite electrode. This model conserves mass and charge and resulted in semi-analytical expressions for equivalent ionic conductivity, diffusion coefficient, and other relevant parameters.

- Improved Parameterizations for Pseudo-2-Dimensional (P2D) Models: Our novel parameterizations of P2D models have exhibited enhanced prediction accuracy for lithiation curves in Li-metal batteries, surpassing the currently employed parameterizations, particularly in the context of fast charging scenarios.

By establishing the connection between micro-scale electrochemical transport phenomena and overall cell performance through multiscale parameterization of porous cathodes, this dissertation has offered valuable insights for the optimal design of composite electrodes. Furthermore, our investigations on the Li-metal anode side have focused on addressing battery safety concerns associated with dendrite growth. The following implications have emerged for the design of high-energy batteries with Li anodes:

- In Li-Metal Batteries: Our findings propose new strategies for electrolyte design, including the optimal selection of solvent and salt, as well as tuning the ionic concentration of the solution. Additionally, we suggest the use of separators with anisotropic pore structures or columnized membranes, which can effectively suppress Li dendrite growth in Li-metal batteries.

- In All-Solid-State Batteries: Our findings suggest new strategies for the design of interfacial buffers, i.e., for the optimal selection of buffer material and the solid electrolyte pair based on their electrochemical and physical properties in all-solid-state batteries. This analysis serves as a useful screening tool to narrow down the space of plausible candidates for an optimal dendrite-suppression buffer material.

The mathematical models developed in this work enable quantitative evaluations of battery materials. When combined with experimental and computational approaches that provide improved characterization of material properties, these models can accelerate the discovery of new electrolytes, separators, and interfacial buffer materials between Li-metal anodes and electrolytes.

By providing these key findings, this dissertation has advanced our knowledge and understanding of the electrochemical processes and transport phenomena in high-energy-density batteries. The developed modeling framework and derived insights hold great potential for guiding future advancements in battery design and optimization, ultimately leading to more efficient and reliable energy storage systems. For future work, the architecture of this modeling framework may be enriched to include the following.

i) Reflecting the pore-scale structure of composite porous electrodes and the morphological changes (both in terms of pore size and pore accessibility) occurring during the battery operational life as a result of dissolution and depositional kinetics; process and integrate high-resolution tomographic images, to keep up with rapidly improving computerized tomography (CT) technology offering increasingly accurate insights into pore-scale geometry;

ii) Accounting for three-dimensional effects occurring locally (particle scale) and at the larger scale (material heterogeneity, pairing between electrode and current collectors), and dynamically evolving alongside thermal and mechanical stresses;

iii) Incorporating thermal and mechanical stresses inducing changes in both micro- and macro-structure, and electro-chemistry;

iv) Modeling degradation mechanisms such as side reactions and dissolution and deposition reactive dynamics;

v) Integrating a pore-level multi-scale method to accelerate numerical simulations and use a probabilistic model of the porescale heterogeneity and translating it to a probabilistic continuum finite volume model.

Appendix A

Linear stability analysis of dendritic growth in lithium-metal batteries

Let $\hat{\varepsilon} = \varepsilon \exp(wt + iky)$. Then, accounting for Eq. (4.14), a Taylor expansion of $\mathbf{D}_\pm$ in Eq. (4.11) is

$$\mathbf{D}_\pm = D_\pm^{\text{ref}} \begin{pmatrix} e^{b_\pm j_\phi^{(0)}} & 0 \\ 0 & 1 \end{pmatrix} + \hat{\varepsilon} D_\pm^{\text{ref}} b_\pm \begin{pmatrix} e^{b_\pm j_\phi^{(0)}} \partial_x \phi^{(1)} & 0 \\ 0 & ik\phi^{(1)} \end{pmatrix} + \mathcal{O}(\varepsilon^2)\mathbf{I}, \qquad (A.1)$$

where $j_\phi^{(0)} = \partial_x \phi^{(0)}$, and $\mathbf{I}$ is the 2×2 identity matrix. Substituting Eqs. (4.14), (4.15) and (A.1) into the dimensionless form of Eqs. (4.1) and (4.2), and collecting the terms of order ε^0 and ε leads to the zeroth-order equations,

$$\frac{dJ_\pm^{(0)}}{dx} = 0, \quad J_\pm^{(0)} = -D_\pm^{\text{ref}} e^{b_\pm j_\phi^{(0)}} \left(\frac{dc_\pm^{(0)}}{dx} + z_\pm c_\pm^{(0)} j_\phi^{(0)} \right), \quad -\frac{d^2\phi^{(0)}}{dx^2} = \frac{z_+ c_+^{(0)} + z_- c_-^{(0)}}{2\lambda_D^2};$$

$$(A.2)$$

and the first-order equations,

$$-\frac{\mathrm{d}}{\mathrm{d}x}\left(J_{\pm}^{(1)} + b_{\pm}J_{\pm}^{(0)}\frac{\mathrm{d}\phi^{(1)}}{\mathrm{d}x}\right) = \left(w + D_{\pm}^{\mathrm{ref}}k^2\right)c_{\pm}^{(1)} + D_{\pm}^{\mathrm{ref}}k^2 z_{\pm}c_{\pm}^{(0)}\phi^{(1)}, \tag{A.3a}$$

$$-\frac{\mathrm{d}^2\phi^{(1)}}{\mathrm{d}x^2} + k^2\phi^{(1)} = \frac{z_+c_+^{(1)} + z_-c_-^{(1)}}{2\lambda_D^2}, \tag{A.3b}$$

$$J_{\pm}^{(1)} = -D_{\pm}^{\mathrm{ref}}\mathrm{e}^{b_{\pm}j_{\phi}^{(0)}}\left(\frac{\mathrm{d}c_{\pm}^{(1)}}{\mathrm{d}x} + z_{\pm}c_{\pm}^{(1)}j_{\phi}^{(0)} + z_{\pm}c_{\pm}^{(0)}\frac{\mathrm{d}\phi^{(1)}}{\mathrm{d}x}\right). \tag{A.3c}$$

It follows from Eq. (A.2) that $J_{\pm}^{0} = \mathrm{const.}$ Hence, Eq. (A.3a) is transformed into

$$-\frac{\mathrm{d}J_{\pm}^{(1)}}{\mathrm{d}x} - b_{\pm}J_{\pm}^{(0)}\frac{\mathrm{d}^2\phi^{(1)}}{\mathrm{d}x^2} = \left(w + D_{\pm}^{\mathrm{ref}}k^2\right)c_{\pm}^{(1)} + D_{\pm}^{\mathrm{ref}}k^2 z_{\pm}c_{\pm}^{(0)}\phi^{(1)}. \tag{A.4}$$

The derivation of the boundary conditions on the evolving electrode surface $\Gamma(t)$, whose points are represented as $(y, h(y, t))^{\top}$, requires one to approximate $\phi(\mathbf{x} \in \Gamma, t)$, $c_{\pm}(\mathbf{x} \in \Gamma, t)$ and their gradients. That is accomplished by expanding these quantities in Taylor series around the base state $\Gamma^{(0)} = \{\mathbf{x} = (x, y)^{\top} : x = h^{(0)}, 0 \le y \le B/L\}$ such that

$$\phi(\mathbf{x} \in \Gamma, t) \approx \phi^{(0)}(h^{(0)}) + \hat{\varepsilon}\hat{\phi}, \qquad \hat{\phi}^{(1)} = \left(h^{(1)}\frac{\mathrm{d}\phi^{(0)}}{\mathrm{d}x} + \phi^{(1)}\right)_{x=h^{(0)}}; \tag{A.5a}$$

$$c_{\pm}(\mathbf{x} \in \Gamma, t) \approx c_{\pm}^{(0)}(h^{(0)}) + \hat{\varepsilon}\hat{c}_{\pm}, \qquad \hat{c}_{\pm}^{(1)} = \left(h^{(1)}\frac{\mathrm{d}c_{\pm}^{(0)}}{\mathrm{d}x} + c_{\pm}^{(1)}\right)_{x=h^{(0)}}; \tag{A.5b}$$

and

$$\nabla\phi(\mathbf{x}\in\Gamma,t)\approx\mathbf{e}_x\left[\frac{\mathrm{d}\phi^{(0)}}{\mathrm{d}x}(h^{(0)})+\hat{\varepsilon}\left(h^{(1)}\frac{\mathrm{d}^2\phi^{(0)}}{\mathrm{d}x^2}+\frac{\mathrm{d}\phi^{(1)}}{\mathrm{d}x}\right)_{x=h^{(0)}}\right]+\mathbf{e}_y\hat{\varepsilon}ik\phi^{(1)}(h^{(0)});$$

(A.5c)

$$\nabla c_\pm(\mathbf{x}\in\Gamma,t)\approx\mathbf{e}_x\left[\frac{\mathrm{d}c_\pm^{(0)}}{\mathrm{d}x}(h^{(0)})+\hat{\varepsilon}\left(h^{(1)}\frac{\mathrm{d}^2c_\pm^{(0)}}{\mathrm{d}x^2}+\frac{\mathrm{d}c_\pm^{(1)}}{\mathrm{d}x}\right)_{x=h^{(0)}}\right]+\mathbf{e}_y\hat{\varepsilon}ikc_\pm^{(1)}(h^{(0)}).$$

(A.5d)

The function $h^{(0)}(t)$ and the constant $h^{(1)}$ are first defined in Eqs. (4.12) and (4.13), respectively. It follows from Eq. (4.8) that first-order approximations of the unit normal vector $\mathbf{n}=\mathbf{n}^{(0)}+\mathcal{O}(\varepsilon^2)$ and the curvature are, respectively, $\kappa=\kappa^{(0)}+\hat{\varepsilon}\kappa^{(1)}$, with the components

$$\mathbf{n}^{(0)}=\begin{pmatrix}-1\\0\end{pmatrix},\qquad\kappa^{(0)}=0,\qquad\kappa^{(1)}=\frac{k^2}{2}h^{(1)}.$$

(A.6)

Hence, a first-order approximation of the reaction rate R_{Li} in Eq. (4.12c), has the components $R_{\mathrm{Li}}^{(0)}$ and $R_{\mathrm{Li}}^{(0)}$ given by Eqs. (A.8c) and (A.10c). The current density I is expanded to first order, $I=I^{(0)}+\hat{\varepsilon}I^{(1)}$, with $I^{(0)}=zR^{(0)}$ and $J^{(1)}=zR^{(1)}$.

The interface $h^{(0)}(t)$ is moving with velocity $U=\mathrm{d}h^{(0)}/\mathrm{d}t$. It follows from Eq. (4.9) that this velocity is given by $U=-\omega R_{\mathrm{Li}}^{(0)}$. We introduce the moving coordinate system associated with the electrode-electrolyte interface, $(\xi\equiv x-Ut,y)$. Rewriting Eqs. (A.1)–(A.6) in this coordinate system yields the following zeroth- and first-order boundary-value problems (BVPs).

A.1 Base-state BVP

The base-state dependent variables $c_\pm^{(0)}(\xi)$ and $\phi^{(0)}(\xi)$ satisfy the one-dimensional steady-state Poisson-Nernst-Planck equations:

$$\frac{\mathrm{d}J_\pm^{(0)}}{\mathrm{d}\xi}=0,\qquad-\frac{\mathrm{d}^2\phi^{(0)}}{\mathrm{d}\xi^2}=\frac{z_+c_+^{(0)}+z_-c_-^{(0)}}{2\lambda_D^2},\qquad0<\xi<1,$$

(A.7a)

where

$$J_\pm^{(0)} = -D_\pm^{\text{ref}} e^{b_\pm j_\phi^{(0)}} \left(\frac{dc_\pm^{(0)}}{d\xi} + z_\pm j_\phi^{(0)} c_\pm^{(0)} \right), \qquad j_\phi^{(0)} \equiv \frac{d\phi^{(0)}}{d\xi}. \tag{A.7b}$$

Equations (A.7) are subject to the boundary conditions at the non-perturbed anode-surface, $\xi = 0$,

$$\frac{dc_+^{(0)}}{d\xi} = 0, \qquad -J_+^{(0)} = R_{\text{Li}}^{(0)}, \qquad \frac{dc_-^{(0)}}{d\xi} + z_- c_-^{(0)} j_\phi^{(0)} = 0; \tag{A.8a}$$

and at the outer surface of the electrolyte, $\xi = 1$,

$$\phi^{(0)}(1) = 0, \qquad c_+^{(0)}(1) = 1, \qquad c_-^{(0)}(1) = 1. \tag{A.8b}$$

In (A.8a),

$$R_{\text{Li}}^{(0)} = -k_0 e^{-\alpha_{\text{cat}} z \eta_\alpha^{(0)}} \left(e^{z \eta_\alpha^{(0)}} - c_+^{(0)}/c_+^\Theta \right), \qquad \eta_\alpha^{(0)} = \phi_\text{e} - \phi^{(0)} - E^\Theta. \tag{A.8c}$$

A.2 Perturbed-state BVP

The perturbed-state variables $c_\pm^{(1)}(\xi)$ and $\phi^{(1)}(\xi)$ satisfy the one-dimensional differential equations

$$-\frac{dJ_\pm^{(1)}}{d\xi} - b_\pm J_\pm^{(0)} \frac{d^2\phi^{(1)}}{d\xi^2} = \left(w + D_\pm^{\text{ref}} k^2 \right) c_\pm^{(1)} + D_\pm^{\text{ref}} k^2 z_\pm c_\pm^{(0)} \phi^{(1)}, \tag{A.9a}$$

$$-\frac{d^2\phi^{(1)}}{d\xi^2} + k^2 \phi^{(1)} = \frac{z_+ c_+^{(1)} + z_- c_-^{(1)}}{2\lambda_D^2}, \tag{A.9b}$$

$$J_\pm^{(1)} = -D_\pm^{\text{ref}} e^{b_\pm j_\phi^{(0)}} \left(\frac{dc_\pm^{(1)}}{d\xi} + z_\pm c_\pm^{(1)} j_\phi^{(0)} + z_\pm c_\pm^{(0)} \frac{d\phi^{(1)}}{d\xi} \right). \tag{A.9c}$$

Equations (A.9) are subject to the boundary conditions at $\xi = 0$,

$$wh^{(1)} = \omega c_0 R_{\text{Li}}^{(1)}, \qquad \frac{\mathrm{d}\hat{c}_+^{(1)}}{\mathrm{d}\xi} = 0, \qquad \hat{J}_-^{(1)} = 0, \qquad -\hat{J}_+^{(1)} = R_{\text{Li}}^{(1)}, \qquad \text{(A.10a)}$$

and at $\xi = 1$,

$$\phi^{(1)}(1) = 0, \qquad c_+^{(1)}(1) = 0, \qquad c_-^{(1)}(1) = 0. \qquad \text{(A.10b)}$$

In these conditions, which are obtained as first-order approximations of Eqs. (4.3)–(4.10),

$$R_{\text{Li}}^{(1)} = k_0 \mathrm{e}^{-\alpha_{\text{cat}} z \eta_\alpha^{(0)}} \left\{ \frac{\hat{c}_+^{(1)}}{c_+^\Theta} + \left[(1 - \alpha_{\text{cat}})\mathrm{e}^{z\eta_\alpha^{(0)}} + \alpha_{\text{cat}} \frac{\hat{c}_+^{(0)}}{c_+^\Theta} \right] (z\hat{\phi}^{(1)} - \text{Ca}k^2 h^{(1)}) \right\}, \quad \text{(A.10c)}$$

$$\hat{J}_\pm^{(1)} = -D_\pm^{\text{ref}} \mathrm{e}^{b_\pm j_\phi^{(0)}} \left(\frac{\mathrm{d}\hat{c}_\pm^{(1)}}{\mathrm{d}\xi} + z_\pm c_\pm^{(1)} j_\phi^{(0)} + z_\pm c_\pm^{(0)} \frac{\mathrm{d}\hat{\phi}^{(1)}}{\mathrm{d}\xi} \right), \qquad \text{(A.10d)}$$

where

$$\hat{\phi}^{(1)} = h^{(1)} \frac{\mathrm{d}\phi^{(0)}}{\mathrm{d}\xi} + \phi^{(1)}, \qquad \hat{c}_\pm^{(1)} = h^{(1)} \frac{\mathrm{d}c_\pm^{(0)}}{\mathrm{d}\xi} + c_\pm^{(1)}. \qquad \text{(A.10e)}$$

A.3   Perturbed-state BVP for anisotropic constant diffusion

Another problem of practical significance involves anisotropic electrolytes in which the diffusion coefficient tensor in Eq. (4.11) is replaced with Eq. (4.16). The procedure used above yields the base-state dynamics described by Eqs. (A.7) and (A.8) with $D_\pm^{\text{ref}} = D_{xx}^\pm$ and $b_\pm = 0$. It also leads to the perturbed-state equations

$$\frac{\mathrm{d}J_\pm^{(1)}}{\mathrm{d}\xi} + wc_\pm^{(1)} + k^2 D_{yy}^\pm (c_\pm^{(1)} + z_\pm c_\pm^{(0)} \phi^{(1)}) = 0, \qquad \text{(A.11)}$$

$$-\frac{\mathrm{d}^2\phi^{(1)}}{\mathrm{d}\xi^2} + k^2\phi^{(1)} = \frac{z_+c_+^{(1)} + z_-c_-^{(1)}}{2\lambda_D^2}, \qquad J_\pm^{(1)} = -D_{xx}^\pm\left[\frac{\mathrm{d}c_\pm^{(1)}}{\mathrm{d}\xi} + z_\pm\left(c_\pm^{(1)}j_\phi^{(0)} + c_\pm^0\frac{\mathrm{d}\phi^{(1)}}{\mathrm{d}\xi}\right)\right]$$

$$(\text{A.12})$$

and the boundary conditions at $\xi = 0$

$$h^{(1)}\frac{\mathrm{d}J_-^{(0)}}{\mathrm{d}\xi} + J_-^{(1)} = 0, \quad h^{(1)}\frac{\mathrm{d}J_+^{(0)}}{\mathrm{d}\xi} + J_+^{(1)} = -R_{\text{Li}}^{(1)}, \quad \frac{\mathrm{d}\hat{c}_+^{(1)}}{\mathrm{d}\xi} = 0, \quad wh^{(1)} = \omega c_0 R_{\text{Li}}^{(1)};$$

$$(\text{A.13})$$

and at $\xi = 1$

$$\phi^{(1)} = 0, \qquad c_\pm^{(1)} = 0. \tag{A.14}$$

Here, $J_\pm^{(0)}$ and $\hat{c}_+^{(1)}$ are defined by Eq. (A.7b) with $D_\pm^{\text{ref}} = D_{xx}^\pm$ and $b_\pm = 0$ and by Eq. (A.10e), respectively.

Appendix B

Linear stability analysis of dendritic growth in all-solid-state batteries

B.1 Perturbation Analysis

We introduce dimensionless variables

$$\tilde{x} = \frac{x}{L}, \quad \tilde{y} = \frac{y}{L}, \quad \tilde{t} = \frac{t\sigma_{\text{el}}RT}{F^2 c_0 L^2}, \quad \tilde{c} = \frac{c}{c_0}, \quad \tilde{\varphi} = \frac{F\varphi}{RT}, \quad \tilde{h} = \frac{h}{L}, \quad \tilde{\kappa} = L\kappa \quad \text{(B.1a)}$$

and model parameters

$$\tilde{\sigma} = \frac{\sigma}{\sigma_{\text{el}}}, \quad \tilde{D}_{\text{b}} = \frac{D_{\text{b}}F^2 c_0}{\sigma_{\text{el}}RT}, \quad \tilde{c}^{\Theta} = \frac{c^{\Theta}}{c_0}, \quad \tilde{k}_0 = \frac{LF^2 k_0}{RT\sigma_{\text{el}}\gamma_{\text{ts}}}, \quad \tilde{\eta}_{\alpha} = \frac{F\eta_{\alpha}}{RT}. \quad \text{(B.1b)}$$

We also define the capillary numbers

$$\text{Ca}_{\text{Li}}^{\text{el}} = \frac{\omega\gamma_{\text{Li}}^{\text{el}}}{RTL}, \quad \text{Ca}_{\text{Li}}^{\text{b}} = \frac{\omega\gamma_{\text{Li}}^{\text{b}}}{RTL} \quad \text{(B.1c)}$$

and the normalized rate of Li production $\tilde{R}_{\mathrm{Li}}$ and the interfacial current density $\tilde{I}$ as

$$\tilde{R}_{\mathrm{Li}} = \frac{LF^2 R_{\mathrm{Li}}}{RT\sigma_{\mathrm{el}}}, \quad \tilde{I} = \frac{LFI}{zRT\sigma_{\mathrm{el}}} = \frac{\tilde{R}_{\mathrm{Li}}}{z}. \tag{B.1d}$$

Unless specified otherwise, all the quantities below are dimensionless, even though we drop the tildes to simplify the notation.

The electrode surface height, $h(y,t)$, and the state variables $\varphi(\mathbf{x},t)$ and $c(\mathbf{x},t)$ are written as

$$h = h^{(0)}(t) + \hat{\varepsilon}h^{(1)}, \quad \varphi = \varphi^{(0)}(x) + \hat{\varepsilon}\varphi^{(1)}, \quad c = c^{(0)}(x) + \hat{\varepsilon}c^{(1)}, \quad \hat{\varepsilon} = \varepsilon e^{wt+iky}, \tag{B.2}$$

where the constant $h^{(1)}$ and the functions $\varphi^{(1)}(x)$ and $c^{(1)}(x)$ are first-order (in ε) corrections to the base state denoted by the superscript $^{(0)}$. The evolving electrode surface $\Gamma(t)$, which consists of points $(y, h(y,t))^\top$, is a perturbation around the base state $\Gamma^{(0)} = \{\mathbf{x} = (x,y)^\top : x = h^{(0)}, 0 \leq y \leq B/L\}$. It follows from Eq. (5.1) that first-order approximations of its unit normal vector, $\mathbf{n} = \mathbf{n}^{(0)} + \mathcal{O}(\varepsilon^2)$, and curvature, $\kappa = \kappa^{(0)} + \hat{\varepsilon}\kappa^{(1)}$, are given by

$$\mathbf{n}^{(0)} = \begin{pmatrix} -1 \\ 0 \end{pmatrix}, \qquad \kappa^{(0)} = 0, \qquad \kappa^{(1)} = \frac{k^2}{2}h^{(1)}. \tag{B.3}$$

It follows from Eq. (5.2) that the interface $h^{(0)}(t)$ is moving with velocity $U = \mathrm{d}h^{(0)}/\mathrm{d}t$. Depending on the buffer type, this velocity is given by either $U = -\omega R_\Gamma^{(0)}$ (Eq. 5.7, Scenario 1) or $U = -\omega R_{\mathrm{Li}}^{(0)}$ (Eq. 5.13, Scenario 2).

In this formulation, the buffer is represented by the domain $\tilde{\Omega}_{\mathrm{b}}^{(0)} = \{\tilde{x} : \tilde{h}^{(0)}(t) < \tilde{x} < \tilde{L}_1\}$ and the solid electrolyte by the domain $\tilde{\Omega}_{\mathrm{el}}^{(0)} = \{\tilde{x} : \tilde{L}_1 < \tilde{x} < 1\}$, where $\tilde{L}_1 = L_1/L$. As mentioned above, we drop the tilde to simplify the notation.

B.1.1 Solid electrolyte

Substituting Eq. (B.2) into the dimensionless form of Eqs. (5.3) and (5.4), and collecting the terms of order ε^0 and ε leads to the PDEs for $\varphi_{\mathrm{el}}^{(n)}(x)$,

$$\frac{\mathrm{d}i_{\mathrm{el}}^{(n)}}{\mathrm{d}x} = 0, \quad i_{\mathrm{el}}^{(n)} = -\sigma_{\mathrm{el}}\frac{\mathrm{d}\varphi_{\mathrm{el}}^{(i)}}{\mathrm{d}x}, \quad n = 0, 1, \quad L_1 < x < 1, \tag{B.4}$$

where $i_{\mathrm{el}} = |\mathbf{i}_{\mathrm{el}}|$ and $\mathbf{i}_{\mathrm{el}}^{(n)} = (i_{\mathrm{el}}^{(n)}, 0)^\top$ for $n = 0, 1$. These two equations are subject to the boundary conditions $\varphi_{\mathrm{el}}^{(n)}(1) = 0$ and the continuity conditions at the electrolyte/buffer interface $x = L_1$. Integrating these equations once yields

$$i_{\mathrm{el}}^{(n)} = -\sigma_{\mathrm{el}}\frac{\mathrm{d}\varphi_{\mathrm{el}}^{(i)}}{\mathrm{d}x} = a_n, \quad \varphi_{\mathrm{el}}^{(n)}(1) = 0, \quad n = 0, 1. \tag{B.5}$$

The constants of integration a_0 and a_1 are determined from the interfacial conditions at $x = L_1$. These conditions depend on the type of buffer material. In Scenario 1, this condition follows from Eqs. (5.11) and (B.1d),

$$i_{\mathrm{el}}^{(n)}(L_1) = I_{\mathrm{Li}}^{(n)}, \quad n = 0, 1, \tag{B.6}$$

which specifies these constants as $a_n = I_{\mathrm{Li}}^{(n)}$ for $n = 0, 1$. In Scenario 2, this condition is provided by Eq. (5.15),

$$\varphi_{\mathrm{el}}^{(n)}(L_1) = \varphi_{\mathrm{b}}^{(n)}(L_1), \quad n = 0, 1. \tag{B.7}$$

In accordance with Eq. (5.14), the interfacial current density depends on the electric potential in the buffer, $I_{\mathrm{Li}} = I_{\mathrm{Li}}(\varphi_{\mathrm{b}})$. Hence, in either scenario, the electric potentials in the electrolyte and the buffer are coupled in any approximation order n.

B.1.2 Scenario 1: High-conductivity buffer

Substituting Eq. (B.2) into the dimensionless form of Eqs. (5.5)–(5.8), and collecting the terms of order ε^0 and ε leads to the BVPs for $c^{(n)}(x)$ used in the approximation

of the Li concentration in the buffer, $c_{\mathrm{Li}}^{\mathrm{b}}(\mathbf{x}, t) \approx c^{(0)}(x) + \hat{\varepsilon}(y, t)c^{(1)}(x)$:

$$J^{(n)} = -D_{\mathrm{b}}\frac{\mathrm{d}c^{(n)}}{\mathrm{d}x}, \qquad \frac{\mathrm{d}^2 c^{(n)}}{\mathrm{d}x^2} = \begin{cases} 0 & n = 0 \\ (w/D_{\mathrm{b}} + k^2)c^{(1)} & n = 1 \end{cases}, \qquad h^{(0)} < x < L_1,$$

(B.8)

subject to the boundary conditions (B.6) and

$$-J^{(n)} = R_\Gamma^{(n)} \quad \text{at } x = h^{(0)}, \qquad -J^{(n)} = R_{\mathrm{Li}}^{(n)} \quad \text{at } x = L_1. \tag{B.9}$$

In these BVPs, according to Eqs. (5.9) and (5.10),

$$R_\Gamma^{(n)} = -k_0 e^{-\alpha_{\mathrm{cat}} z \eta_\alpha^{(0)}} \begin{cases} \dfrac{c^{(0)}}{c^\Theta} e^{z\eta_\alpha^{(0)}} - 1 & n = 0 \\ \dfrac{c^{(1)}}{c^\Theta} e^{z\eta_\alpha^{(0)}} & n = 1 \end{cases} \tag{B.10}$$

and

$$R_{\mathrm{Li}}^{(n)} = k_0 \begin{cases} \dfrac{c^{(0)}}{c^\Theta} - 1 & n = 0 \\ k^2(1 - \alpha_{\mathrm{cat}} + \dfrac{c^{(0)}}{c^\Theta}\alpha_{\mathrm{cat}})h^{(1)}\mathrm{Ca}_{\mathrm{Li}}^{\mathrm{b}} - h^{(1)}\dfrac{\hat{c}^{(1)}}{c^\Theta} & n = 1, \end{cases} \tag{B.11}$$

where $\eta_\alpha^{(0)} = \varphi_{\mathrm{e}} - \varphi_{\mathrm{b}}^{(0)} - E^\Theta$. It follows from Eqs. (5.2), (B.2) and (B.3) that

$$wh^{(1)} = \omega c_0 R_{\mathrm{Li}}^{(1)} \quad \text{and} \quad \hat{c}^{(1)} = h^{(1)}\frac{\mathrm{d}c^{(0)}}{\mathrm{d}x} + c^{(1)}. \tag{B.12}$$

The derivation of the boundary condition on the evolving electrode surface $\Gamma(t)$, whose points are represented as $(y, h(y, t))^\top$, requires us to expand $c_{\mathrm{Li}}^{\mathrm{b}}(\mathbf{x} \in \Gamma, t)$ and its gradient in Taylor series around the base state $\Gamma^{(0)} = \{\mathbf{x} = (x, y)^\top : x = h^{(0)}, 0 \leq y \leq B/L\}$ such that

$$c_{\mathrm{Li}}^{\mathrm{b}}(\mathbf{x} \in \Gamma, t)(\mathbf{x} \in \Gamma, t) \approx c^{(0)}(h^{(0)}) + \hat{\varepsilon}\hat{c}^{(1)}(h^{(0)}) \tag{B.13a}$$

and

$$\nabla c_{\mathrm{Li}}^{\mathrm{b}} \approx \mathbf{e}_x \left[\frac{\mathrm{d}c^{(0)}}{\mathrm{d}x}(h^{(0)}) + \hat{\varepsilon}\left(h^{(1)}\frac{\mathrm{d}^2 c^{(0)}}{\mathrm{d}x^2} + \frac{\mathrm{d}c^{(1)}}{\mathrm{d}x} \right)_{x=h^{(0)}} \right] + \mathbf{e}_y \hat{\varepsilon} i k c^{(1)}(h^{(0)}). \qquad \text{(B.13b)}$$

B.1.3 Scenario 2: Low-conductivity buffer

Substituting Eq. (B.2) into the dimensionless form of Eqs. (5.12)–(5.14), and collecting the terms of order ε^0 and ε leads to the BVPs for $\varphi_{\mathrm{b}}^{(n)}(x)$:

$$i_{\mathrm{b}}^{(n)} = -\sigma_{\mathrm{b}}\frac{\mathrm{d}\varphi_{\mathrm{b}}^{(n)}}{\mathrm{d}x}, \qquad \frac{\mathrm{d}i_{\mathrm{b}}^{(n)}}{\mathrm{d}x} = 0, \qquad n = 0,1; \qquad h^{(0)} < x < L_1, \qquad \text{(B.14)}$$

subject to boundary conditions (B.7) and

$$-i_{\mathrm{b}}^{(n)}(h^{(0)}) = R_{\mathrm{Li}}^{(n)}(h^{(0)}), \qquad i_{\mathrm{b}}^{(n)}(L_1) = i_{\mathrm{el}}^{(n)}(L_1), \qquad n = 0,1. \qquad \text{(B.15)}$$

Here, $w h^{(1)} = \omega c_0 R_{\mathrm{Li}}^{(1)}$ and

$$R_{\mathrm{Li}}^{(n)} = -k_0 e^{-\alpha_{\mathrm{cat}} z \eta_\alpha^{(0)}} \begin{cases} e^{z\eta_\alpha^{(0)}} - \dfrac{c_{\mathrm{Li}}^{\mathrm{b}}}{c^{\Theta}} & n = 0 \\[2ex] \left[(1-\alpha_{\mathrm{cat}})e^{z\eta_\alpha^{(0)}} + \alpha_{\mathrm{cat}}\dfrac{c_{\mathrm{Li}}^{\mathrm{b}}}{c^{\Theta}} \right](k^2 \mathrm{Ca}_{\mathrm{Li}}^{\mathrm{b}} h^{(1)} - z\hat{\varphi}_{\mathrm{b}}^{(1)}) & n = 1. \end{cases}$$
$$\text{(B.16)}$$

The above expression is obtained, similarly to Eq. (B.13), by expanding $\varphi_{\mathrm{b}}(\mathbf{x} \in \Gamma, t)$ and its gradient in Taylor series around the base state $\Gamma^{(0)}$, and by defining $\hat{\varphi}_{\mathrm{b}}^{(1)}$ as

$$\hat{\varphi}_{\mathrm{b}}^{(1)} = h^{(1)}\frac{\mathrm{d}\varphi_{\mathrm{b}}^{(0)}}{\mathrm{d}x} + \varphi_{\mathrm{b}}^{(1)}. \qquad \text{(B.17)}$$

B.1.4 Battery without a buffer

The linear stability analysis of ASSBs without a buffer is identical to Scenario 2, in which the transport properties of the buffer are equal to those in the solid electrolyte and the interface $x = L_1$ is absent. Thus, Eqs. (B.4)–(B.7) are replaced with Eq. (B.4) defined for the whole domain $h^{(0)} < x < 1$, on which Eqs. (B.14)–(B.17) (minus the

interfacial condition at $x = L_1$ and with $Ca_{Li}^b = Ca_{Li}^{el}$) are also defined.

B.1.5 Base-state solutions

Analytical solutions of the base-state BVPs, i.e., Eqs. (B.4)–(B.16) for $n = 0$, yields the spatial distribution of the electric potential throughout the half cell in Scenario 1,

$$
\varphi^{(0)}(\xi;t) = \begin{cases} \varphi_e & 0 \le \xi \le \hat{L}_1 \\ \dfrac{\xi - 1 + Ut}{\sigma_{el}} R_\Gamma^{(0)} & \hat{L}_1 \le \xi \le 1 \end{cases} \tag{B.18}
$$

and in Scenario 2,

$$
\varphi^{(0)}(\xi;t) = \begin{cases} \left(\dfrac{\xi - \hat{L}_1}{\sigma_b} + \dfrac{\hat{L}_1 - 1 + Ut}{\sigma_{el}} \right) R_{Li}^{(0)} & 0 \le \xi \le \hat{L}_1 \\ \dfrac{\xi - 1 + Ut}{\sigma_{el}} R_{Li}^{(0)} & \hat{L}_1 \le \xi \le 1 - Ut. \end{cases} \tag{B.19}
$$

These solutions are written in the moving coordinate system $\xi = x - Ut$, with $\hat{L}_1 = L_1 - Ut$. The linear stability analysis is valid for early stages of the dendrite formation, during which $Ut \ll L_1$ and (since $L_1 \ll 1$) $Ut \ll 1$. For these early times, $\varphi^{(0)}(\xi;t)$ in Eqs (B.18) and (B.19) loose their explicit dependence on t, reducing to

$$
\varphi^{(0)}(\xi) = \begin{cases} \varphi_e & 0 \le \xi \le L_1 \\ \dfrac{\xi - 1}{\sigma_{el}} R_\Gamma^{(0)} & L_1 \le \xi \le 1 \end{cases} \tag{B.20}
$$

in Scenario 1 and to

$$
\varphi^{(0)}(\xi) = \begin{cases} \left(\dfrac{\xi - L_1}{\sigma_b} + \dfrac{L_1 - 1}{\sigma_{el}} \right) R_{Li}^{(0)} & 0 \le \xi \le L_1 \\ \dfrac{\xi - 1}{\sigma_{el}} R_{Li}^{(0)} & L_1 \le \xi \le 1 \end{cases} \tag{B.21}
$$

in Scenario 2.

These solutions are implicit because of the nonlinear dependence of $R_{Li}^{(0)}$ and $R_\Gamma^{(0)}$

on $\varphi^{(0)}(\xi)$ and, in Scenario 1, on

$$c^{(0)}(\xi) = \begin{cases} \frac{R_\Gamma^{(0)}}{D_b}\xi + \left(\frac{R_\Gamma^{(0)}}{k_0} + 1\right)c^\Theta, & 0 \leq \xi \leq L_1 \\ 1 & L_1 \leq \xi \leq 1. \end{cases} \tag{B.22}$$

In other words, for any given φ_e, these solutions take the form $\varphi^{(0)}(\xi) = \mathcal{F}[\varphi^{(0)}(\xi)]$, where the functional $\mathcal{F}[\cdot]$ is defined by either Eq. (B.20) or Eq. (B.21). This root-finding problem is solved numerically with the Matlab function `fzero`.

Figure B.1 exhibits the spatial distribution of the base-state electric potential, $\varphi^{(0)}(\xi)$, in ASSBs without a buffer and with the highly conductive buffer (Scenario 1 with $D_b = 1$ and $\tilde{\mathrm{Ca}} = 1$). We do not show the solutions for the low-conductivity buffer because they overlap with the buffer-free expressions when $\sigma_b = 1$. The electric potential increases linearly with distance from the evolving anode, ξ, with higher values of the applied potential φ_e inducing larger potential gradients in the electrolyte. In Scenario 1, the Faradaic reaction $\mathrm{Li}^+ + e^- \rightarrow \mathrm{Li}$ takes place at the the buffer/electrolyte interface and the electric potential in the buffer is constant.
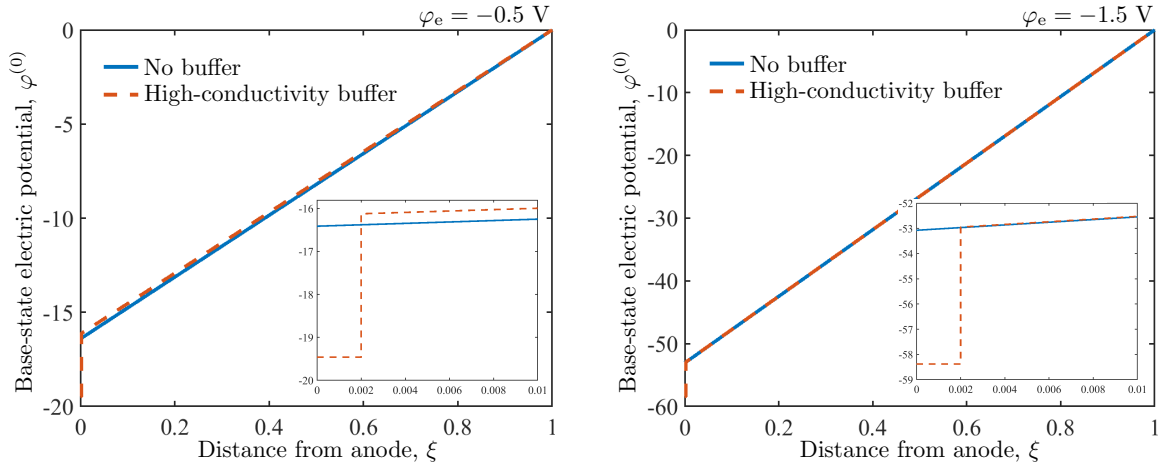
Figure B.1: Spatial profiles of the dimensionless base-state electric potential $\varphi^{(0)}(\xi)$ in ASSBs without a buffer and with a high-conductivity buffer ($D_b = 1$ and $\mathrm{Ca}_{\mathrm{Li}}^{\mathrm{el}} = \mathrm{Ca}_{\mathrm{Li}}^{\mathrm{b}}$). These are plotted in the dimensionless moving coordinate system $\xi = x - Ut$, wherein ξ represents the distance from the growing electrode surface.

The solutions for $\varphi^{(0)}(\xi)$ and $c^{(0)}(\xi)$, and their first- and second-order derivatives,

serve as coefficients in the perturbed-state BVPs, i.e., in Eqs. (B.4)–(B.16) with $n = 1$. The latter are solved numerically [17] by employing a second-order finite-difference scheme and solving the resulting generalized eigenvalue problem with the Matlab function `eigs` to compute the dispersion relation $w = w(k)$. Alternatively, under certain assumptions, the perturbed-state BVPs for $\varphi^{(1)}(\xi)$ and the dispersion relations from Eq. (B.12) are solved analytically in Appendix B.

B.2 Analytical dispersion relations

B.2.1 Scenario 1: High-conductivity buffer

Let us assume that $w \ll Dk^2$ in (B.8) with $n = 1$, i.e., that the temporal fluctuations of the first-order perturbation $c^{(1)}(\xi)$ are negligible. This yields a PDE

$$\frac{\mathrm{d}^2 c^{(1)}}{\mathrm{d}\xi^2} = k^2 c^{(1)}, \qquad 0 < \xi < L_1, \tag{B.23}$$

whose solution is $c^{(1)}(\xi) = \beta_1 \exp(k\xi) + \beta_2 \exp(-k\xi)$. The constants of integration β_1 and β_2 are obtained from boundary conditions (B.9),

$$D_{\mathrm{b}} \frac{\mathrm{d}c^{(1)}}{\mathrm{d}\xi}(0) = R_{\Gamma}^{(1)}, \qquad D_{\mathrm{b}} \frac{\mathrm{d}c^{(1)}}{\mathrm{d}\xi}(L_1) = R_{\mathrm{Li}}^{(1)}. \tag{B.24}$$

Substituting this solution into Eq. (B.12), and recalling that $z R_{\mathrm{Li}}^{(0)} = I^{(0)}$, we obtain the dispersion relation

$$w = \frac{\omega c_0}{z} \frac{I^{(0)}/c^{\Theta} - D_{\mathrm{b}} \mathrm{Ca}_{\mathrm{Li}}^{\mathrm{b}} (\alpha_{\mathrm{cat}} I^{(0)}/k_0 + z) k^2}{D_{\mathrm{b}}/k_0 - B}, \tag{B.25a}$$

where

$$a = -\frac{k_0}{c^{\Theta}} \mathrm{e}^{(1-\alpha_{\mathrm{cat}}) z \eta_\alpha^{(0)}}, \qquad A = \frac{a + D_{\mathrm{b}} k}{a - D_{\mathrm{b}} k} \mathrm{e}^{2kL_1}, \qquad B = \frac{1}{c^{\Theta} k} \frac{1-A}{1+A}. \tag{B.25b}$$

The critical wavenumber, k_{cr}, is a wavenumber k for which $w = 0$. It follows from Eq. (B.25) that

$$k_{cr} = \sqrt{\frac{I^{(0)}}{Ca_{Li}^{b} D_{b} c^{\Theta} (\alpha_{cat} I^{(0)}/k_0 + z)}}. \tag{B.26}$$

B.2.2 Scenario 2: Low-conductivity buffer

The solution of BVPs (B.4)–(B.7) and (B.14)–(B.17) is

$$\varphi^{(1)} = A \begin{cases} \xi + (L_1 - 1)\dfrac{\sigma_b}{\sigma_{el}} - L_1 & 0 \leq \xi \leq L_1 \\[2mm] \dfrac{\sigma_b}{\sigma_{el}} (\xi - 1) & L_1 \leq \xi \leq 1, \end{cases} \tag{B.27a}$$

where

$$A = \frac{z h^{(1)} R_{Li}^{(0)} - k^2 h^{(1)} Ca_{Li}^{b} \sigma_b}{\sigma_b/K - z[(L_1 - 1)\sigma_b/\sigma_{el} - L_1]} \tag{B.27b}$$

and

$$K = k_0 e^{-\alpha_{cat} z \eta_\alpha^{(0)}} [(1 - \alpha_{cat}) e^{z \eta_\alpha^{(0)}} + \alpha_{cat}]. \tag{B.27c}$$

Substituting Eq. (B.27) into Eq. (B.12), and recalling that $z R_{Li}^{(0)} = I^{(0)}$, yields the dispersion relation,

$$w = \omega c_0 \frac{I^{(0)} - k^2 Ca_{Li}^{b} \sigma_b}{\sigma_b/K - z[(L_1 - 1)\sigma_b/\sigma_{el} - L_1]}, \tag{B.28}$$

and the critical wavenumber,

$$k_{cr} = \sqrt{\frac{I^{(0)}}{Ca_{Li}^{b} \sigma_b}}. \tag{B.29}$$

In the absence of a buffer, $L_1 = 0$, $\sigma_b = \sigma_{el}$, and $\sigma_b = \sigma_{el}$. Hence, for ASSBs without a buffer, Eqs. (B.28) and (B.29) reduce to

$$w = \omega c_0 \frac{I^{(0)} - k^2 Ca_{Li}^{el} \sigma_{el}}{\sigma_{el}/K + z} \tag{B.30}$$

and the critical wavenumber k_{cr},

$$k_{\mathrm{cr}} = \sqrt{\frac{I^{(0)}}{\mathrm{Ca}_{\mathrm{Li}}^{\mathrm{el}} \sigma_{\mathrm{el}}}}. \tag{B.31}$$

Bibliography

[1] US Energy Information Administration. *Annual Energy Outlook 2023 With Projections to 2050*. 2023.

[2] Gregory L Plett. *Battery management systems, Volume I: Battery modeling*. Artech House, 2015.

[3] Colin McKerracher. Bnef talk 2020: Electric mobility: The end of the beginning. URL: https://vimeo.com/389506892, 2 2020.

[4] Philipp Adelhelm, Pascal Hartmann, Conrad L Bender, Martin Busche, Christine Eufinger, and Juergen Janek. From lithium to sodium: cell chemistry of room temperature sodium–air and sodium–sulfur batteries. *Beilstein journal of nanotechnology*, 6(1):1016–1055, 2015.

[5] Neelima Paul, Morten Wetjen, Sebastian Busch, Hubert Gasteiger, and Ralph Gilles. Contrast matched sans for observing sei and pore clogging in silicon-graphite anodes. *Journal of The Electrochemical Society*, 166(6):A1051, 2019.

[6] Aashutosh Mistry, Daniel Juarez-Robles, Malcolm Stein IV, Kandler Smith, and Partha P Mukherjee. Analysis of long-range interaction in lithium-ion battery electrodes. *Journal of Electrochemical Energy Conversion and Storage*, 13(3):031006, 2016.

[7] Jonghyun Park, Jeong Hun Seo, Gregory Plett, Wei Lu, and Ann Marie Sastry. Numerical simulation of the effect of the dissolution of limn2o4 particles on li-ion battery performance. *Electrochemical and Solid-State Letters*, 14(2):A14, 2010.

[8] Yoon Koo Lee. The effect of active material, conductive additives, and binder in a cathode composite electrode on battery performance. *Energies*, 12(4), 2019.

[9] Xianke Lin, Jonghyun Park, Lin Liu, Yoonkoo Lee, AM Sastry, and Wei Lu. A comprehensive capacity fade model and analysis for li-ion batteries. *Journal of The Electrochemical Society*, 160(10):A1701, 2013.

[10] Marita Pigłowska, Beata Kurc, Maciej Galiński, Paweł Fuć, Michalina Kamińska, Natalia Szymlet, and Paweł Daszkiewicz. Challenges for safe electrolytes applied in lithium-ion cells—a review. *Materials*, 14(22):6783, 2021.

[11] Kevin N Wood, Eric Kazyak, Alexander F Chadwick, Kuan-Hung Chen, Ji-Guang Zhang, Katsuyo Thornton, and Neil P Dasgupta. Dendrites and pits: Untangling the complex behavior of lithium metal anodes through operando video microscopy. *ACS central science*, 2(11):790–801, 2016.

[12] Lucy M Morgan, Michael P Mercer, Arihant Bhandari, Chao Peng, Mazharul M Islam, Hui Yang, Julian Holland, Samuel W Coles, Ryan Sharpe, Aron Walsh, et al. Pushing the boundaries of lithium battery research with atomistic modelling on different scales. *Progress in Energy*, 4(1):012002, 2021.

[13] P Wang, L Yang, H Wang, DM Tartakovsky, and S Onori. Temperature estimation from current and voltage measurements in lithium-ion battery systems. *Journal of Energy Storage*, 34:102133, 2021.

[14] Qiu He, Bin Yu, Zhaohuai Li, and Yan Zhao. Density functional theory for battery materials. *Energy & Environmental Materials*, 2(4):264–279, 2019.

[15] Weiyu Li and Daniel M Tartakovsky. Effective representation of active material and carbon binder in porous electrodes. *Journal of The Electrochemical Society*, 169(4):040556, 2022.

[16] Francesca Boso, Weiyu Li, Kimoon Um, and Daniel M Tartakovsky. Impact of carbon binder domain on the performance of lithium-metal batteries. *Journal of The Electrochemical Society*, 169(10):100550, 2022.

[17] Weiyu Li, Hamdi A Tchelepi, Yiguang Ju, and Daniel M Tartakovsky. Stability-guided strategies to mitigate dendritic growth in lithium-metal batteries. *Journal of The Electrochemical Society*, 169(6):060536, 2022.

[18] Weiyu Li, Hamdi A Tchelepi, and Daniel M Tartakovsky. Screening of electrolyte-anode buffers to suppress lithium dendrite growth in all-solid-state batteries. *Journal of the Electrochemical Society*, 170(5):050510, 2023.

[19] Weiyu Li, Haruko M Wainwright, Qina Yan, Haiyan Zhou, Baptiste Dafflon, Yuxin Wu, Roelof Versteeg, and Daniel M Tartakovsky. Estimation of evapotranspiration rates and root water uptake profiles from soil moisture sensor array data. *Water Resources Research*, 57(11):e2021WR030747, 2021.

[20] Weiyu Li and Daniel M Tartakovsky. Fast and accurate estimation of evapotranspiration for smart agriculture. *Water Resources Research*, 59(4):e2023WR034535, 2023.

[21] Weiyu Li, Amy G Tsai, Marcos Intaglietta, and Daniel M Tartakovsky. A model of anemic tissue perfusion after blood transfusion shows critical role of endothelial response to shear stress stimuli. *Journal of Applied Physiology*, 131(6):1815–1823, 2021.

[22] Maira Indrikova, Stephan Grunwald, Frederik Golks, Andreas Netz, Bastian Westphal, and Arno Kwade. The Morphology of Battery Electrodes with the Focus of the Conductive Additives Paths. *Journal of The Electrochemical Society*, 162(10):A2021–A2025, 7 2015.

[23] Mingyan Wu, Xingcheng Xiao, Nenad Vukmirovic, Shidi Xun, Prodip K. Das, Xiangyun Song, Paul Olalde-Velasco, Dongdong Wang, Adam Z. Weber, Lin Wang Wang, Vincent S. Battaglia, Wanli Yang, and Gao Liu. Toward an ideal polymer binder design for high-capacity battery anodes. *Journal of the American Chemical Society*, 135(32):12048–12056, 8 2013.

[24] Jianchao Chen, Jianyong Liu, Yue Qi, Tao Sun, and Xiaodong Li. Unveiling the

roles of binder in the mechanical integrity of electrodes for lithium-ion batteries. *Journal of The Electrochemical Society*, 160(9):A1502, 2013.

[25] G Liu, H Zheng, S Kim, Y Deng, A M Minor, X Song, and Vincent S Battaglia. Effects of various conductive additive and polymeric binder contents on the performance of a lithium-ion composite cathode. *Journal of The Electrochemical Society*, 155(12):A887, 2008.

[26] David E Stephenson, Bryce C Walker, Cole B Skelton, Edward P Gorzkowski, David J Rowenhorst, and Dean R Wheeler. Modeling 3D Microstructure and Ion Transport in Porous Li-Ion Battery Electrodes. *Journal of The Electrochemical Society*, 158(7):781–789, 2011.

[27] Nathan A. Zacharias, Douglas R. Nevers, Cole Skelton, Karey Knackstedt, David E. Stephenson, and Dean R. Wheeler. Direct Measurements of Effective Ionic Transport in Porous Li-Ion Electrodes. *Journal of The Electrochemical Society*, 160(2):A306–A311, 12 2013.

[28] Moritz Kroll, Sarah L. Karstens, Marvin Cronau, Alexandra Höltzel, Sabine Schlabach, Nikita Nobel, Claudia Redenbach, Bernhard Roling, and Ulrich Tallarek. Three-Phase Reconstruction Reveals How the Microscopic Structure of the Carbon-Binder Domain Affects Ion Transport in Lithium-Ion Batteries. *Batteries & Supercaps*, 4(8):1363–1373, 8 2021.

[29] Xuekun Lu, Antonio Bertei, Donal P. Finegan, Chun Tan, Sohrab R. Daemi, Julia S. Weaving, Kieran B. O'Regan, Thomas M.M. Heenan, Gareth Hinds, Emma Kendrick, Dan J.L. Brett, and Paul R. Shearing. 3D microstructure design of lithium-ion battery electrodes assisted by X-ray nano-computed tomography and modelling. *Nature Communications*, 11(1), 12 2020.

[30] Bradley L. Trembacki, Aashutosh N. Mistry, David R. Noble, Mark E. Ferraro, Partha P. Mukherjee, and Scott A. Roberts. Editors' Choice—Mesoscale Analysis of Conductive Binder Domain Morphology in Lithium-Ion Battery Electrodes. *Journal of The Electrochemical Society*, 165(13):E725, 10 2018.

[31] Francois LE Usseglio-Viretta, Andrew Colclasure, Aashutosh N Mistry, Koffi Pierre Yao Claver, Fezzeh Pouraghajan, Donal P Finegan, Thomas M M Heenan, Daniel Abraham, Partha P Mukherjee, Dean Wheeler, Paul Shearing, Samuel J Cooper, and Smith Kandler. Resolving the discrepancy in tortuosity factor estimation for li-ion battery electrodes through micro-macro modeling and experiment. *Journal of The Electrochemical Society*, 165(14):A3403, 2018.

[32] Simon Hein, Timo Danner, Daniel Westhoff, Benedikt Prifling, Rares Scurtu, Lea Kremer, Alice Hoffmann, André Hilger, Markus Osenberg, Ingo Manke, Margret Wohlfahrt-Mehrens, Volker Schmidt, and Arnulf Latz. Influence of Conductive Additives and Binder on the Impedance of Lithium-Ion Battery Electrodes: Effect of Morphology. *Journal of The Electrochemical Society*, 167(1):013546, 1 2020.

[33] Giles Richardson, Ivan Korotkin, Rahifa Ranom, Michael Castle, and JM Foster. Generalised single particle models for high-rate operation of graded lithium-ion electrodes: Systematic derivation and validation. *Electrochimica Acta*, 339:135862, 4 2020.

[34] Scott G Marquis, Valentin Sulzer, Robert Timms, Colin P Please, and S Jon Chapman. An asymptotic derivation of a single particle model with electrolyte. *Journal of The Electrochemical Society*, 166(15):A3693, 2019.

[35] Meng Guo, Godfrey Sikha, and Ralph E White. Single-particle model for a lithium-ion cell: Thermal behavior. *Journal of The Electrochemical Society*, 158(2):A122, 2010.

[36] Jie Li, Nima Lotfi, Robert G Landers, and Jonghyun Park. A single particle model for lithium-ion batteries with electrolyte and stress-enhanced diffusion physics. *Journal of The Electrochemical Society*, 164(4):A874, 2017.

[37] Marc Doyle, Thomas F. Fuller, and John Newman. Modeling of Galvanostatic Charge and Discharge of the Lithium/Polymer/Insertion Cell. *Journal of The Electrochemical Society*, 140(6):1526–1533, 6 1993.

[38] Wei Lai and Francesco Ciucci. Mathematical modeling of porous battery electrodes-Revisit of Newman's model. *Electrochimica Acta*, 56(11):4369–4377, 4 2011.

[39] Markus Schmuck. Upscaling of Solid-electrolyte Composite Intercalation Cathodes for Energy Storage Systems. *Applied Mathematics Research eXpress*, 2017(2):402–430, 9 2017.

[40] Xuan Zhang and Daniel M. Tartakovsky. Effective ion diffusion in charged nanoporous materials. *Journal of The Electrochemical Society*, 164(4):E53–E61, 2017.

[41] Graeme W. Milton. *The Theory of Composites*. Cambridge Monographs on Applied and Computational Mathematics. Cambridge University Press, 2002.

[42] Todd R. Ferguson and Martin Z. Bazant. Nonequilibrium Thermodynamics of Porous Electrodes. *Journal of The Electrochemical Society*, 159(12):A1967–A1985, 10 2012.

[43] Yunjung Hyun, Shlomo P Neuman, Velimir V Vesselinov, Walter A Illman, Daniel M Tartakovsky, and Vittorio Di Federico. Theoretical interpretation of a pronounced permeability scale effect in unsaturated fractured tuff. *Water Resources Research*, 38(6), 2002.

[44] Gerardo Severino and Antonio Coppola. A note on the apparent conductivity of stratified porous media in unsaturated steady flow above a water table. *Transport in Porous Media*, 91:733–740, 2012.

[45] Silvia Tozza and Gerardo Toraldo. Numerical hints for insulation problems. *Applied Mathematics Letters*, 123:107609, 2022.

[46] Ulrich Hornung. *Homogenization and porous media*, volume 6. Springer, 2012.

[47] Kazuo Yamamoto, Yasutoshi Iriyama, Toru Asaka, Tsukasa Hirayama, Hideki Fujita, Craig A.J. Fisher, Katsumasa Nonaka, Yuji Sugita, and Zempachi

Ogumi. Dynamic Visualization of the Electric Potential in an All-Solid-State Rechargeable Lithium Battery. *Angewandte Chemie International Edition*, 49(26):4414–4417, 6 2010.

[48] Gregory B Less, Jung Hwan Seo, S Han, Ann Marie Sastry, Jochen Zausch, Arnulf Latz, Sebastian Schmidt, Christian Wieser, Dirk Kehrwald, and Stefan Fell. Micro-Scale Modeling of Li-Ion Batteries: Parameterization and Validation. *Journal of The Electrochemical Society*, 159(6):A697–A704, 3 2012.

[49] Juraj. Numerical inversion of laplace transforms in matlab, 2022.

[50] Daniel M Tartakovsky and Shlomo P Neuman. Transient effective hydraulic conductivities under slowly and rapidly varying mean gradients in bounded three-dimensional random media. *Water Resources Research*, 34(1):21–32, 1998.

[51] Lea Sophie Kremer, Alice Hoffmann, Timo Danner, Simon Hein, Benedikt Prifling, Daniel Westhoff, Christian Dreer, Arnulf Latz, Volker Schmidt, and Margret Wohlfahrt-Mehrens. Manufacturing Process for Improved Ultra-Thick Cathodes in High-Energy Lithium-Ion Batteries. *Energy Technology*, 8(2):1900167, 2 2020.

[52] Yuping Wu, Elke Rahm, and Rudolf Holze. Carbon anode materials for lithium ion batteries. *Journal of Power Sources*, 114(2):228–236, 2003.

[53] Xin-Bing Cheng, Rui Zhang, Chen-Zi Zhao, and Qiang Zhang. Toward safe lithium metal anode in rechargeable batteries: A review. *Chemical Reviews*, 117(15):10403–10473, 2017.

[54] Xuan Zhang and Daniel M Tartakovsky. Optimal design of nanoporous materials for electrochemical devices. *Applied Physics Letters*, 110(14):143103, 2017.

[55] Honghe Zheng, Ruizhi Yang, Gao Liu, Xiangyun Song, and Vincent S Battaglia. Cooperation between active material, polymeric binder and conductive carbon additive in lithium ion battery cathode. *The Journal of Physical Chemistry C*, 116(7):4875–4882, 2012.

[56] Arumugam Manthiram. A reflection on lithium-ion battery cathode chemistry. *Nature Communications*, 11(1):1–9, 2020.

[57] Aashutosh Mistry, Stephen Trask, Alison Dunlop, Gerald Jeka, Bryant Polzin, Partha P Mukherjee, and Venkat Srinivasan. Quantifying negative effects of carbon-binder networks from electrochemical performance of porous li-ion electrodes. *Journal of The Electrochemical Society*, 168(7):070536, 2021.

[58] Malcolm Stein, Aashutosh Mistry, and Partha P Mukherjee. Mechanistic understanding of the role of evaporation in electrode processing. *Journal of The Electrochemical Society*, 164(7):A1616, 2017.

[59] Sohrab R Daemi, Chun Tan, Tobias Volkenandt, Samuel J Cooper, Anna Palacios-Padros, James Cookson, Dan JL Brett, and Paul R Shearing. Visualizing the carbon binder phase of battery electrodes in three dimensions. *ACS Applied Energy Materials*, 1(8):3702–3710, 2018.

[60] Lukas Zielke, Tobias Hutzenlaub, Dean R Wheeler, Ingo Manke, Tobias Arlt, Nils Paust, Roland Zengerle, and Simon Thiele. A combination of x-ray tomography and carbon binder modeling: reconstructing the three phases of licoo2 li-ion battery cathodes. *Advanced Energy Materials*, 4(8):1301617, 2014.

[61] Aashutosh N Mistry, Kandler Smith, and Partha P Mukherjee. Secondary-phase stochastics in lithium-ion battery electrodes. *ACS Applied Materials & Interfaces*, 10(7):6317–6326, 2018.

[62] Bradley Trembacki, Eric Duoss, Geoffrey Oxberry, Michael Stadermann, and Jayathi Murthy. Mesoscale electrochemical performance simulation of 3d interpenetrating lithium-ion battery electrodes. *Journal of the Electrochemical Society*, 166(6):A923, 2019.

[63] Daniel M Tartakovsky and Marco Dentz. Diffusion in porous media: phenomena and mechanisms. *Transport in Porous Media*, 130(1):105–127, 2019.

[64] Toby L Kirk, Colin P Please, and S Jon Chapman. Physical modelling of the slow voltage relaxation phenomenon in lithium-ion batteries. *Journal of The Electrochemical Society*, 168(6):060554, 2021.

[65] Ali Jokar, Barzin Rajabloo, Martin Désilets, and Marcel Lacroix. Review of simplified Pseudo-two-Dimensional models of lithium-ion batteries. *Journal of Power Sources*, 327:44–55, 2016.

[66] Samuel J Cooper, Antonio Bertei, Paul R Shearing, JA Kilner, and Nigel P Brandon. Taufactor: An open-source application for calculating tortuosity factors from tomographic data. *SoftwareX*, 5:203–210, 2016.

[67] Valentin Sulzer, Scott G Marquis, Robert Timms, Martin Robinson, and S Jon Chapman. Python battery mathematical modelling (PyBaMM). *Journal of Open Research Software*, 9(1), 2021.

[68] Jonathan E Guyer, Daniel Wheeler, and James A Warren. Fipy: Partial differential equations with python. *Computing in Science & Engineering*, 11(3):6–15, 2009.

[69] Christophe Geuzaine and Jean-François Remacle. Gmsh: A 3-D finite element mesh generator with built-in pre-and post-processing facilities. *International Journal for Numerical Methods in Engineering*, 79(11):1309–1331, 2009.

[70] Owen Crowther and Alan C West. Effect of electrolyte composition on lithium dendrite growth. *Journal of the Electrochemical Society*, 155(11):A806, 2008.

[71] Asghar Aryanfar, Daniel Brooks, Boris V Merinov, William A Goddard III, Agustín J Colussi, and Michael R Hoffmann. Dynamics of lithium dendrite growth and inhibition: Pulse charging experiments and monte carlo calculations. *The Journal of Physical Chemistry letters*, 5(10):1721–1726, 2014.

[72] Qing Chen, Ke Geng, and Karl Sieradzki. Prospects for dendrite-free cycling of li metal batteries. *Journal of The Electrochemical Society*, 162(10):A2004, 2015.

[73] Peng Bai, Ju Li, Fikile R Brushett, and Martin Z Bazant. Transition of lithium growth mechanisms in liquid electrolytes. *Energy & Environmental Science*, 9(10):3221–3229, 2016.

[74] Amir Riaz and Hamdi A. Tchelepi. Linear stability analysis of immiscible two-phase flow in porous media with capillary dispersion and density variation. *Physics of Fluids*, 16(12):4727–4737, 2004.

[75] Hongtao Zhong, Mikhail N. Shneider, Xingqian Mao, and Yiguang Ju. Dynamics and chemical mode analysis of plasma thermal-chemical instability. *Plasma Sources Science and Technology*, 30(3), 3 2021.

[76] Lars Göran Sundström and Fritz H. Bark. On morphological instability during electrodeposition with a stagnant binary electrolyte. *Electrochimica Acta*, 40(5):599–614, 1995.

[77] Juan Elezgaray, Christophe Léger, and Françoise Argoul. Linear stability analysis of unsteady galvanostatic electrodeposition in the two-dimensional diffusion-limited regime. *Journal of The Electrochemical Society*, 145(6):2016–2024, 6 1998.

[78] Mukul D. Tikekar, Lynden A. Archer, and Donald L. Koch. Stability analysis of electrodeposition across a structured electrolyte with immobilized anions. *Journal of The Electrochemical Society*, 161(6):A847–A855, 4 2014.

[79] Edwin Khoo, Hongbo Zhao, and Martin Z. Bazant. Linear stability analysis of transient electrodeposition in charged porous media: Suppression of dendritic growth by surface conduction. *Journal of The Electrochemical Society*, 166(10):A2280–A2299, 6 2019.

[80] Ankit Verma, Hiroki Kawakami, Hiroyuki Wada, Anna Hirowatari, Nobuhisa Ikeda, Yoshifumi Mizuno, Toshikazu Kotaka, Koichiro Aotani, Yuichiro Tabuchi, and Partha P. Mukherjee. Microstructure and pressure-driven electrodeposition stability in solid-state batteries. *Cell Reports Physical Science*, 2(1):100301, 1 2021.

[81] Mukul D. Tikekar, Lynden A. Archer, and Donald L. Koch. Stabilizing electrodeposition in elastic solid electrolytes containing immobilized anions. *Science Advances*, 2(7), 2016.

[82] Mukul D. Tikekar, Gaojin Li, Lynden A. Archer, and Donald L. Koch. Electroconvection and morphological instabilities in potentiostatic electrodeposition across liquid electrolytes with polymer additives. *Journal of The Electrochemical Society*, 165(16):A3697–A3713, 12 2018.

[83] Tianhan Gao, Guangyu Liu, and Wei Lu. A theory that couples electrochemistry and thin film piezoelectricity with stability analysis for electrodeposition. *Journal of the Mechanics and Physics of Solids*, 162:104827, 5 2022.

[84] Akash Ganesh, Dipin S. Pillai, and R. Narayanan. Effect of low-frequency AC forcing on the morphological instability arising in electrodeposition. *Journal of Engineering Mathematics*, 132(1):1–18, 2 2022.

[85] T. J. Rademaker, G. R. A. Akkermans, D. L. Danilov, and P. H. L. Notten. On the deviation of electro-neutrality in Li-ion battery electrolytes. *Journal of The Electrochemical Society*, 161(8):E3365–E3372, 6 2014.

[86] Xinyang Wang, Ming Chen, Siyuan Li, Chang Zhao, Weidong Zhang, Zeyu Shen, Yi He, Guang Feng, and Yingying Lu. Inhibiting dendrite growth via regulating the electrified interface for fast-charging lithium metal anode. *ACS Central Science*, 7(12):2029–2038, 2021.

[87] Jianming Zheng, Mark H Engelhard, Donghai Mei, Shuhong Jiao, Bryant J Polzin, Ji-Guang Zhang, and Wu Xu. Electrolyte additive enabled fast charging and stable cycling lithium metal batteries. *Nature Energy*, 2(3):1–8, 2017.

[88] Christoffer P Nielsen and Henrik Bruus. Morphological instability during steady electrodeposition at overlimiting currents. *Physical Review E*, 92:52310, 2015.

[89] Jean-Noël Chazalviel. Electrochemical aspects of the generation of ramified metallic electrodeposits. *Physical Review A*, 42:15, 1990.

[90] C. L. Druzgalski, M. B. Andersen, and A. Mani. Direct numerical simulation of electroconvective instability and hydrodynamic chaos near an ion-selective surface. *Physics of Fluids*, 25(11):110804, 8 2013.

[91] M. Rosso, T. Gobron, C. Brissot, J. N. Chazalviel, and S. Lascaud. Onset of dendritic growth in lithium/polymer cells. *Journal of Power Sources*, 97-98:804–806, 7 2001.

[92] Jinwang Tan, Alexandre M. Tartakovsky, Kim Ferris, and Emily M. Ryan. Investigating the effects of anisotropic mass transport on dendrite growth in high energy density lithium batteries. *Journal of The Electrochemical Society*, 163(2):A318–A327, 12 2016.

[93] Sohail Murad. The role of external electric fields in enhancing ion mobility, drift velocity, and drift–diffusion rates in aqueous electrolyte solutions. *The Journal of Chemical Physics*, 134(11):114504, 3 2011.

[94] Victor Ponce, Diego E. Galvez-Aranda, and Jorge M. Seminario. Analysis of a Li-ion nanobattery with graphite anode using molecular dynamics simulations. *Journal of Physical Chemistry C*, 121(23):12959–12971, 6 2017.

[95] Bharath Ravikumar, Mahesh Mynam, and Beena Rai. Molecular dynamics investigation of electric field altered behavior of lithium ion battery electrolytes. *Journal of Molecular Liquids*, 300:112252, 2 2020.

[96] Man Liu, Peter J. Chimtali, Xue Bin Huang, and Ru Bo Zhang. Structures and dynamic properties of the $LiPF_6$ electrolytic solution under electric fields – a theoretical study. *Physical Chemistry Chemical Physics*, 21(24):13186–13193, 6 2019.

[97] Lars Ole Valøen and Jan N Reimers. Transport properties of $LiPF_6$-based Li-ion battery electrolytes. *Journal of The Electrochemical Society*, 152(5):A882, 2005.

[98] Sarah Stewart and John Newman. Measuring the salt activity coefficient in lithium-battery electrolytes. *Journal of The Electrochemical Society*, 155(6):A458, 2008.

[99] Tingzheng Hou, Guang Yang, Nav Nidhi Rajput, Julian Self, Sang Won Park, Jagjit Nanda, and Kristin A. Persson. The influence of FEC on the solvation structure and reduction reaction of $LiPF_6$/EC electrolytes and its implication for solid electrolyte interphase formation. *Nano Energy*, 64:103881, 10 2019.

[100] ed. Rumble, John R. *CRC Handbook of Chemistry and Physics*. 102nd Edition (Internet Version 2021). CRC Press/Taylor & Francis, Boca Raton, FL, 2021.

[101] R Naejus, D Lemordant, R Coudert, and P Willmann. Excess thermodynamic properties of binary mixtures containing linear or cyclic carbonates as solvents at the temperatures 298.15 K and 315.15 K. *The Journal of Chemical Thermodynamics*, 29:15031515, 1997.

[102] CODATA Value: vacuum electric permittivity.

[103] Shanshan Xu, Kuan-Hung Chen, Neil P. Dasgupta, Jason B. Siegel, and Anna G. Stefanopoulou. Evolution of dead lithium growth in lithium metal batteries: Experimentally validated model of the apparent capacity loss. *Journal of The Electrochemical Society*, 166(14):A3456–A3463, 10 2019.

[104] C T Tan and G M Homsy. Stability of miscible displacements in porous media: Rectilinear flow. *Physics of Fluids*, 29(11):3549–3556, 1986.

[105] Yannis C Yortsos and Murat Zeybek. Dispersion driven instability in miscible displacement in porous media. *Physics of Fluids*, 31(12):3511–3518, 1988.

[106] Amir Riaz and Hamdi A. Tchelepi. Influence of relative permeability on the stability characteristics of immiscible flow in porous media. *Transport in Porous Media*, 64(3):315–338, 9 2006.

[107] Amir Riaz and Hamdi A. Tchelepi. Stability of two-phase vertical flow in homogeneous porous media. *Physics of Fluids*, 19(7):72103, 2007.

[108] Mikko Haataja, David J Srolovitz, and Andrew B Bocarsly. Morphological stability during electrodeposition: I. Steady states and stability analysis. *Journal of The Electrochemical Society*, 150(10):C699, 2003.

[109] Mikko Haataja, David J Srolovitz, and Andrew B Bocarsly. Morphological stability during electrodeposition: II. Additive effects. *Journal of The Electrochemical Society*, 150(10):C708, 2003.

[110] Lei Chen, Hao Wei Zhang, Lin Yun Liang, Zhe Liu, Yue Qi, Peng Lu, James Chen, and Long-Qing Chen. Modulation of dendritic patterns during electrodeposition: A nonlinear phase-field model. *Journal of Power Sources*, 300:376–385, 2015.

[111] Zijian Hong and Venkatasubramanian Viswanathan. Phase-field simulations of lithium dendrite growth with open-source software. *ACS Energy Letters*, 3(7):1737–1743, 2018.

[112] Xiulin Fan and Chunsheng Wang. High-voltage liquid electrolytes for Li batteries: progress and perspectives. *Chemical Society Reviews*, 50:10486–10566, 2021.

[113] Kang Xu and Arthur Von Wald Cresce. Li-solvation/desolvation dictates interphasial processes on graphitic anode in Li ion cells. *Journal of Materials Research*, 27(18):2327–2341, 2012.

[114] Yasuyuki Kondo, Takeshi Abe, and Yuki Yamada. Kinetics of interfacial ion transfer in lithium-ion batteries: Mechanism understanding and improvement strategies. *ACS Applied Materials & Interfaces*, 14(20):22706–22718, 2022.

[115] Ramaswamy Murugan, Venkataraman Thangadurai, and Werner Weppner. Fast lithium ion conduction in garnet-type $Li_7La_3Zr_2O_{12}$. *Angewandte Chemie International Edition*, 46(41):7778–7781, 2007.

[116] Fengyu Shen, Marm B Dixit, Xianghui Xiao, and Kelsey B Hatzell. Effect of pore connectivity on Li dendrite propagation within LLZO electrolytes observed with synchrotron x-ray tomography. *ACS Energy Letters*, 3(4):1056–1061, 2018.

[117] Pallab Barai, Anh T Ngo, Badri Narayanan, Kenneth Higa, Larry A Curtiss, and Venkat Srinivasan. The role of local inhomogeneities on dendrite growth in LLZO-based solid electrolytes. *Journal of The Electrochemical Society*, 167(10):100537, 2020.

[118] Daxian Cao, Xiao Sun, Qiang Li, Avi Natan, Pengyang Xiang, and Hongli Zhu. Lithium dendrite in all-solid-state batteries: growth mechanisms, suppression strategies, and characterizations. *Matter*, 3(1):57–94, 2020.

[119] Shijun Tang, Guiwei Chen, Fucheng Ren, Hongchun Wang, Wu Yang, Chenxi Zheng, Zhengliang Gong, and Yong Yang. Modifying an ultrathin insulating layer to suppress lithium dendrite formation within garnet solid electrolytes. *Journal of Materials Chemistry A*, 9(6):3576–3583, 2021.

[120] Yali Luo, Weiwei Feng, Zijie Meng, Yuanjun Wang, Xue Jiang, and Zihan Xue. Interface modification in solid-state lithium batteries based on garnet-type electrolytes with high ionic conductivity. *Electrochimica Acta*, 397:139285, 2021.

[121] Zefu Zuo, Libin Zhuang, Jinzhuo Xu, Yumeng Shi, Chenliang Su, Peichao Lian, and Bingbing Tian. Lithiophilic silver coating on lithium metal surface for inhibiting lithium dendrites. *Frontiers in Chemistry*, 8:109, 2020.

[122] Takashi Nakamura, Koji Amezawa, Jörn Kulisch, Wolfgang G Zeier, and Jürgen Janek. Guidelines for all-solid-state battery design and electrode buffer layers based on chemical potential profile calculation. *ACS Applied Materials & Interfaces*, 11(22):19968–19976, 2019.

[123] Zeeshan Ahmad, Tian Xie, Chinmay Maheshwari, Jeffrey C Grossman, and Venkatasubramanian Viswanathan. Machine learning enabled computational screening of inorganic solid electrolytes for suppression of dendrite formation in lithium metal anodes. *ACS Central Science*, 4(8):996–1006, 2018.

[124] Maria H Braga, Nicholas S Grundish, Andrew J Murchison, and John B Good-enough. Alternative strategy for a safe rechargeable battery. *Energy & Environmental Science*, 10(1):331–336, 2017.

[125] Hong Fang and Puru Jena. Li-rich antiperovskite superionic conductors based on cluster ions. *Proceedings of the National Academy of Sciences*, 114(42):11046–11051, 2017.

[126] Mei Chin Pang, Yucang Hao, Monica Marinescu, Huizhi Wang, Mu Chen, and Gregory J. Offer. Experimental and numerical analysis to identify the performance limiting mechanisms in solid-state lithium cells under pulse operating conditions. *Physical Chemistry Chemical Physics*, 21(41):22740–22755, 10 2019.

[127] Fudong Han, Andrew S Westover, Jie Yue, Xiulin Fan, Fei Wang, Miaofang Chi, Donovan N Leonard, Nancy J Dudney, Howard Wang, and Chunsheng Wang. High electronic conductivity as the origin of lithium dendrite formation within solid electrolytes. *Nature Energy*, 4(3):187–196, 2019.

[128] Steve D Fabre, Delphine Guy-Bouyssou, Pierre Bouillon, Frédéric Le Cras, and Charles Delacourt. Charge/discharge simulation of an all-solid-state thin-film battery using a one-dimensional model. *Journal of The Electrochemical Society*, 159(2):A104–A115, 12 2011.

[129] Karen E. Thomas-Alyea. Design of porous solid electrolytes for rechargeable metal batteries. *Journal of The Electrochemical Society*, 165(7):A1523–A1528, 5 2018.

[130] Fabian Single, Birger Horstmann, and Arnulf Latz. Theory of impedance spectroscopy for lithium batteries. *The Journal of Physical Chemistry C*, 123(45):27327–27343, 2019.

[131] Lars von Kolzenberg, Arnulf Latz, and Birger Horstmann. Solid–electrolyte interphase during battery cycling: Theory of growth regimes. *ChemSusChem*, 13(15):3901–3910, 2020.

[132] Kostiantyn V Kravchyk, Faruk Okur, and Maksym V Kovalenko. Break-even analysis of all-solid-state batteries with li-garnet solid electrolytes. *ACS Energy Letters*, 6(6):2202–2207, 2021.

[133] PM Gonzalez Puente, Shangbin Song, Shiyu Cao, Leana Ziwen Rannalter, Ziwen Pan, Xing Xiang, Qiang Shen, and Fei Chen. Garnet-type solid electrolyte: Advances of ionic transport performance and its application in all-solid-state batteries. *Journal of Advanced Ceramics*, 10(5):933–972, 2021.

[134] A Alec Talin, Dmitry Ruzmetov, Andrei Kolmakov, Kim McKelvey, Nicholas Ware, Farid El Gabaly, Bruce Dunn, and Henry S White. Fabrication, testing, and simulation of all-solid-state three-dimensional Li-ion batteries. *ACS Applied Materials & Interfaces*, 8(47):32385–32391, 2016.

[135] Hong-Kang Tian, Zhe Liu, Yanzhou Ji, Long-Qing Chen, and Yue Qi. Interfacial electronic properties dictate Li dendrite growth in solid electrolytes. *Chemistry of Materials*, 31(18):7351–7359, 2019.

[136] Madison Morey, John Loftus, Andrew Cannon, and Emily Ryan. Interfacial studies on the effects of patterned anodes for guided lithium deposition in lithium metal batteries. *The Journal of Chemical Physics*, 156(1):014703, 2022.

[137] Junji Suzuki, Kyoichi Sekine, and Tsutomu Takamura. Evaluation of the diffusion coefficient of Li in Ag using a Li+ sensor electrode mounted in a bipolar cell. *Electrochemistry*, 74(4):303–308, 2006.

[138] J R Willhite, N Karnezos, P Cristea, and J O Brittain. Li^7 self diffusion in LiAl—an NMR study. *Journal of Physics and Chemistry of Solids*, 37(12):1073–1076, 1976.

[139] Tao Zhang, Lijun Fu, Jie Gao, Yuping Wu, Rudolf Holze, and Haoqing Wu. Nanosized tin anode prepared by laser-induced vapor deposition for lithium ion battery. *Journal of Power Sources*, 174(2):770–773, 2007.

[140] William R. Tyson and William Alfred Miller. Surface free energies of solid metals: Estimation from liquid surface tension measurements. *Surface Science*, 62(1):267–276, 1977.

[141] Frank C Walsh. Electrode reactions in metal finishing. *Transactions of the IMF*, 69(3):107–110, 1991.

[142] György Kaptay. Method for estimating solid-solid interface energies in metal-ceramic systems: The aluminium-silicon carbide system. In *Materials Science Forum*, volume 215, pages 475–484. Trans Tech Publ, 1996.

[143] Kun Shen, Yixuan Wang, Jun Zhang, Yi Zong, Gengwei Li, Changchun Zhao, and Hao Chen. Revealing the effect of grain boundary segregation on li ion transport in polycrystalline anti-perovskite li 3 clo: a phase field study. *Physical Chemistry Chemical Physics*, 22(5):3030–3036, 2020.

[144] Kun Fu, Yunhui Gong, Boyang Liu, Yizhou Zhu, Shaomao Xu, Yonggang Yao, Wei Luo, Chengwei Wang, Steven D Lacey, Jiaqi Dai, et al. Toward garnet electrolyte–based li metal batteries: An ultrathin, highly effective, artificial solid-state electrolyte/metallic li interface. *Science Advances*, 3(4):e1601659, 2017.

[145] Minghui He, Zhonghui Cui, Cheng Chen, Yiqiu Li, and Xiangxin Guo. Formation of self-limited, stable and conductive interfaces between garnet electrolytes and lithium anodes for reversible lithium cycling in solid-state batteries. *Journal of Materials Chemistry A*, 6(24):11463–11470, 2018.

[146] Kun Fu, Yunhui Gong, Zhezhen Fu, Hua Xie, Yonggang Yao, Boyang Liu, Marcus Carter, Eric Wachsman, and Liangbing Hu. Transient behavior of the metal interface in lithium metal–garnet batteries. *Angewandte Chemie International Edition*, 56(47):14942–14947, 2017.

[147] Xiaogang Han, Yunhui Gong, Kun Kelvin Fu, Xingfeng He, Gregory T Hitz,

Jiaqi Dai, Alex Pearse, Boyang Liu, Howard Wang, and Gary Rubloff. Negating interfacial impedance in garnet-based solid-state li metal batteries. *Nature Materials*, 16(5):572–579, 2017.

[148] Henghui Xu, Yutao Li, Aijun Zhou, Nan Wu, Sen Xin, Zongyao Li, and John B Goodenough. Li3n-modified garnet electrolyte for all-solid-state lithium metal batteries operated at 40° c. *Nano Letters*, 18(11):7414–7418, 2018.

[149] Xiulin Fan, Xiao Ji, Fudong Han, Jie Yue, Ji Chen, Long Chen, Tao Deng, Jianjun Jiang, and Chunsheng Wang. Fluorinated solid electrolyte interphase enables highly reversible solid-state li metal battery. *Science Advances*, 4(12):9245, 2018.

[150] Chunsong Kwon and Daniel M Tartakovsky. Modified immersed boundary method for flows over randomly rough surfaces. *Journal of Computational Physics*, 406:109195, 2020.

[151] Dongbin Xiu and Daniel M Tartakovsky. Numerical methods for differential equations in random domains. *SIAM Journal on Scientific Computing*, 28(3):1167–1185, 2006.

[152] Daniel M Tartakovsky and Dongbin Xiu. Stochastic analysis of transport in tubes with rough walls. *Journal of Computational Physics*, 217(1):248–259, 2006.